

ELECTRONIC TRANSPORT, FIELD EFFECT  
AND DOPING  
IN PENTACENE NANORODS AND  
MONOLAYER THIN FILM  
PREPARED BY COMBINATION OF  
NANO-FABRICATION AND SELF-ASSEMBLY.

**Inauguraldissertation**

zur

Erlangung der Würde eines Doktors der Philosophie  
vorgelegt der  
Philosophisch-Naturwissenschaftlichen Fakultät  
der Universität Basel

von

**Claudio Vanoni**

aus Aurigeno, Tessin

Villigen, 2008

Genehmigt von der Philosophisch-Naturwissenschaftlichen Fakultät  
auf Antrag von

Prof. Dr. Ch. Schönenberger  
Dr. T. A. Jung  
Dr. W. Riess

Basel, den 19. September 2006

Prof. Dr. Hans-Peter Hauri  
Dekan

# Abstract

The transport in organic semiconductors is investigated on the nanometer scale. Field effect transistor with device-active layers in the monolayer (ML) range are characterized in-situ right after the controlled deposition of pentacene. By using a bottom contact geometry, the thickness of the channel is varied in several steps and the thin film transistors (TFTs) are characterized after each additional deposition. The mobility is found to saturate at a channel thickness of 3-4 ML. This allows for the operation of 2 ML TFT, where the effect of dopant molecules deposited on top of the channel is studied. Fluorinated tetracyanoquinodimethane ( $F_4TCNQ$ ) is found to increase the charge carrier concentration by a charge transfer process with pentacene without degradation of the mobility. For a separation of contact effects from bulk effects, TFTs with channel length between  $20\ \mu\text{m}$  and  $200\ \mu\text{m}$  have been processed in parallel. The contact resistance  $R_c$  and the contact free mobility  $\mu_{cf}$  have been extracted and analyzed by the transmission line method (TLM).

In temperature dependent studies, an approximately linear  $\log(\mu)$  vs.  $1/T$  relation describes the experimental results. The fit is slightly better for the undoped TFT compared to the doped TFT. This is consistent with the accepted theoretical models based on a disordered

Gaussian density of states (DOS). In fact, the experimental determination of the DOS in doped TFTs shows an additional broad peak at 0.14 eV above the HOMO edge caused by the dopant molecules.

A second pronounced effect of doping is the reduction of the  $R_c$  by a factor 20 between the gold electrode and pentacene. The gate field dependent decrease of  $R_c$  in undoped TFTs is related to a lowering of the Schottky barrier at the interface. In doped TFTs, the opposite effect is observed. This demonstrates the influence of the dopant molecules on the interface barrier. The injection process determining  $R_c$  is found to change from a thermionic emission mechanism to a tunneling regime.

For the investigation of the injection properties at the interface, a new manufacturing method to produce metallic nanojunction is presented. In combination with a self-assembly process leading to pentacene rod-like islands connecting the two electrodes right through their growth, the transport in the 10-nm scale is investigated. At this scale length, the current-voltage (I-V) characteristics of pentacene is changing from rectifying Schottky-like behavior to fully linear behavior upon F<sub>4</sub>TCNQ doping. Variable temperature investigations show that the conduction in the doped pentacene nanojunction is thermally activated, with an activation energy very close to the energy position of the dopant induced peak in the DOS and to the thermal activation energy of  $R_c$ .

*keywords:*

organic semiconductor, pentacene, field effect, monolayer, mobility, density of states (DOS), transport mechanism, nanoscale transport, nanojunction, electromigration, nanorods, injection, contact resistance, metal-organic interface, Schottky barrier, doping, thermally assisted tunneling, gate field modulation, in-situ doping, charge transfer.

# Contents

|   |           |
|---|-----------|
| <b>Abstract</b>   | <b>3</b>  |
| <b>1 Introduction and motivation</b>                        | <b>9</b>  |
| <b>2 Outline</b>  | <b>15</b> |
| <b>3 Fabrication and characterization of nanojunctions</b>  | <b>19</b> |
| 3.1 Manufacturing process . . . . .                         | 20        |
| 3.2 Batch process . . . . .                                 | 22        |
| 3.3 In-situ control of the nanojunction formation . . . . . | 25        |
| 3.4 Concerns on electrical stability . . . . .              | 32        |
| 3.5 Concerns on chemical stability . . . . .                | 37        |
| <b>4 Self-assembly and growth of pentacene thin film</b>    | <b>41</b> |
| 4.1 Principle of self-assembly . . . . .                    | 41        |
| 4.2 Pentacene: model for ordered organic semiconductors     | 45        |

|          |  |           |
|----------|--|-----------|
| 4.3      | Physical vapor deposition of pentacene . . . . .                                     | 46        |
| 4.4      | Structural Characterization . . . . .  | 49        |
| 4.4.1    | Methods: AFM, SEM and XRD . . . . .  | 49        |
| 4.4.2    | Pentacene on oxide surface . . . . .   | 50        |
| 4.4.3    | Pentacene on metal surfaces . . . . .  | 55        |
| <b>5</b> | <b>Electrical transport through self-assembled pentacene nanorods</b>                | <b>63</b> |
| 5.1      | Contacting pentacene nanorods by a metallic nano-junction . . . . .                  | 64        |
| 5.2      | Current-voltage measurements of undoped and doped nanorods . . . . .                 | 64        |
| 5.3      | Temperature dependence of the conductivity . . . . .                                 | 70        |
| 5.3.1    | Experimetal setup . . . . .  | 70        |
| 5.3.2    | Results on doped pentacene . . . . .   | 70        |
| 5.3.3    | Undoped pentacene nanorods . . . . .   | 72        |
| 5.4      | Possible transport mechanism . . . . .   | 76        |
| <b>6</b> | <b>In-situ doping of a few monolayer pentacene thin film</b>                         | <b>83</b> |
| 6.1      | Thin film transistor: introduction and working principle                             | 84        |
| 6.1.1    | Design . . . . .   | 84        |
| 6.1.2    | Working principle . . . . .  | 85        |
| 6.1.3    | Extrapolation of TFT mobility and charge carrier density from measurements . . . . . | 86        |
| 6.1.4    | Correction for contact resistance: transmission line method (TLM) . . . . .          | 89        |
| 6.1.5    | Considerations on the models, peculiarities of organic semiconductors . . . . .      | 90        |
| 6.2      | In-situ control of TFT formation . . . . .   | 93        |
| 6.2.1    | Sample preparation . . . . .   | 93        |
| 6.2.2    | Measurements setup . . . . .   | 94        |
| 6.2.3    | TFT formation . . . . .  | 94        |

## CONTENTS

---

|          |  |            |
|----------|--|------------|
| 6.3      | Determination of the mobility and the threshold gate voltage . . . . .                           | 95         |
| 6.4      | Effect of guest dopant molecules . . . . .   | 104        |
| 6.4.1    | Control of threshold gate voltage by in-situ doping . . . . .                                    | 104        |
| 6.4.2    | F <sub>4</sub> TCNQ doping : effect on the carrier concentration . . . . .                       | 109        |
| 6.5      | Influence of air exposure on the threshold gate voltage  | 113        |
| <b>7</b> | <b>Coevaporation of F<sub>4</sub>TCNQ and pentacene</b>  | <b>117</b> |
| 7.1      | Reduction of the contact resistance . . . . .  | 117        |
| 7.2      | Comparison between the mobility of undoped and doped TFT . . . . .                               | 123        |
| <b>8</b> | <b>Thermally activated transport in pentacene</b>  | <b>125</b> |
| 8.1      | Temperature dependence of the mobility . . . . .   | 126        |
| 8.2      | Temperature-induced shift of the gate voltage threshold  | 134        |
| 8.3      | Contact resistance . . . . .   | 136        |
| 8.4      | Charge carrier density dependence of the contact free mobility at various temperatures . . . . . | 138        |
| 8.5      | Density of states in undoped and F <sub>4</sub> TCNQ doped pentacene . . . . .                   | 141        |
| <b>9</b> | <b>Conclusions and Outlook</b>   | <b>149</b> |
|          | <b>Bibliography</b>  | <b>152</b> |
|          | <b>Acknowledgments</b>   | <b>152</b> |
|          | <b>Pubblication</b>  | <b>165</b> |
|          | <b>Acknowledgments</b>   | <b>168</b> |



# Chapter 1

## Introduction and motivation

Looking at the changes of our society in the recent history, two major driving forces to the development can be recognized: communication and computation. Society evolved from localized small communities to a network of interlinked individuals, where an efficient and extended information exchange is taking place. For a fast, reliable and long-range information transport, we do not anymore rely on Pheidippides, homing pigeon, or smoke signals. Since the beginning of the last century, two very efficient information carriers have been exploited: electromagnetic waves and electrons. This enables communication between any two locations on the planet earth in less than the time needed for the human being to react on an external

## INTRODUCTION AND MOTIVATION

---

stimulus, typically 100 ms. On the other hand, the large quantity of information generated everyday and available on archive has to be processed to make it useful: this is where computation plays a major role. The invention of integrated circuits has largely facilitated this task, another development that has promoted the electron as the major actor. The arena is obtained from highly artificial materials, like ultra-purified silicon engineered with dopants concerted even more exotic materials like GaN. The physics in these condensed matters is favorable to the manipulation of electrons, the exploitation of the extent and the quantum properties of its wave-like nature. Nowadays the use of electromagnetic waves for communication and electronic computation is the basis of the information era that we live in.

Recently, very practical limitations started to be pointed out. Conventional semiconductors lack on flexibility, can not be processed in large areas and depend on increasing (and less and less sustainable) investments costs [1]. Organic electronics offers a large potential for improvement to compete with inorganic counterpart. Indeed, many industrial and academic institutions are working on the implementation of this new class of semiconductors into applications. A few examples have already reached the market, like organic light emitting diodes (OLED) and radio frequency identifier (RFID), others will follow.

Besides the engineering development, more fundamental studies are interested in the basic electronic behavior in organic semiconductors. It is realized that the aspects concerning the motion and the nature of charges are very different from inorganic materials. For example, the mobility of crystalline organic semiconductors is much lower compared to single crystal inorganic semiconductors. In the best organic semiconductors like small weight polyacenes, the mobility reaches the  $1\text{ cm}^2/(\text{Vs})$  range, which is almost comparable to amorphous silicon. However, highly desirable solution-processible or-

---

ganic semiconductors still exhibit mobilities many orders of magnitude below this values. In order to improve the device performance, knowledge on the relation between the microscopic structural morphology and the mobility is required.

From a physical point of view, the major differences come from the rather weak Van der Waals intermolecular forces that bind together the molecules in crystalline  $\pi$  conjugated organic solid and the chains in polymer compounds. The bandwidth arising from the splitting of the highest occupied molecular orbital (HOMO) and the lowest unoccupied molecular orbital (LUMO) when going from an isolated molecule to interacting molecules is therefore narrow. Furthermore, it is even more decreased by electron-phonon coupling [2], i.e. it is strongly influenced by thermal fluctuations [3]. As a consequence, the transfer integral describing the electronic coupling between molecules is much weaker than between atoms in inorganic crystals. In other words, the electronic wave function is confined on a molecular scale and the mobility relies more on an hopping of charges between localized states rather than on an extended band mechanism. Recent theoretical descriptions model the transport in disordered organic semiconductors as a thermal assisted tunneling between localized molecular states [4]. Here, a central concept common to all the proposed models is the density of states (DOS) which directly influences the hopping mobility. The DOS arises from the further splitting of electronic transport orbitals caused by disorder. To a good approximation, the energy distribution of a pristine organic semiconductor DOS exhibits a Gaussian profile as confirmed by comparison between theoretical prediction and measurements of temperature, charge carrier density and field dependence of the mobility. In doped organic semiconductors, the DOS can be more complicated exhibiting additional peaks [5]. Consequently, the model should also consider the dopant induced states that may contribute

## INTRODUCTION AND MOTIVATION

---

to the charge transport. Therefore, comparisons between the experimental determined DOS and the transport properties are required and would allow to validate the theoretical predictions

The above considerations relate only to bulk devices. To which extent these models describe the electronic transport when the size or the dimensionality of the organic semiconductor is decreased only starts to be explored. In inorganic semiconductor, the lower limit of the relevant length scale where a bulk description of the electronic properties needs to be changed is set by the de Broglie wave length. Typically, in high mobility inorganic semiconductors this is in the 100 nm range. Since the electron wave function in organic semiconductors is much smaller, it is expected that the transport properties do not deviate from a classical bulk description down to the molecular dimensions. This implies that devices based on organic semiconductors can operate at small sizes compared to inorganic devices without changes of the physics that describe the working principles. For example, field effect transistor with a channel thickness in the few monolayers range have been demonstrated [6, 7]. These material systems offer significant advantages for device miniaturization. To manufacture device in this size range a bottom up approach where the components interconnect by a self-assembly process is required [8, 9, 10]. Possible application of small size organic devices is their use as sensors [11], provided that a large number of devices can be connected in parallel. The greatly enhanced sensitivity is given by the small number of entities necessary to change the physical properties on the nanometer scale. For example, surface charge transfer could provide carriers that are then detected by an increase of the conductance. The modulation of the conductance can also take place at the interface between the organic material and the electrode, which usually becomes the bottleneck for transport as the size is reduced. In sensors research the modulation is passively exploited to detect the

---

analyte, whereas in other research field it is engineered to enhance the injection of charges. In inorganic semiconductors, the mechanism leading to the reduction of the contact resistance for example by doping are well known [12]. In organic material, the same effect is observed, but the mechanism appear to be different. The injection process is described as an hopping process from the broad DOS of the first molecular layer to the much narrower DOS of the next layers [13]. However, the effect of doping at the interface and the consequent reduction of the contact resistance is not well understood yet.

The extreme case of miniaturization in organic semiconductor is reached in molecular electronics, where a single molecule is the basic constituent of a circuit [14]. Here, the physical description has to be adapted [15]: the flow of charges depends exact on the location of the molecular levels, which can be in principle addressed and manipulated. Since the energy level of a molecule can be chemically tailored, a variety of functionalities are available. Moreover, chemistry can produce these basic elements by a single synthesis in a quantity that is larger than the total number of inorganic transistors that have ever been produced. The major challenge remains to incorporate the molecules into a circuit, where the simplest one is composed by two electrodes that directly connect a single molecule. A number of approaches have been exploited for research [16, 17, 18, 19, 20, 21], a new one is presented in the first part of this work.

It is therefore important and very interesting to investigate the electronic behavior of organic semiconductors, doping processes and injection through metal-organic interface with reduced size and dimension of the active material, either by using ultra thin films in the monolayers range or by decreasing the size of the channel toward reaching molecular dimensions. This is the starting point of this thesis.



# Chapter 2

## Outline

This dissertation is organized as follow:

In Chap. 3 a top-down manufacturing process aimed at obtaining stable metallic junction with the electrode separation comparable to the length of a molecule is presented. This was the original goal of the work and is a fundamental requirement in order to investigate the transport properties through a single molecule. It will be shown that the necessary stability, both physically and chemically, to perform single molecule experiments is not met. Nevertheless, the obtained nanojunction with gap in the 10 nm range are useful to study the transport properties of organic semiconductors at this length scale and to characterize injection properties.

Chap. 4 describes the self-assembly of pentacene on different surfaces. Pentacene is chosen as a model for organic semiconductor ma-

terials because it possesses the most favourable electronic properties among organic semiconductors. Moreover, it does not chemically react with the metallic surfaces but only physically adsorbs. On  $\text{SiO}_2$ , the layer-by-layer growth is characterized, whereas on polycrystalline gold, a self-assembly process leading to rod-like pentacene islands (nanorods) is found. This Chapter sets the basis for the investigations of the electric transport properties of few monolayer (ML) thin film transistor (TFT) and of the self assembled pentacene nanorods.

In Chap. 5 a new bottom-up approach based on the self-assembly of pentacene nanorods grown across metallic nanojunctions is shown. Electrical transport through undoped and doped nanorods, in air and in vacuum at variable temperature is investigated on the nanometer scale. Possible transport mechanisms are then discussed with the focus on the effect of doping on the injection properties across the metal-organic interface.

In order to compare the transport properties of the nanorods, few ML pentacene in a TFT geometry are investigated in Chap. 6. Pentacene channels with a thickness of 1.7-7 ML are characterized *in-situ*. The doping effect is studied by evaporation of dopant molecules in a sub-ML coverage on top of the channel. The surface sensitivity of the ultrathin channel is also exploited to investigate the effects of air exposure.

Chap. 7 present the crucial effect of  $\text{F}_4\text{TCNQ}$  doping on the charge injection across metal-pentacene interfaces. This is achieved by using TFTs with different channel lengths, where the contact resistance ( $R_c$ ) is obtained by the application of the transmission line method (TLM). The gate field influence on  $R_c$  is discussed.

Temperature dependent transport studies in undoped and  $\text{F}_4\text{TCNQ}$  doped TFTs are shown in Chap. 8. The  $R_c$  and  $\mu$  dependence on the temperature  $T$  is discussed along with the relation between contact free mobility  $\mu_{cf}$ , carrier concentration  $p$  and  $T$ . Fi-

---

nally, the dopant induced modification of the density of states (DOS) is extracted from the data. The influence of the modified DOS on the transport and injection properties, as well as the comparison between the transport in nanoscale junction and in TFT setup are presented.



# Chapter 3

## Fabrication and characterization of nanojunctions

In this chapter, a new manufacturing process for obtaining two metallic electrodes with a separation that can be adjusted from tens of nm to few nm is presented. The method makes beneficial use of the angle deposition technique while taking a pre-fabricated step as the shadow mask: a metallic layer is deposited from a negative angle direction with respect to the vertical sidewall of a sharp step.

# FABRICATION AND CHARACTERIZATION OF NANOJUNCTIONS

## 3.1 Manufacturing process

Fig. 3.1 shows the processing steps used to produce the nanojunctions.

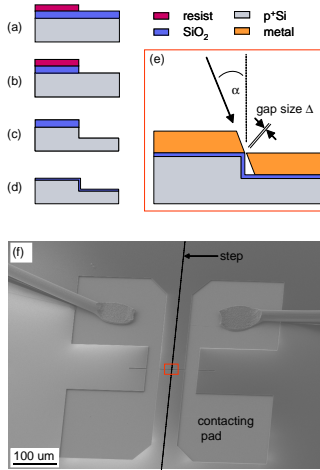


**Figure 3.1:** (a)-(d) Processing for the preparation of the sharp insulating step. (e) angle evaporation of the metal electrodes. (f) SEM of a device showing the two contacting pads and the thin wire crossing the step. At the center, the location of the gap (red square).

The manufacturing starts by defining the location of the step. A p-type (110) Si 4" wafer is patterned by photolithography. For

### 3.1. MANUFACTURING PROCESS

---

this purpose, a window is opened in a positive resist (Fig. 3.1(a)), where the resist is used as a mask for the removal of the oxide by buffered oxide etchant (Fig. 3.1(b)). Next, the resist is removed and the unetched oxide is used as a mask for the anisotropic etching of the Si substrate obtained with a water solution of tetramethylammonium hydroxide (Fig. 3.1(c)). The time necessary to reach the desired depth was calibrated before each run on a test piece. The etching rate varies between 5 nm/sec and 10 nm/sec. The depth of trench etched in the substrate was reduced as possible, although for depths below  $\sim 100$  nm, a step edge with only modest quality is obtained. The reason is the waviness of the resist, the resulting waviness on the oxide mask and the missalinement with respect to the crystallographic orientation of the substrate. The anisotropic etching process therefore requires a minimum etch depth for to smooth out these irregularities and to obtain a single (111) vertical plane along the patterned line. After accomplishing the etching process, the remaining oxide is removed. In order to insulate the semiconducting substrate from the surface, 50 nm of high quality  $\text{SiO}_2$  are regrown onto the surface by a dry thermal oxidation (Fig. 3.1(d)). It was verified by scanning electron microscopy (SEM) that the step edge remains sharp also after the oxide regrowth. Next, contacting pads,  $40 \mu\text{m}$  from each side of the step, are patterned. In this case a double layer process is used. It makes use of a second resist layer on top of a (not photosensitive) first one. By adjusting the exposure and the developing time, an undercut in the resist profile is obtained. The double layer process is used to facilitated the lift-off after the metal deposition and for obtaining a metal layer with a gentle decreasing thickness toward the boarders by continuously rotating the sample during metalization. Finally, because the substrate serves as a gate electrode and for monitoring of the leakage current, the backside was covered by a Ti/Cr metal layer. The wafer is then sawed in  $21 \times 7$  or  $7 \times 7 \text{ mm}^2$  pieces and fur-

## FABRICATION AND CHARACTERIZATION OF NANOJUNCTIONS

---

ther processed by the manufacturing of the metallic nanojunction. For this purpose, a  $1.5\ \mu\text{m}$ -wide Au or Pd wire is deposited at ambient temperature through an opening in a second double layer resist. This metallic wire is oriented perpendicular to the step edge direction and electrically contacts the pre-patterned pads. The evaporation is performed from an angle  $\alpha$  with respect to the surface normal direction (Fig. 3.1(e)). Depositing the metal at a perpendicular direction leads to an increased number of defective devices. Using a larger deposition angle, the minimal gap size increased. Good results are obtained by using an angle of  $10^\circ - 30^\circ$ . The wire is produced by thermal evaporation (resistive heating) of the metal at a background pressure of  $2 \cdot 10^{-6}$  mbar and at a deposition rate of  $1\text{-}2\ \text{\AA}/\text{sec}$ , which is continuously monitored by using a quartz microbalance. The deposition rate is calibrated by profilometer measurements (alpha-step, Tencor) and by tapping mode atomic force microscope.

### 3.2 Batch process

A batch process involving a sample that can be moved behind a shutter has been developed (Fig. 3.2). This enables the variation of the electrode thickness along one axis of the two dimensional array of identical prepared devices. Devices obtained in this way possess a gap spacing that depends on their position in the 2D array along the direction of motion of the shutter. The sample is mounted on a moving holder that can be tilted before the evaporation by a fixed angle, which define the evaporation angle  $\alpha$  described in Fig. 3.1(e).

For a statistical analysis on the obtained gap size, two methods are adopted. The first one is based on measurements from SEM images of the gap size of open, nominal identically devices. The second one is based on the electrical characterization of the devices produced by the movable shutter technique. The gap size of one device

## 3.2. BATCH PROCESS

---

is estimated from SEM images by the average of 10 measurements of the electrode distances along the gap region. Typically, such measurements give a scatter for the gap of one device of  $\pm 5$  nm. By measuring the gap of 20 devices obtained from 3 different runs aimed at the same deposited thickness, it is found that the mean gap size is  $19 \pm 5$ ,  $21 \pm 8$  and  $8 \pm 5$  nm. It is concluded that the deposition process can be controlled with a precision of  $\pm 7$  nm for a total thickness of  $\sim 100$  nm. By looking at the devices produced on the same run, the variation of the gap size between devices is  $\pm 6$  nm. This is not surprising, since close inspection of the SEM image reveals that the deposited Au layer forms a polycrystalline film consisting of 30-50 nm-size crystal grains. However, due to the 3-dimensional geometry of the gap, a precise measurement of the gap size is difficult.

For this reason, the second method based on electrical measurements is also presented. Table 3.2 shows a statistical analysis based on one chip where different metal thicknesses  $h_{step}$  are deposited (deposition angle  $21^\circ$ ) with the movable shutter technique over rows of devices (63 devices measured in total) with the same step height  $h_{step} = 120$  nm.

The results show that up to a metal thickness of 87 nm all the devices were open. The gap in these devices is in the range of tens of nm. By increasing the deposited thickness, the percentage of open devices decreases. In these rows, the open devices have a gap in the 10 nm range. By further increasing the metal thickness, the gap size and the yield of open devices decrease. At a target gap size of 3 nm, 50% of the devices were short. Finally, for metal thickness above 161 nm all the devices were short. As already mentioned in the analysis based on SEM images, the graininess of the film growth leads to individual grains that in many cases bridge the gap before the average Au thickness reaches the step height. This observation also indicates the important role of the Au atom diffusion during the

## FABRICATION AND CHARACTERIZATION OF NANOJUNCTIONS

---

**Table 3.1:** Statistical analysis based on the electrical characterization of 63 devices with the same step height  $h_{step}=120$  nm and with different deposited thickness  $h_{av}$ .

| deposited thickness (nm) | target gap size (nm)<br>( $h_{step} - h_{av}$ ) | open devices (%) |
|--------------------------|---|------------------|
| $\leq 87$                | $\geq 33$                                       | 100              |
| 102                      | 18  | 71               |
| 117                      | 3   | 50               |
| 131                      | -11   | 12               |
| 146                      | -26   | 37               |
| 161                      | -41   | 0                |

### 3.3. IN-SITU CONTROL OF THE NANोजUNCTION FORMATION

---

deposition in the nm scale at ambient temperature [22]. In other cases, the grains provide a local shadow effect delaying the shorting of the junction. This is probably the case for the open devices with electrode thickness above 120 nm. From these data, the scatter of the gap size is considered to be  $\pm 15$  nm, which is higher than the estimation based on the SEM images. One reason is that the analysis based electrical characterization also includes devices with defects, like unusual big grains and damages caused by the measurements process.

Nevertheless, nanojunction devices with a gap size of  $\sim 10$  nm are successfully used in Chap. 5 for the electrical characterization of the transport of organic semiconductors on the nanometer scale by exploiting the self-assembling process presented in the Sec. 4.4.3.

### 3.3 In-situ control of the nanojunction formation

Aiming at the original goal of contacting individual small molecules it is necessary to fabricate 1 nm-scale nanojunction devices. For this purpose, the transient of the nanojunction formation from electrically open to short-circuited devices during the deposition of the electrodes is explored. It is likely that the first contact between the electrodes relates to one or several fast growing grains near the step edge. At a certain critical gap size, an open junction becomes unstable, exhibits resistance fluctuations and finally closes by the diffusion of metal atoms. This transient process is monitored by measuring the conductance of one specific device in-situ during the deposition of the narrow metallic wire at the last step of the device fabrication process. A very different behavior is observed between the use of gold and palladium as electrode material. First the situation for Au

## FABRICATION AND CHARACTERIZATION OF NANOJUNCTIONS

---

is discussed.

Fig. 3.4 shows the relation between the junction conductance  $G$  and the deposition time for a device having  $h_{step}$  of 100 nm when the evaporation rate is fixed at  $\sim 1.3 \text{ \AA/s}$ . The abscissa gives the amount of deposited metal with reference to the deposition time (bottom) and average metal thickness  $h_{av}$  (top) which is calibrated within 10%. The ordinate shows  $G$  scaled by the conductance quantum  $G_0 = 2e^2/h$ .  $G$  was monitored by measuring the device current while applying a fixed bias  $V=10 \text{ mV}$  during the deposition. It is found that when  $h_{av}$  exceeds  $\sim 5 \text{ nm}$ ,  $G$  begins to increase substantially. Further on, the ratio  $G/G_0$  increases to values higher than 1 when  $h_{av}$  is close to  $\sim 20 \text{ nm}$ . For  $h_{av}$  values above  $\sim 20 \text{ nm}$ , the Au wire between the contact pads and the step edge forms a continuous film as recognized by both SEM investigation and transport measurements. The final  $h_{av}$  is a factor of 5 smaller than  $h_{step}$ . This observation is ascribed to the diffusion of the deposited Au atoms along the vertical sidewall of the step. This process is greatly enhanced by the control bias applied between the two electrodes, confirming the surface diffusion and electromigration behaviour of metal adatoms [23, 24].

The increase of  $G$  between 5 and 20 nm is likely due to the formation of a gold nanojunction ensemble consisting of nm-scale gold islands along the step sidewall. In fact, the presence of such gold islands was confirmed by SEM and also by the low temperature transport experiments presented in Sec. 3.4.

A different behaviour is observed when Pd is used as electrode material. The result is shown in Fig. 3.5. In this case the increase of  $G$  is not observed below  $h_{av}$  of  $\sim 88 \text{ nm}$ . The diffusion of the Pd atoms appears to be substantially weaker than that of Au atoms. This is in agreement with reference [25]. When  $h_{av}$  is increased from  $\sim 89 \text{ nm}$  to  $\sim 92 \text{ nm}$ ,  $G$  increases exponentially, in correspondence to the increasing tunneling probability with the gap narrowing in this

### 3.3. IN-SITU CONTROL OF THE NANOFUNCTION FORMATION

---

$h_{av}$  range. When  $h_{av}$  is between 92 and 93.5 nm,  $G$  exhibits a plateau ( $G = G_0$ ) indicating the formation of a metallic point contact that is likely to occur at a single metallic grain boundary at the step edge [26]. Further evaporation above 94 nm leads to a short-circuited device with resistance in the  $100\ \Omega$  range.

## FABRICATION AND CHARACTERIZATION OF NANOJUNCTIONS

---

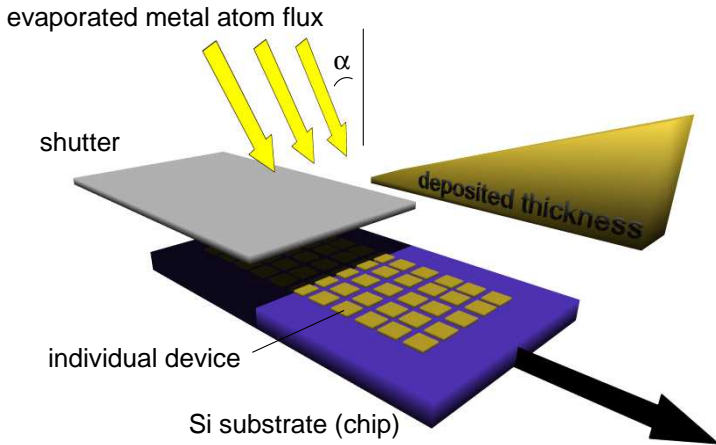


**Figure 3.2:** Drawing of the moving shutter technique. The chip with the devices is placed on a movable stage below a shutter. In this way, the device can be slowly exposed to the evaporated metal atoms creating a gradient in the deposited thickness along the direction of the motion. For performing the angle evaporation, the stage can be placed in a tilted position in the evaporation chamber.

### 3.3. IN-SITU CONTROL OF THE NANOFUNCTION FORMATION

---

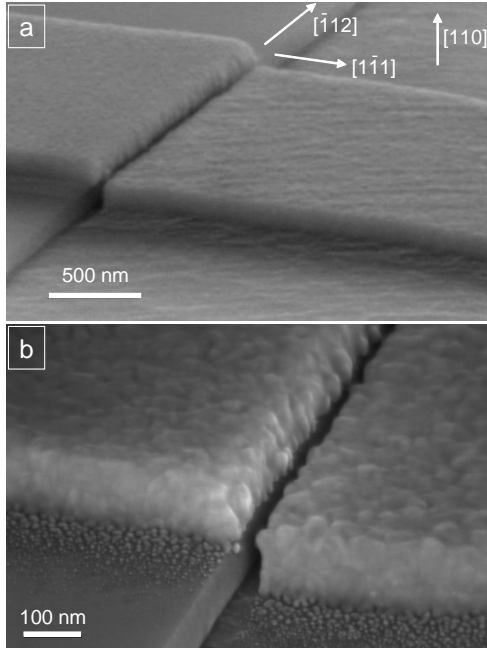


**Figure 3.3:** (a) SEM micrograph of a gold device typically obtained by the batch process. The step edge is aligned along the  $[\bar{1}12]$  direction while the metal is aligned perpendicular to the step. The width of the electrodes is  $1.5\ \mu\text{m}$  and the step height  $h_{step}$  is  $\sim 100\ \text{nm}$ . (b) Detail of the junction showing a gap size of  $\sim 10\ \text{nm}$ . The smooth vertical sidewall of the substrate step originates from the slowly etched  $(1\bar{1}1)$  plane of the substrate.

## FABRICATION AND CHARACTERIZATION OF NANOJUNCTIONS

---

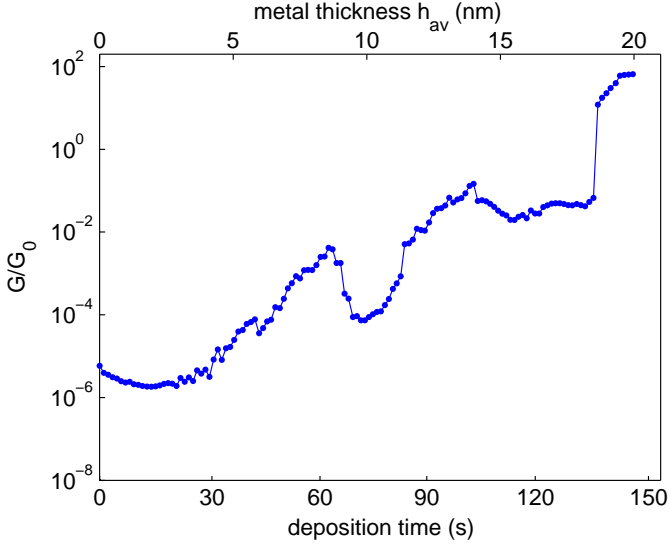


**Figure 3.4:** The variation of the conductance  $G$  of the Au nanojunction device measured in-situ in function of Au deposition time.  $G$  has been measured by applying a fixed bias of 10 mV and is scaled to the conductance quantum  $G_0$ . A device with  $100 \pm 3$  nm step height was used. Note the start of the increase of  $G$  with increasing Au layer thickness which is more than a factor 10 lower than the step height. This observation indicates an enhancement of the migration of the Au atoms along the gap by the applied bias.

### 3.3. IN-SITU CONTROL OF THE NANOFUNCTION FORMATION

---

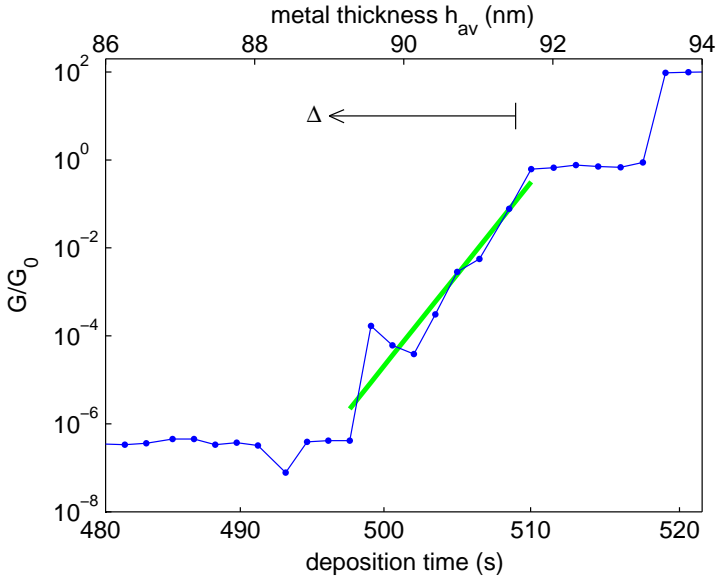


**Figure 3.5:** The variation of the conductance  $G$  of the Pd nanojunction device measured in-situ as a function of the Pd deposition time.  $G$  has been measured by applying a fixed bias of 10 mV and is scaled to the conductance quantum  $G_0$ . A device with  $100 \pm 3$  nm step height was used. The thick line is an exponential fitting of the conductance change when the deposited Pd thickness increases from 89 to 92 nm.

### 3.4 Concerns on electrical stability

To study the stability of the palladium point contact produced during simultaneous in-situ control, the evaporation is stopped when the junction conductance is detected to be equal to  $G_0$  and the variation of  $G$  with time is monitored. Fig. 3.6 shows the result. It is found that  $G$  remains close to  $G_0$  for an initial 30 s, then decreases in time. The decrease of  $G$  occurs in a stepwise way similar to the conductance variation observed in a mechanically controllable break junction. In both cases, the discrete rearrangement of atoms in the junction causes finite conductance changes. However it should be noted that here the measured currents is in the tunneling regime ( $G \ll G_0$ ) while break junction experiments refer to a situation where there is an initial metallic contact between the electrodes.

To estimate the final junction gap size from the observed conductance in Fig. 3.6, the exponential relation between  $G$  and  $\Delta$  observed in Fig. 3.5 for  $h_{av}$  between 89 and 92 nm is considered. The right ordinate shows the result: here it is assumed that  $\Delta$  is zero for  $h_{av}$  equal to  $h_0 = 92$  nm, and  $G$  is fitted by  $G_0 e^{-\beta \Delta}$  with  $\Delta = (h_0 - h_{av})$ . The fit provides a phenomenological tunneling parameter  $\beta = 0.49 \pm 0.14 \text{ \AA}^{-1}$ . Using  $\beta$ , the observed drop of  $G$  from  $G_0$  to  $(10^{-4} - 10^{-6}) \times G_0$  in Fig. 3.6 is ascribed to the increase of  $\Delta$  up to 1-3 nm, which is compatible to the molecular length scale. It should be noted that the noise level in these measurements is below 1 pA at  $V=0.1$  V as it can be seen from the base line of Fig. 3.5. All the data points above  $5 \times 10^{-7}$  are not influenced by noise or significant experimental errors and reflect therefore real changes in the junction.

Although the point contact ( $G = G_0$ ) observed in the Pd nanojunction device can be ascribed to an atomic scale contact at a metallic grain around the step edge, several metallic grains along the 1.5  $\mu\text{m}$ -wide step of the device can be simultaneously responsible for the

### 3.4. CONCERNS ON ELECTRICAL STABILITY

---

conductance in the tunneling regime ( $G \ll G_0$ ). In fact, when the nanojunction is realized at an edge of a single metallic grain, the tunneling conductance varies with  $\Delta$  as  $e^{-\beta^0 \Delta}$  by tunneling of electrons through vacuum, where  $\beta^0$ , given by  $2\sqrt{2me\phi_M/\hbar^2}$  ( $m$  is the electron mass,  $e$  the electron charge,  $\hbar$  the Planck constant and the metal's work function  $\phi_M = 2 - 5$  eV) takes a value of  $1.5 - 2.3 \text{ \AA}^{-1}$ . The factor of 3-5 discrepancy of the observed  $\beta$  from  $\beta^0$  is too large to be ascribed to the uncertainty of the actual  $\phi_M$  in the device. Therefore the observed smaller slope of  $G$  in Fig. 3.5 is likely due to the narrowing of the gap and the concomitant increase of the number of the grains along the step. However, the evaluated final gap size of 1-3 nm in Fig. 3.6 still provides an adequate estimate since the experimentally fitted value of  $\beta$  as determined above is used in the procedure. By assuming a single Pd grain contact, the obtained gap size can be evaluate to be  $\sim 0.5$  nm ( $\beta^0 = 2.3 \text{ \AA}^{-1}$  with  $\phi_M = 5.1$  eV) which constitutes the lower limit of the estimate.

From this analysis, a single grain tunneling junction devices can likely be produced by narrowing the width of the electrodes by e.g. electron beam lithography. This will also be helpful in the case of nanojunctions with larger gap, where the location of the nm-sized organic conductor like the nanorods presented in Chap. 5 may not be identical to the place where the gap is minimal.

The electrical stability of the nanojunction devices is also a major concern for the transfer and connection to external circuits. A lot of care must be take in order to limit drastic changes in the device. A very necessary precaution, is to wear an anti-static wrist strap and connected all the instrumental cables to ground through a high resistance before and while connecting the devices. The reason is that because of the small but insulating gap involved, any potential fluctuations between the two electrodes produce a huge electric field, which cause atomic electromigration or, in the extreme case, even an

## FABRICATION AND CHARACTERIZATION OF NANOJUNCTIONS

---

explosion of the junction area with damages that can be seen by eye.

Even if all the cares are taken, the nanojunctions with gaps in the 1 nm range are extreme difficult to handle. An example is given in Fig. 3.7. The devices used for these experiments are prepared by evaporating gold with a positive angle ( $\sim 20^\circ$ ) respect to the sidewall of the prepatterned step. In this way, a very thin film of gold ( $< 10$  nm) on the vertical sidewall connected by two thicker electrodes on the horizontal surfaces is obtained. Because of the dewetting of gold deposited on oxide, the film forms gold islands separated by gaps in the 1 nm range. The islands formation is confirmed by SEM investigations and is very similar to the gold structure that can be seen on the  $\text{SiO}_2$  surface close to the electrode in Fig. 3.3(b). The chip with the device is then carefully electrically connected and cooled down to 4.2 K by slow immersion in a helium bath. The current-voltage characteristics reveal periodic steps separated by  $\sim 100$  meV. These are attributed to the Coulomb blockade phenomena due to electron tunneling between  $\sim 10$  nm-size gold islands [27]. The results shows also that the device change between two consecutive measurements, caused probably by some atomic rearrangement. This is remarkable, since at liquid helium temperature diffusion is strongly suppressed and electromigration, influenced by joule heating, is not expected to be relevant for the current intensities ( $\leq 100$  pA) measured here.

The presented example involves many  $\sim 1$  nm gaps between the gold islands, but the same conclusion on the high mobility of the gold atom can be made also for the nanojunctions devices. Although the stability is improved by using Pd, the physical limitations like diffusion and electromigration are of concern for every manufacturing method aimed at obtaining stable metallic nanogap for studying small, or even single, molecules.

### 3.4. CONCERNS ON ELECTRICAL STABILITY

---

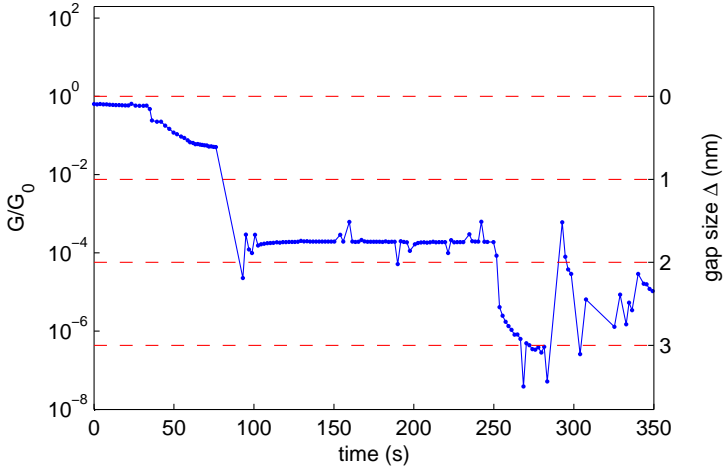


**Figure 3.6:** Temporal stability of the conductance  $G$  of the in-situ fabricated Pd nanojunction device after terminating the Pd evaporation when  $G$  reaches the conductance quantum  $G_0$ . A fixed bias of 10 mV is applied throughout the fabrication of the device and after termination of the evaporation. The gap size  $\Delta$  is calculated from the fit of  $\Delta$  vs.  $G/G_0$  presented in Fig. 3.5.

# FABRICATION AND CHARACTERIZATION OF NANOJUNCTIONS

---

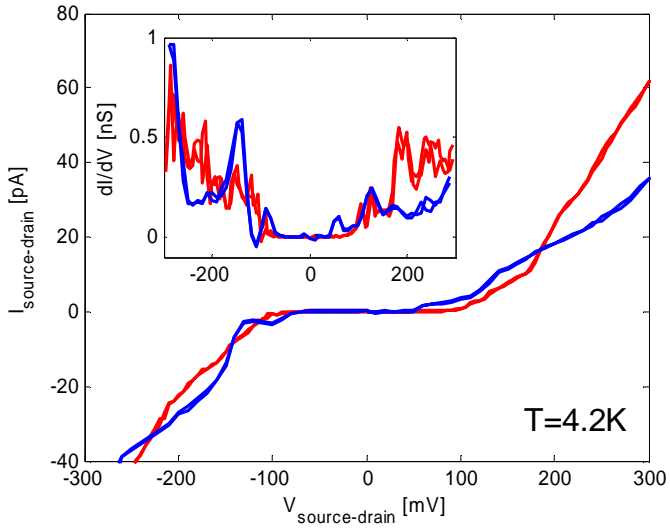


**Figure 3.7:** Low temperature ( $4.2\text{ K}$ ) current-voltage characteristics of the same device showing structural changes between two consequently measurements.

## 3.5. CONCERNS ON CHEMICAL STABILITY

---

### 3.5 Concerns on chemical stability

In an attempt to characterize the conduction through molecules, a large number of gold islands separated by gaps in the 1 nm range are exposed to a thiols solution. The devices are produced by depositing the metal but this time with a positive angle respect to prepatterned step. As result, an ensemble of gold islands on the vertical sidewall connected by the two electrodes is expected. The conductance of the devices increases with the thickness of the film, showing that separated islands merge together. The devices are then immersed in ethanol solutions of thiol-terminated molecules such as 1,4-benzenedimethanethiol (DMBT) and octanethiols (C8SH) for 20 h. The results are shown in Fig. 3.8. As a reference, a batch of devices are immersed in pure ethanol (EtOH). The conductance is often enhanced by a factor of 10-50 for a thickness smaller than 6 nm. Although it was difficult to obtain reliable data due to the instability of the device, it is evident that the conductance of the devices increases for both kind of thiol molecules. Transport experiments and theoretical consideration show that alkanethiols are orders of magnitude less conductive than conjugated thiols molecules. This suggests that the similar enhancement of the conductivity observed here is mainly related to the interaction of the thiol binding group with the gold atoms. In STM experiments on self-assembled monolayer of thiols on gold surfaces, it is observed that thiols modify the gold surface by creating etch pits [28]. It is therefore plausible, that the thiols groups locally modify the shape of the gold islands. Since the conduction is governed by tunneling between islands, a statistical change in the gap dimensions will be detected as an enhancement of the conductance driven by those gaps that become smaller. This instability against thiols solution can be also supported by considering that the gold islands are less stable than the reconstructed flat surface used in STM experiments, which are obtained by thermal treatment and should

## FABRICATION AND CHARACTERIZATION OF NANOJUNCTIONS

---

be more closer to the equilibrium.

In conclusion, the shape of gold islands produced by a thermal evaporation on a substrate is found to change upon adsorption of molecules from a thiol solutions. This scenario is different from the case where thermodynamically stable gold colloids are produced and used as metal electrodes [29, 30]. In the case of evaporated electrodes, the stability of the gold grains is a major concern for experiments where prepared 1 nm gaps are used for the self-assembly of thiol molecules. For this reason, in the next Chapters, the focus will be moved to pentacene molecules, which are much less aggressive and can be self-assembled also over gaps exceeding the 1 nm range.

### 3.5. CONCERNS ON CHEMICAL STABILITY

---

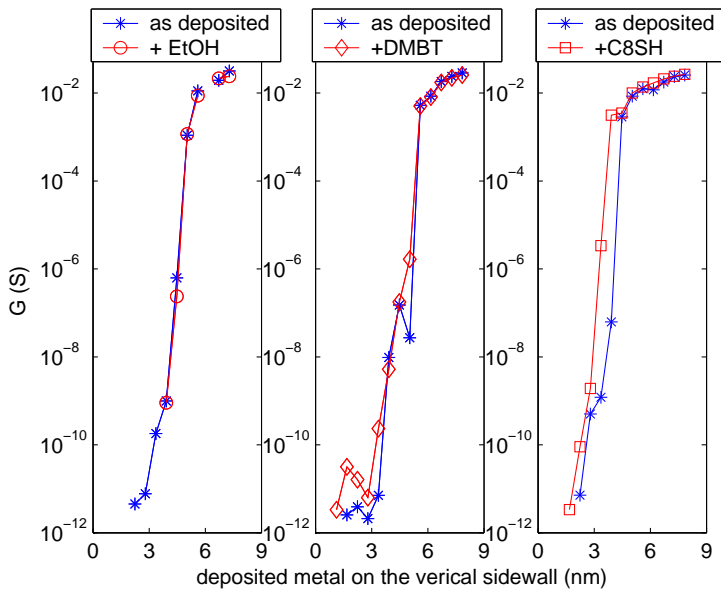


**Figure 3.8:** Conductance of the devices with increasing gold thickness on the vertical sidewall before and after immersion in different solutions.



# Chapter **4**

## Self-assembly and growth of pentacene thin film

In this chapter the technique and the setup used to deposit small organic molecules like pentacene is presented. Depending on the surface and on the parameters used for the self-assembly, different morphologies are obtained.

### 4.1 Principle of self-assembly

Self-assembly is a phenomenon in which simple components spontaneously form complex and ordered aggregates. This feature is ubiquitously found in biological systems. For example, membranous bound-

## SELF-ASSEMBLY AND GROWTH OF PENTACENE THIN FILM

---

ary structures like cell membrane define all life that we know today. Those structures, generate by a self-assembly process of amphiphile molecules solved in a liquid medium, seems to be very tightly bound to the origin of life [31]. In addition to the formation of micelles by adequate water soluble molecules, self-assembly can also take place in other environments and is not limited to molecules. As a general feature, it must involve components that interact with each other and with the environment. The environment must allow for motion of the constituent and can be a liquid phase or an interface. The interaction between the constituent are determined by the chemical structure of the molecules but can also be guide by “programmable instruction” obtained by specifically designed features, for example by chemically incorporate selective interactive groups at the particle surface or directly in the molecules [32]. The interaction between the components has to be balanced between repulsive and attractive forces and must be “weak”, i.e. its energy must be comparable to the thermal energy. The covalent chemical bond that holds together the atoms in the molecules is much too strong for this purpose: the noncovalent interactions are the basis for any (room temperature) self-assembling process. This provides reversibility and adjustability to the aggregate structures enabling to reach a ordered (meta)stable equilibrium [33]. The obtained supramolecular structures has become a major filed of research in the last quarter of the century motivated by the hope of finding novel properties in functional supramolecular materials [8].

The self-assembly of molecules at a solid surface is generally studied in multifunctional UHV systems in the context of self-assembling on metallic single crystal [34]. The relevant interactions are in a first approximation between the molecules itself and between the molecules and the surface, i.e. the electronic interactions between molecular orbitals and metallic surface states [35]. Photoelectron

## 4.1. PRINCIPLE OF SELF-ASSEMBLY

---

spectroscopic techniques in the energy range of ultraviolet light (20–50 eV) are useful to investigate the binding energy of the outermost molecular levels. The electrostatic interaction between the molecule and the surface can be detected by a modification on the electronic states and by the creation of an interface dipole barrier [36]. The interactions between the molecules and the surface can be investigated by varying the metal [37, 35] or in within the same metal by using different crystal orientations [38]. Another degree of freedom is given by the interaction between neighbor molecules that can be tuned by changing the coverage, by chemical tailoring of side groups [39] or by using intermixed monolayers [40]. This enable to obtain a broad range of supramolecular, two dimensional and highly ordered structures like herringbone pattern or one dimensional lines [41]. These studies usually deal with sub-monolayer coverage in a thermodynamic regime where the growth occurs close to equilibrium conditions and the system have the necessary time to reach a minimum energy configuration. Therefore the electronic as well as the conformational state of an isolated molecule upon adsorption can be compared to (demanding) computational calculations [Ref rr], where different mathematical models, from *ab initio* calculations to density functional theories, can verify their validity [42].

For thicker layers and at higher evaporation rates, the growth is determined by a competition between kinetics and thermodynamics [43]. The kinetics term is given by the ratio between the thermal activated diffusion of the molecules on the surface and the deposition flux. In the kinetics regime (e.g. in case of high deposition rate and low substrate temperature), the formed structures are far away from the thermodynamical equilibrium and can results therefore in polymorphisms, which is a very common feature in organics crystals. These results can hardly be compared to simulations or to theoretical calculation because the complexity of the weak intermolecular inter-

## SELF-ASSEMBLY AND GROWTH OF PENTACENE THIN FILM

---

action and the many degrees of freedom of the systems are to large for the present computational power to be appropriately described.

The growth of organic molecules on polycrystalline metals is much less investigated because of the complications given by the presence of different crystal orientation and grain boundaries. Moreover, SPM techniques are also more difficult to apply in the case of rough surfaces. However, in a first approximation, polycrystalline metals can be described as a ensemble of grains with a distribution of different crystal orientations around an average one forming a textured surface. Knowledge from the literature on single metal crystal can be used, however the influence on the growth of the different facet orientations, the average crystalline size, the ground boundaries and step edge density can hardly be neglected. This is more relevant to practical application and is the main concern of this chapter, where all the metal surfaces and electrodes are obtained by physical vapor deposition of the metal on non-lattice-matched substrate at ambient temperature and are therefore polycrystalline.

In Sec. 4.4.2 and 4.4.3 different morphologies obtained by depositing pentacene molecules on polycrystalline metal substrates and on oxide substrates are presented. In a context relevant to electronics at the nanometer scale, self-assembly processes offer a chance to bridge technological the gap between molecular electronics and bulk plastic electronics []. In this field, also called supramolecular electronics, teh self-assembled structures are considered as ideal building blocks because of the favorable combination between small dimensions and a perfect (ordered) crystalline structures [44]. Moreover, a bottom-up approach is accessible if the components are able to self-assemble between larger structures. This process is exploited in Chap. 5, where the obtained supramolecular nanocrystals connect two prepatterned electrode allowing for characterization of the electrical transport properties.

## 4.2. PENTACENE: MODEL FOR ORDERED ORGANIC SEMICONDUCTORS

---

### 4.2 Pentacene: model for ordered organic semiconductors

Pentacene molecules are the material of choice used in this dissertation because of the excellent charge carrier mobility and because of its ability to form large well-ordered crystalline structure [45]. Its ability to conduct charges is determined by two factors. First, pentacene exhibits a conjugated  $\pi$ -electron system, formed by the  $p_z$ -orbitals of  $sp^2$ -hybridized C-Atoms, which extends over the whole molecule. In a single pentacene molecule, the weakness of the  $\pi$ -bonding results in a lower electronic excitation ( $\pi$ - $\pi^*$  transitions). The occupied  $\pi$  level is also commonly called highest occupied molecular orbital (HOMO), while the unoccupied  $\pi^*$  level is referred as lowest unoccupied molecular orbital (LUMO). As in inorganic solid materials, the electron levels responsible for the electrical conduction are the ones which are closest to the Fermi energy, which lies between the HOMO and the LUMO and characterize therefore the electronic states responsible for the conduction and for the optical properties. The HOMO-LUMO gap in pentacene is found to be 2.7 eV [46]. A difference from inorganic crystals is the weak van der Waals forces between the molecules, which results only in a partial mixing of the orbitals between adjacent molecules and in a reduced transfer integral. This integral is directly related to the effective width of the energy band for charge carrier transport, i.e. the bandwidth. In comparison to inorganic crystals, the reduced bandwidth tends to localize the charges. In this context, the concept of valence and conduction band are replaced by the HOMOs and LUMOs of the organic crystals, which are mainly located at the molecule sites but weakly interacting with each other. Only at low temperature and in case of well ordered purified organic crystals the transport may be described in terms of band transport. Increasing the amount of disorder, either by impurities

## SELF-ASSEMBLY AND GROWTH OF PENTACENE THIN FILM

---

or by grain boundaries, further decrease the bandwidth transforming the band transport to an hopping process. Another way to increase the disorder is by increasing the temperature, which both affect the intramolecular and intermolecular vibrations. Thus, the electrical transport in organic semiconductor greatly depend on the purity of the starting materials but also on the manufacturing process, which lead to imperfections that dominate the intrinsic transport. This is particular important in the case of polycrystalline thin film described in this dissertation.

Besides the excellent mobility, pentacene (as well as other small molecular weight molecules) has also the advantage to be easily vacuum sublimated to a thickness that can be controlled at the mono-layer level as presented in the next sections.

### 4.3 Physical vapor deposition of pentacene

Fig. 4.1(a) shows an overview of the setup used for the sublimation of pentacene. It consists of ① a vacuum chamber provided with ② an evaporation stage and ③ a quartz crystal microbalance (QCMB) (Fig. 4.1(b)) The chamber is pumped by a ⑤ turbo pump down to a base pressure of  $2 \times 10^{-8}$  mbar. The sample is mounted in a ④ linear translation feedthrough that permits to expose or hide the sample from the flow of the sublimated molecules. Additionally, the translation feedthrough can be rotated allowing for the deposition the molecules with an arbitrary angle respect to the surface normal (Fig. 4.1(c)). For in-situ electrical characterization, the devices on a chip are mounted on the ③ chip holder placed at the end of the linear feedthrough . The devices are connected to the external measurements setup via a ⑥ 7-plugs wire feedthrough. This allows a contin-

### 4.3. PHYSICAL VAPOR DEPOSITION OF PENTACENE

---

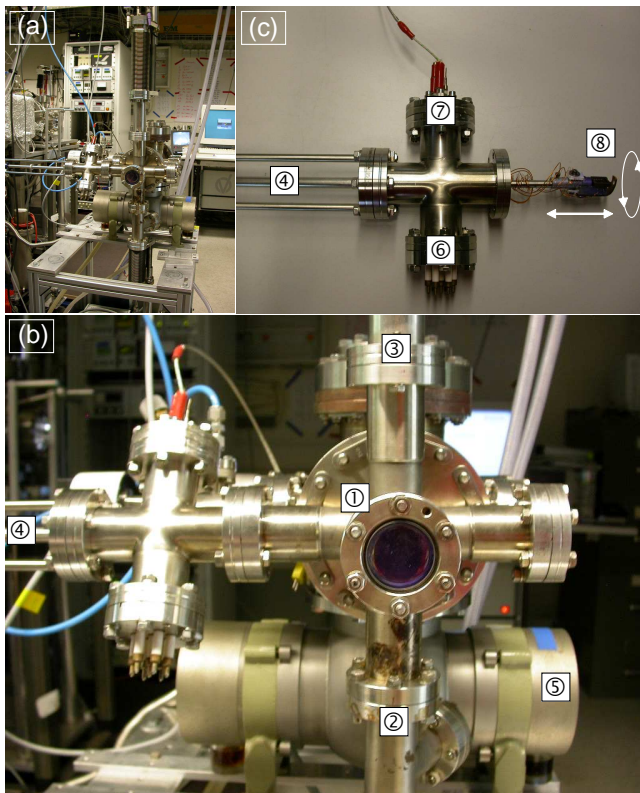


**Figure 4.1:** Setup used for the evaporation of the organic molecules and for the in-situ measurements of the produced devices.

## SELF-ASSEMBLY AND GROWTH OF PENTACENE THIN FILM

---

uous characterization of the devices when the sample is exposed to the molecular flux or placed in the shadowed region. Additionally, an electrical heater is integrated close to the chip and allows for deposition at different substrate temperature. A second  $\odot$  wire feedthrough allows sample heating and temperature controlling by a thermocouple element. In the evaporation stage there are two sources for evaporating or coevaporating two different kind molecules. The sources are made by two metallic chamins brought in thermic contact with two separate electric bottom heaters. Alternatively, a ceramic pot inserted in a metallic coil has also been used instead of the metallic chamin. The chamins are heated by the current driven through the heater which define the temperature of the evaporators (200-300°C ,Ref). By tuning the heating current, the evaporation rate could be set from 0.01 to 1 ML/min. The evaporation rate and the deposited thickness are monitored by the QCMB that is provided by a water cooling system ensuring a minimal thermic load and consequently a more stable frequency signal. The signal is calibrated by tapping mode atomic force microscope. To further improve the precision, the measured signal is averaged over 100s. Because for depositing the molecules the sample has to be introduced between the source and the QCMB, the effective rate and deposited thickness is calculated as the average between the values obtained before and after the deposition. Before starting an evaporation, the rate is allowed for stabilization for  $\sim 1$  h, minimizing therefore the rate fluctuations. The temperature of the sample (25°C for all presented experiments) is measured by the thermocouple element and did not change while the evaporation process.

Prior to the deposition of the molecules on SiO<sub>2</sub> surfaces, the sample are cleaned by a 30 s oxygen plasma in a Oxford PlasmaLab 100 RIE etching system with 10 ccm O<sub>2</sub>, 100 mbar chamber pressure and 100 W radio frequency power. For the deposition on the metal

## 4.4. STRUCTURAL CHARACTERIZATION

---

samples, the freshly deposited metal surfaces are used without additional cleaning. For electrical characterization, the devices are glued by silver paint on a ceramic chip carrier and wire-bonded. All the samples are transferred to the molecules evaporation chamber within 15 min, minimizing the air exposure time.

### 4.4 Structural Characterization

#### 4.4.1 Methods: AFM, SEM and XRD

Tapping mode atomic force measurements (tm-AFM) is a useful tool for the calibration of the deposition thickness of pentacene on  $\text{SiO}_2$  because of the precise measurement of the layer thickness. The instrument used is a Nanoscope DI 3100 scanning station with commercial tips. The height resolution of tm-AFM allows the identification of the growth mode, distinguishing between layer-by-layer growth and multilayer island growth. Larger scans allow the statistical analysis of the height distribution and the extent of the surface coverage. These data are used both for the calibration of the QCMB and for evaluation of the electrically characterized devices.

A major drawback of tm-AFM it is the difficulty of investigations on polycrystalline metals because of the roughness comparable to the height of the pentacene layers. For this purpose, a scanning electron microscope (SEM, *Supra 55 VP*) is used for a quality control of the deposited thin film. Because of the contrast difference in the SEM images, pentacene aggregates are easily recognized both on oxide and on metals. This allows an identification of grain boundaries and measurements of the the island shape and size. It is also very useful in the investigation of the coverage of the edge of the metallic electrodes, which is particularly important for the electrical contact of the electrode to the conduction channel of thin film transistor.

## SELF-ASSEMBLY AND GROWTH OF PENTACENE THIN FILM

---

Moreover, the contrast enable to discern between single, double or multiple molecular layers on oxide. In combination with tm-AFM measurements of the thickness of one layer, it is possible to conclude on the 3-dimensional multilayer shape based on SEM images.

An important question related to the transport properties of pentacene is the determination of the molecular crystal structure with respect to the transport direction. For this purpose, samples obtained by depositing pentacene on oxide and on gold surfaces have been analyzed with x-ray diffractometry (XRD). The measurements have been carried out at the Swiss Light Source MS-X04SA beamline [47], which provides high spectral flux density 5-40 keV x-rays. The energy of the beam was set to 11.8 keV ( $\lambda=1.051 \text{ \AA}$ ), which is just below the  $L_3$  adsorption edge of gold. A crystal-analyzer system, consisting of 5 detectors is used for high resolution data acquirement. The detector and the sample can be independently rotated allowing for  $\theta$ - $2\theta$  scans. After careful alignment of the sample, the  $\theta$  angle could be varied between  $0.3^\circ$  and  $20^\circ$ , where an angle resolution between  $0.01^\circ$ - $0.08^\circ$  was used. From the peaks in the  $\theta$ - $2\theta$  scans that satisfy the diffraction condition the distance between planes in the molecular crystal (parallel to the sample surface) is calculated following the Bragg's law

$$n\lambda = 2d\sin(\theta) \quad (4.1)$$

where  $n$  is the diffraction peak order,  $\lambda$  the x-ray wave length,  $d$  the crystal lattice perpendicular to the surface and  $\theta$  the angle between the incident radiation and the sample.

### 4.4.2 Pentacene on oxide surface

Because of the crucial influence on electrical properties, the growth of pentacene deposited on smooth oxide surfaces has been vastly investigated [48, 49]. It is recognized that pentacene can be grown in a

## 4.4. STRUCTURAL CHARACTERIZATION

---

layer-by-layer fashion with extended two dimensional grains, which in fact decrease the number of grain boundaries. The grain boundaries have a larger number of traps compared to the ordered crystalline domains and have therefore an important influence on to the charge transport [50]. The growth mode and the size of the resulting grains can be controlled by the deposition rate, the substrate temperature [51] and by chemical modifications of the oxide surface [52]. This is of particular importance for the investigation of few ML thin film, where an complete layer is only obtained by a well controlled growth.

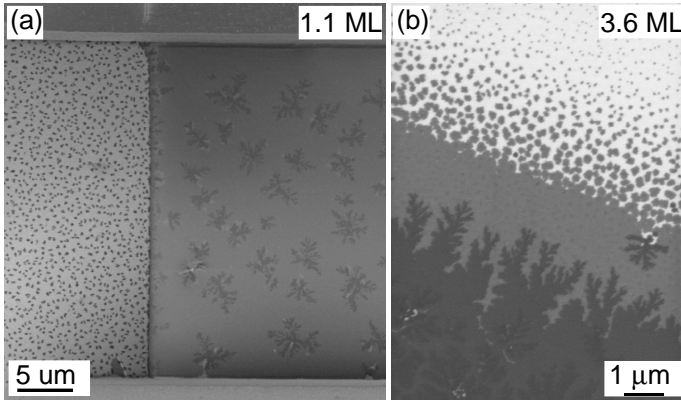
Fig. 4.2(a) shows a SEM micrograph of a device obtained by depositing 1.1 ML of pentacene at a rate of 0.03 ML/min. The channel is homogeneously covered by a first complete layer, with an additional uncomplete second layer in form of dendrimers. The layer-by-layer growth is evidenced in Fig. 4.2(b), where 3.6 ML are deposited through a shadow mask. The top of the picture shows the low coverage area with the SiO<sub>2</sub> appearing in a bright color. The coverage increases toward the bottom part of the picture, where a first, a second and a third layer is visible as layers with increasing dark color. The grain boundaries in the first monolayer are not recognizable either by SEM nor by AFM. The grain size estimated by the nucleation density interfered from the upper part of Fig. 4.2(b) should not be larger than 1  $\mu$ m, but it can not be excluded that a number of the grains merge together forming larger single crystals.

Fig. 4.3(a) shows an AFM measurements of the sample presented in Fig. 4.2(a). The height of a single layer is found to be approximately 1.5 nm (Fig. 4.3(b)), which corresponds very well to the length of a pentacene molecules (15 Å).

These results are also confirmed by XRD measurements on a sample with  $\sim$ 6 ML presented in Fig. 4.4. Because of small thickness of the investigated samples, the peaks are broad. However, three main peaks associated to the pentacene layer can be recognized. The

SELF-ASSEMBLY AND GROWTH OF PENTACENE  
THIN FILM

---



**Figure 4.2:** (a) SEM micrograph of a TFT device produced by depositing 1.1 ML. The channel is homogeneously covered by a complete layer, followed by a second uncomplete one. A gold electrode used for the electrical characterization of the film properties is visible on the left part of the picture. (b) SEM of a second sample produced by depositing 3.6 ML through a shadow mask. The coverage increase from the upper part toward the bottom part of the picture. The transition between uncovered area and exposed area appears as increasing dark colored layer.

#### 4.4. STRUCTURAL CHARACTERIZATION

---

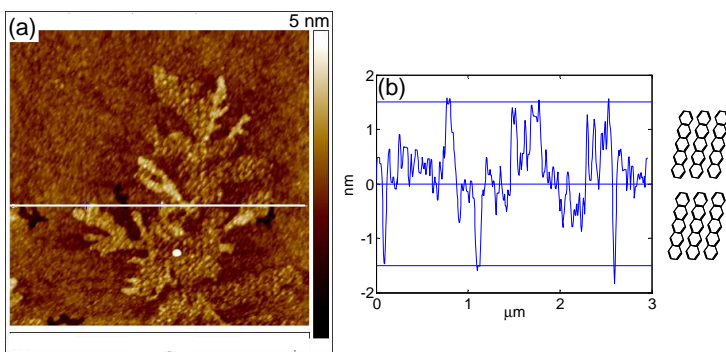


**Figure 4.3:** (a)  $3\ \mu\text{m} \times \mu\text{m}$  AFM scan of the sample presented in Fig. 4.2(a). (b) line scan showing that the surface is almost completely covered by a 1.5 nm layer. The dendrimer growing on top of it is also 1.5 nm height, confirming the layer-by-layer growth mode.

# SELF-ASSEMBLY AND GROWTH OF PENTACENE THIN FILM

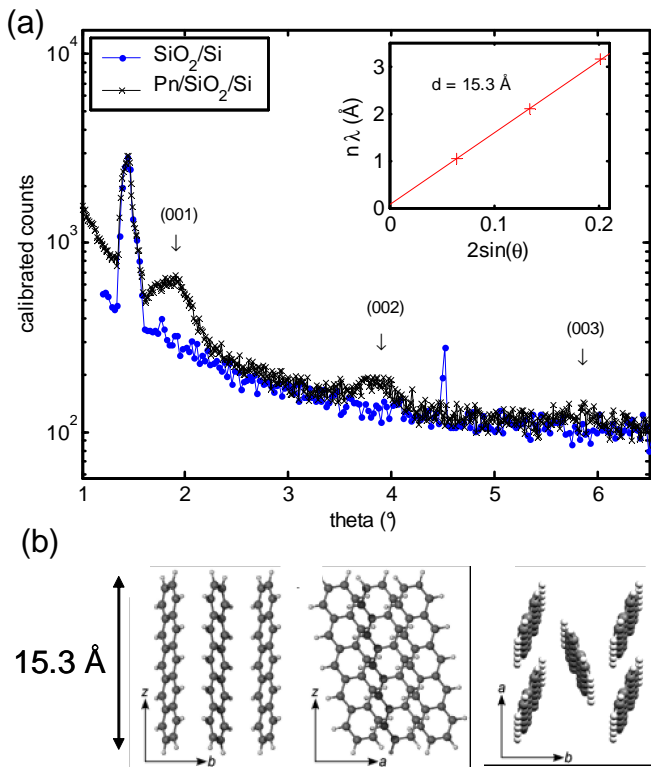


**Figure 4.4:** (a) XRD spectrum of 6 ML pentacene deposited on SiO<sub>2</sub>(50 nm)/Si surface. The peaks corresponding to the pentacene crystal lattice are evidenced. (b) Crystal structure of the thin film phase. Reprinted from [49]

## 4.4. STRUCTURAL CHARACTERIZATION

---

position at  $1.85^\circ$ ,  $3.85^\circ$  and  $5.80^\circ$  corresponds to a lattice constant of the (001) planes of the pentacene crystals of  $15.3 \text{ \AA}$  for the  $1^{th}$ ,  $2^{th}$  and  $3^{th}$  order diffraction peaks, respectively. This is in excellent agreement with crystallographic studies on the pentacene thin film phase [53, 54, 55].

From these results, it is concluded that the produced samples consist of polycrystalline thin film composed by pentacene molecules standing in the upright position. The molecules pack together resulting in ordered monolayer domain that grow in layer-by-layer fashion. These growth conditions are exploited for the production of the few ML thin film transistor presented in Chap. 6.

It is important to note, that the growth is different if the sample are not quickly transferred to the deposition chamber after the last oxygen plasma cleaning process. Otherwise, extended air exposure of the  $\text{SiO}_2$  surface leads to multilayer islands and the production of uniform samples with few ML pentacene coverage is not possible. The contaminations from the environment change the surface composition and consequently the surface energy, which probably change the diffusion/flux ratio and therefore the growth mode.

### 4.4.3 Pentacene on metal surfaces

The growth of ultrathin layers of pentacene on metal substrate differs from the growth on oxide surfaces. On a metal surface, the electronic surface states of the metal extend into the vacuum as evanescent waves, which strongly interact with the molecular orbitals. On gold single crystal, the pentacene exhibit a flat-lying phase [56], where the molecules are oriented with their long axis parallel to the substrate and growth in a layer-by-layer cofacial structure, provided that a balance between intermolecular interaction and molecular surface interaction is achieved. In case of polycrystalline surfaces, this balance can change depending on the details of the surface as shown in this

## SELF-ASSEMBLY AND GROWTH OF PENTACENE THIN FILM

---

section. The metal surfaces studied in this dissertation are polycrystalline gold and palladium surfaces used as electrodes for the TFTs (Chap. 6) and the gold electrode of the nanojunctions (Chap. 3).

The electrodes used in the TFTs are made by depositing on oxidized p-Si substrates 10 nm Ti adhesion layer followed by 200 nm of Au or Pd. For all these surfaces, the deposited pentacene form multi-layers round-shaped islands as depicted in the left side of Fig. 4.5(a), (b) and on Fig. 4.6(a)

The growth of pentacene on metal is important first of all for the characterization of the contact resistance of few monolayer TFT. In such few monolayer film, the morphology of the organic layer at the transition between the metal electrode and the oxide surface is crucial for a good electrical contact between the electrode and the pentacene channel. Fig. 4.5(a) shows an example of a bad contact, which leads to a pronounced contact resistance that strongly limits the performances. The device is obtained by depositing 1.8 ML at a perpendicular direction to the surface. It is recognized from the SEM image that the region close to the interface grow in a peculiar way, with a strong tendency of dewetting. As a consequence, only a small portion of the electrode is connected by pentacene to the channel. Although the electrodes patterning process is developed for obtaining a gently decreasing thickness by using a double layer resist and by rotating the sample during metallization, a local shadow mask effect can decrease the amount as well as the rate of deposited molecules close to the electrode. This problem is minimize by depositing the first half of the pentacene at an angle of  $\pm 30^\circ$ , exposing equally the left and the right contact regions. The process is terminated by the remaining part of pentacene deposited at a perpendicular direction. Increasing the channel thickness to 6-7 ML further increase the extent of the contact between the channel and the electrode as shown in Fig. 4.5(b). The device performance is enhanced, even if the chan-

#### 4.4. STRUCTURAL CHARACTERIZATION

---

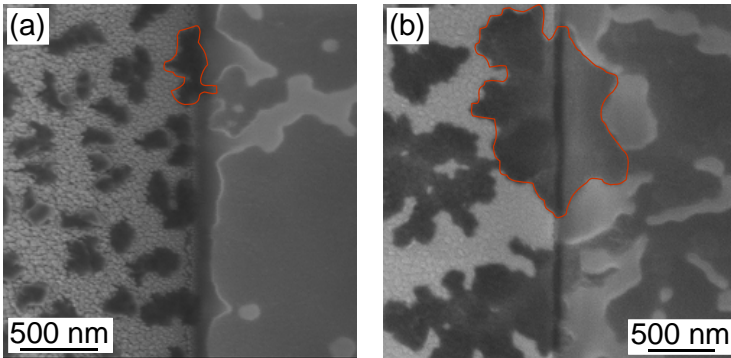


**Figure 4.5:** (a) SEM of a electrode (left) with a bad contact to the pentacene channel (right). Only a small island connect the electrode to the channel. (b) SEM of a good contact, showing that a much larger contact area between the pentacene island on the electrode edge and the pentacene layer on the  $\text{SiO}_2$ . The sample is obtained by partially depositing the pentacene with an angle of  $\pm 30^\circ$  with respect to the perpendicular direction. In this particular sample, an higher amount of pentacene is deposited.

## SELF-ASSEMBLY AND GROWTH OF PENTACENE THIN FILM

---

nel coverage appear less regular probably because of slightly different evaporation condition or surface contamination. The consideration on the extent of the contact area responsible for the injection is important for the investigation of the the contact resistance. Compared to thicker devices or to top-contacted TFT, in few ML TFTs only the region close to the interface, i.e. only the channel width and the pentacene coverage along the edge of the electrode, is important, while the two dimensional geometrical extent of the metal pad is not. The reason is that at these small coverages, the pentacene on the electrode forms disconnected islands and can not contribute to the injection of carriers in the channel.

A completely different growth mode is unexpectedly found by investigation of pentacene deposited on *single gold layer* that is used as the electrodes for the nanojunctions. Only in this case, pentacene self-assemble as several 100 nm-long rods with a diameter of  $\sim 20$  nm (Fig. 4.6(b)). This growth mode (at a fixed growth rate of 0.06-0.08, ML/min) strongly depends on the polycrystalline texture of the surface. This is clearly demonstrated in Fig. 4.6(c), where the metal surface on the left side of the picture is prepatterned by Ti(10 nm)/Pd(200 nm). The whole surface is then covered by 90 nm Au, followed by pentacene deposition up to a nominal thickness of 4.2 ML. On the Au/Ti/Pd/SiO<sub>2</sub> surface, pentacene grows in 3-dimensional islands as illustrated above. However, on the Au/SiO<sub>2</sub> surface, the molecules self-assemble in the form of nanorods.

It is worth to point out that the Au surfaces both sides, with and without prepatterned Pd/Ti layer, are prepared in identical conditions with the pentacene deposited in the same run. Moreover, a gold thickness of 90 nm ensure a complete coverage of the underlying surface and a floating effect or diffusion of the underlying metal while gold deposition is not found in the literature. The self-assembly of pentacene on a metal substrate critically depends on the elec-

#### 4.4. STRUCTURAL CHARACTERIZATION

---

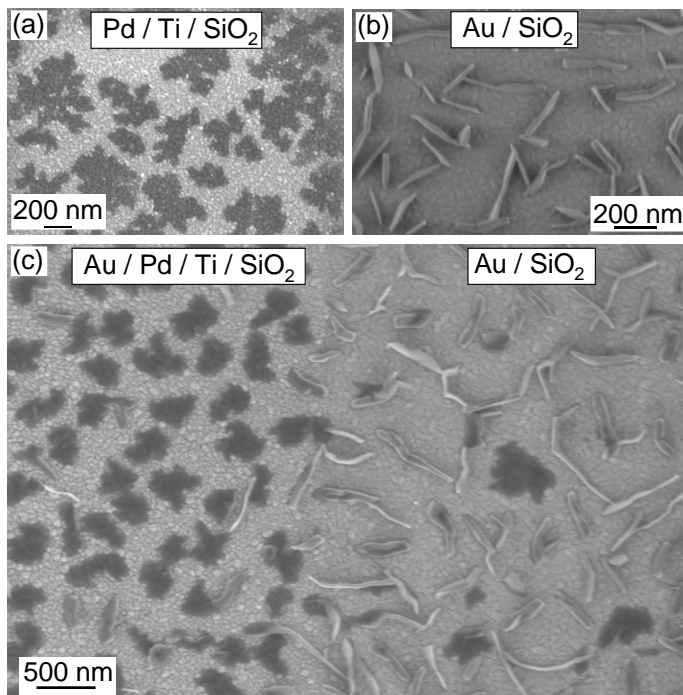


**Figure 4.6:** SEM micrographs of pentacene deposited on different metal surfaces covering a SiO<sub>2</sub> substrate. (a) 1.4 ML deposited on Pd(200 nm)/Ti(10 nm). (b) 4.1 ML on Au(90 nm). (c) 4.2 ML deposited on Au(90 nm). The Au layer extend over the all sample, but on the left side, the surface is prepatterned by a Pd(200 nm)/Ti(10 nm), while on the right side Au is directly evaporated on SiO<sub>2</sub>.

## SELF-ASSEMBLY AND GROWTH OF PENTACENE THIN FILM

---

tronic structure of the metal [35]. Possibly, diffusion and self-assembly also depend on the crystallographic orientation and on the step edge density. XRD of gold deposited directly on  $\text{SiO}_2$  reveals a preferred (111) orientation, with additional other crystal facets, grain boundaries and step edges as visible in the SEM pictures. By tm-AFM measurements, the average roughness  $R_a$  for the Au/ $\text{SiO}_2$  and Au/Pd/Ti/ $\text{SiO}_2$  surfaces is found to be  $1.5 \pm 0.5$  nm and  $3.5 \pm 0.5$  nm, respectively. It is therefore plausible that the density of other crystal orientations and/or type of defects on the metal surface differ. The growth of the pentacene nanorods is apparently controlled by a delicate balance between the diffusion of the molecules on the textured metal surface and  $\pi$ - $\pi$  interactions between the molecules. The different diffusion of pentacene on the two surfaces is also suggested by a close inspection of the SEM picture. The gold grains are better visible on the Au/Pd/Ti/ $\text{SiO}_2$  surface, indicating that 1-2 ML of pentacene completely cover the Au/ $\text{SiO}_2$  surface. Unfortunately, it was not possible to determine the crystal structure of the nanorods by XRD. The  $\sim 100$  nm gold layer, necessary for the particular growth of the nanorods, increases the reflectivity of the surface at small angles by several orders of magnitude. The intensity of the reflected x-rays mask the scattered signal from the pentacene crystal and no peaks corresponding to the pentacene layer could be identified. This makes a determination of the pentacene orientation (parallel or perpendicular to the surface) impossible. However, it is safely concluded that a small differences in the average atomic crystalline structure of a polycrystalline metallic surface directly influences the molecular self-assembling of nanoscale object by a delicate energetic balance. This provide thus an interesting method to control a surface-mediated self-assembly process by physically tailoring the substrate.

It was found out later, that the growth of pentacene nanorods was already observed [57, 58]. However the use of such self-assembling

#### 4.4. STRUCTURAL CHARACTERIZATION

---

was not recognized. In the next Chapter, this self-assembling process is exploited to grow nanorods across the nanojunction devices and to characterize the charge transport in organic semiconductor at the nanometer scale.



# Chapter 5

## Electrical transport through self-assembled pentacene nanorods

In this Chapter, the self-assembly properties of pentacene are exploited to obtain nanorods that bridge the gap of a metallic nanojunctions, allowing for the investigation of the electrical transport properties. The characterization is performed in-situ, in air and in a cryostat with temperature ranging between 298 K and 100 K. Depending on the doping of pentacene, either by air contamination or coevaporation with a dopant molecules, different transport mechanisms are observed.

## 5.1 Contacting pentacene nanorods by a metallic nanojunction

As presented in Sec. 4.4.3, pentacene deposited at a rate of  $\sim 0.1$  ML/min on a single layer gold surface self-assembles in a form of 20-nm wide, several 100-nm long nanorods. When the deposition is performed on a metallic nanojunction, the nanorods can grow across the gap connecting the two electrodes. The deposition angle was set between  $0^\circ$  and  $+30^\circ$  in order to facilitate the bridging of the gap. An example of the nanorods devices obtained by undoped pentacene is presented in Fig. 5.1(b), where it is recognized that nanorods in the junction area are sometimes wider than what is obtained on the planar surface. Nevertheless, the  $3\text{-}\mu\text{m}$  wide electrodes are connected by  $\sim 7$  nanorods for a total width of  $\sim 800$  nm. Fig. 5.1(a) shows a schematic drawn of the nanojunction. Devices based on pentacene doped by  $F_4\text{TCNQ}$  (the molecular structure and the energy levels are presented in Sec. 6.4) have also been obtained by coevaporation of the two molecules in a 3% ratio. It was found that the doped pentacene also forms islands but self-assemble in a flatter and less regular shape as depicted in Fig. 5.1(c). The different shape can be explained by the relatively high doping ratio and its influence on the crystal structure. However, the aspect ratio and the nanorods-electrode contact area are similar (within a factor 2) and can not explain the very different electrical transport properties presented below.

## 5.2 Current-voltage measurements of undoped and doped nanorods

The electrical characterization is performed by the measurements of current-voltage characteristics ( $I - V$ ) of the devices using a

## 5.2. CURRENT-VOLTAGE MEASUREMENTS OF UNDOPED AND DOPED NANORODS

---

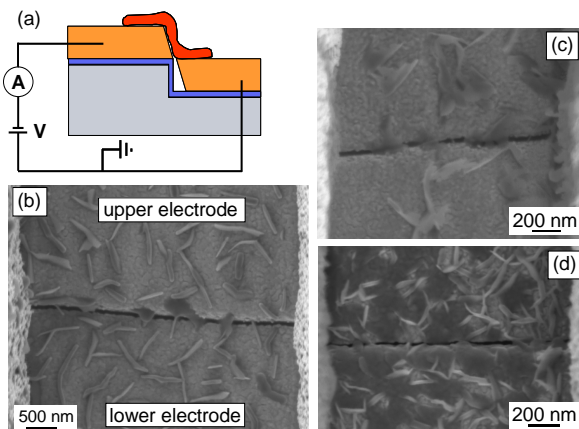


**Figure 5.1:** (a) Drawn of the nanojunction devices used for measuring the transport properties of pentacene nanorods. (b) SEM micrograph of a nanorods device. The pentacene molecules (nominal thickness  $\sim 6$  ML) self-assemble in form of nanorods that grown over the gap of the nanojunction connecting the two electrodes. Upper electrode is referred to the gold electrode above the step, while lower electrode is at the bottom of the sidewall of the step. (c) SEM of a  $F_4TCNQ$  doped pentacene device showing the different shape of the self-assembled islands. However, both undoped and doped nanorods have similar contact area to the metal electrodes. (d) SEM of a thick undoped pentacene nanojunction obtained by depositing  $\sim 20$  ML at a rate of  $0.7$  ML/min.

## ELECTRICAL TRANSPORT THROUGH SELF-ASSEMBLED PENTACENE NANORODS

---

**Kethley 236** as a voltage drive source meter for controlling  $V_{sd}$  and measuring  $I_{sd}$  with sub-pA precision. In order to keep this current resolution and to limit the parasitic capacitance, the instrument, which is provided with triaxial cables, is connected to the sample by using appropriate cables, feedthrough and connectors. In the part of the setup where the use of triaxial cables was not possible (e.g. inside the evaporation chamber and in the cryostat), single separated wire with a thin insulation provide a satisfactory current resolution since the external noise is shielded by the metallic chamber. High voltage feedthrough are found to shows significant lower current leak compare to compact multi-pin feedthrough and are therefore preferred. The leakage current through the substrate is measured using a **Kethley 2400**. The data are acquired at a rate of  $\sim 1$  measurement/sec by a laptop provided with a *Labview* program that controls both instruments. Three different measurement setup configurations are used: the in-situ characterization setup (Fig. 4.1), a commercial probe station for the measurements in air and a cryostat for the temperature dependent characterization. For all three setup, the same measurements units are used. The bias applied between the upper and the lower electrode was swept at 0.05-0.2 V/s between  $\pm 2$  V for the undoped devices and between  $\pm 1$  V for the doped ones.

Fig. 5.2(c) and (d) show the  $I - V$  of an undoped and a 3% F<sub>4</sub>TCNQ doped pentacene nanojunction devices measured in vacuum and in air, respectively. The device obtained from pure pentacene measured in vacuum shows an insulating behavior with current below 5 pA for bias voltage up to 2 V. Since the current measured on an empty device (before the deposition of the pentacene) is even smaller, the hysteresis and the current intensity recorded is related to the undoped nanorods and is not an experimental artefact. The organic semiconductor is in this condition depleted of carriers. This observation is supported by the investigations on thin film transis-

## 5.2. CURRENT-VOLTAGE MEASUREMENTS OF UNDOPED AND DOPED NANORODS

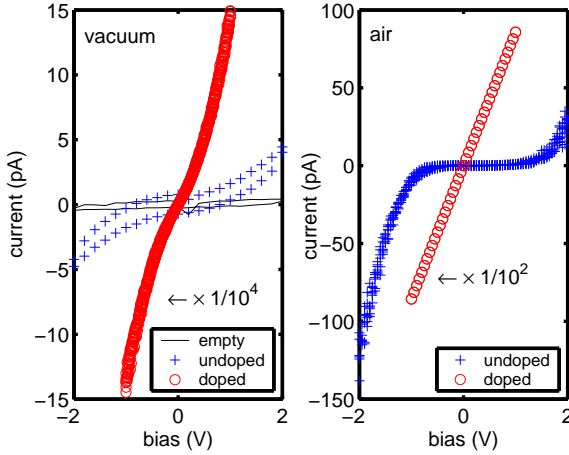


**Figure 5.2:** (a)  $I - V$  of undoped and doped pentacene nanorods measured in vacuum. Comparison between the current measured in an empty device (before the pentacene evaporation) and the undoped pentacene nanojunction shows that the hysteresis and the current intensity recorded is related to the nanorods and is not an experimental artifact. Undoped nanorods show a highly insulating (Schottky) behavior, whereas in doped pentacene the conduction increased by a factor  $10^5$ . (b)  $I - V$  of undoped and doped pentacene nanorods measured in air. Undoped pentacene exhibits a rectifying behavior, while a fully linear ohmic  $I - V$  is recorded for doped pentacene. Upon exposure to the air, the conduction of the undoped pentacene (at  $V = \pm 2$  V) increases by a factor 5-25, while the conduction of the doped pentacene decreases by a factor 20.

## ELECTRICAL TRANSPORT THROUGH SELF-ASSEMBLED PENTACENE NANORODS

---

tor (TFT) based on the same material and at similar conditions. The transfer characteristics of undoped pentacene TFT presented in Sec. 6.4 indicates a normally-off transistor ( $I_{sd} = 0$  at  $V_g=0$ ), i.e.  $V_{g,th} < 0$ .

Upon doping, the current in the nanojunction increases to 150 nA at 2 V. The effect is related to charge carriers that are introduced by the doping process. Again, this can be compared to the positive values of  $V_{g,th}$  of the doped TFT presented in Sec. 6.4 and to the related charge carrier density  $p_0=4.8 \times 10^{18}$  1/cm<sup>3</sup> that can be estimated for a 3% doped pentacene. This increase is assigned to the doping-induced increase of the charge carriers density generated by a charge transfer mechanism between the pentacene matrix and the dopant [59]. This interaction is investigated in detail in Chap. 6 and Chap. 8. In vacuum, the symmetric  $I - V$  of the doped nanojunction shows a transition from a linear regime below 0.2 V to a power law at higher bias voltages ( $I \propto V^\alpha$  with  $\alpha = 1.7 - 1.8$  at  $V = \pm 1$  V).

This could be interpreted either as an indication for the trap filling regime before the onset of a space charge limited current (SCLC) [60, 61] or as a Poole-Frenkel (PF) effect [62]. SCLC are usually only possible in the most rigorously purified single crystal, which is not the case here. However, the small channel length may be favorable to SCLC in spite of PF. Following Gregg *et al.* [63], the discrimination can be made by comparing the charge carrier concentration  $p$  induced by both mechanisms. For this purpose, the  $I - V$  are first fitted by the PF model

$$J = eF\mu_0 p_{b,0} \exp((-E_{a,0} + \eta F^{1/2})/kT) \quad (5.1)$$

where  $J$  is the current density ( $I/(Wd)$  with the width  $W=600$  nm and the thickness  $d=10$  nm),  $F$  is the electric field ( $V/L$  with  $L=10$  nm),  $\mu_0$  the mobility,  $p_{b,0}$  the charge carrier density at zero field (estimated

## 5.2. CURRENT-VOLTAGE MEASUREMENTS OF UNDOPED AND DOPED NANORODS

---

above),  $E_{a,0}$  the activation energy and  $\eta$  describes the dependence of  $\mu$  and  $p$  on  $F^{1/2}$ . By setting  $\sigma_0 = e\mu_0 p_{b,0}/(Wd) = 7 \times 10^{-8}$  S found by extrapolating the conductance at zero bias, the fit provides  $E_a/kT = 11$  meV and  $\eta = 2.77 \times 10^{-5}$  eVcm/V $^{1/2}$ .

Since SCLC requires the bulk charge density  $p_{b,F} = p_{b,0} \exp(\eta F^{1/2}/(kT))$  to be insignificant compared to the injected carriers density  $p_{inj,F} = F\epsilon\epsilon_0/(eL)$ , the ratio

$$\xi = \frac{p_{b,F}}{p_{inj,F}} \quad (5.2)$$

needs to be much smaller than 1 for SCLC. After analysis of the data, it is found  $\xi > 1$  for all the applied bias for the nanojunction measured in vacuum, which would indicate a PF current. For doped pentacene exposed to the air, the lack of knowledge on  $p_{b,0}$  and  $\mu_0$  makes this analysis impossible. Moreover,  $\xi$  is quite sensitive to the uncertainty in the actual device geometry. It is therefore concluded, that the  $I - V$  are not pure SCLC nor PF but an interplay between both mechanisms probably exists. The important observation is that both type of descriptions are related to a bulk effect, i.e. the contact resistance in the doped pentacene nanojunction seems at least comparable to the bulk part. This issue will further be discussed in Sec. 5.4.

For the undoped nanojunctions measured in air, a finite conduction is recorded, probably because of charge carriers induced by an effect of moisture, oxygen and light [64, 65]. From the TFT characteristics presented in Sec. 6.5, a charge carrier concentration of  $\sim 3 \times 10^{17} \text{ cm}^{-3}$  is calculated, which is lower compared to the F<sub>4</sub>TCNQ doped pentacene (Sec. 6.4.2). The measured  $I - V$  are strongly non-linear and asymmetric. By a 3% F<sub>4</sub>TCNQ doping, the conduction is enhanced by a factor  $10^3$ - $10^5$  and shows an Ohmic behavior. This implies that the dopant molecules has a fundamental influence to the

# ELECTRICAL TRANSPORT THROUGH SELF-ASSEMBLED PENTACENE NANORODS

---

transport properties on the nanometer scale.

To gain insight on the transport mechanism, temperature dependent measurements are presented in the next Section.

## 5.3 Temperature dependence of the conductivity

### 5.3.1 Experimental setup

For the temperature dependent studies, all the sample have to be transferred from the evaporation chamber to the low temperature measurements setup, exposing therefore the samples to the air for about 5 min. The setup consists of a close cycle He-cryostat (Janis xxx) with a base pressure below  $1 \times 10^{-6}$  mbar. The same measurements units as for the in-situ characterization is used.

### 5.3.2 Results on doped pentacene

Fig. 5.3(a) shows the  $I-V$  of a doped nanojunction measured at temperatures ranging from 298 K to 101 K. The curve are linear, showing an Ohmic conduction for all investigated temperatures. If a simple thermal activated transport  $I(T)/V = G(T) = G_0 \exp(-E_a/(k_B T))$  is assumed, the activation energy  $E_a$  can be calculated from the slope of the Arrhenius plot  $\log(G(T))$  vs.  $1/T$ . The results presented in Fig. 5.3(b) show that this model fits very well the transport in the doped nanorods device with an activation energy  $E_a = 128 \pm 4$  meV. By comparing the conductance before and after the thermal cycle, a 10% lower conductance after the cycle is recorded, which indicates an acceptable low degradation.

### 5.3. TEMPERATURE DEPENDENCE OF THE CONDUCTIVITY

---

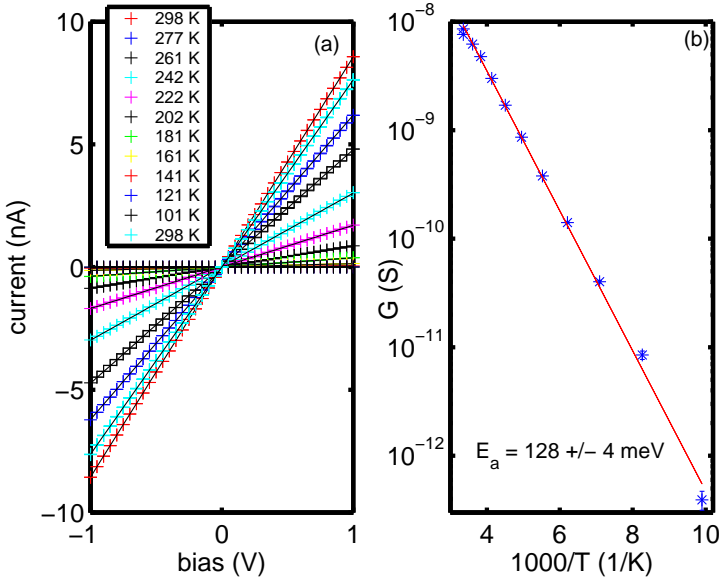


**Figure 5.3:** (a) I-V characteristics of a doped pentacene nano-junctions measured at temperature between 298 K and 101 K. A striking linear behaviour is observed at all temperatures. (b) Arrhenius plot of the conductance showing a thermal activation energy of  $128 \pm 4$  meV.

## ELECTRICAL TRANSPORT THROUGH SELF-ASSEMBLED PENTACENE NANORODS

---

### 5.3.3 Undoped pentacene nanorods

The transport mechanism in undoped pentacene nanorods device is very different from the doped ones. The asymmetry, already presented in Sec. 5.2, further extends to the temperature dependence. Fig. 5.4(a) shows the  $I - V$  measured at temperatures between 298 K and 200 K. The raw data has a quite large scatter (cf. the  $I - V$  of undoped nanorods in air in Fig. 5.2), therefore an averaging procedure over three consecutive scans is applied. In Fig. 5.4(b) the current measured at different bias is plotted versus the inverse of the temperature. An Arrhenius model describing the transport requires that the points, representing the current measured at the same bias, should be aligned, where the slope of the line represents the activation energy. This is clearly not the case, and the transport mechanism appears to be more complicated. The slope of the curve in Fig. 5.4(b) is attributed to some activation energies (that depend on temperature and on bias). The transport is almost temperature independent for negative bias, while for positive bias the activation factor reaches  $\sim 300$  meV for intermediate temperature. The increase of the conductivity in some T-range could be ascribed to the electrical instability of the nanorods, probably given by some charges in the contact region caused by the applied bias. However, the observation of different transport between positive and negative voltages is evident and is not influenced by changes in the contact region.

Although the experimental  $I - V$  curves could be reasonably fitted by a Fowler-Nordheim model (field assisted injection through a triangular shape energy barrier) for negative bias and by a Richardson-Schottky model [66] (thermionic emission over an image potential lowered energy barrier) for positive bias, it is difficult to unambiguously determine a transport mechanism. Moreover, the measured temperature dependence is not well described by these models. It was shown that the obtained fitted parameter differs by order of magnitude from

### 5.3. TEMPERATURE DEPENDENCE OF THE CONDUCTIVITY

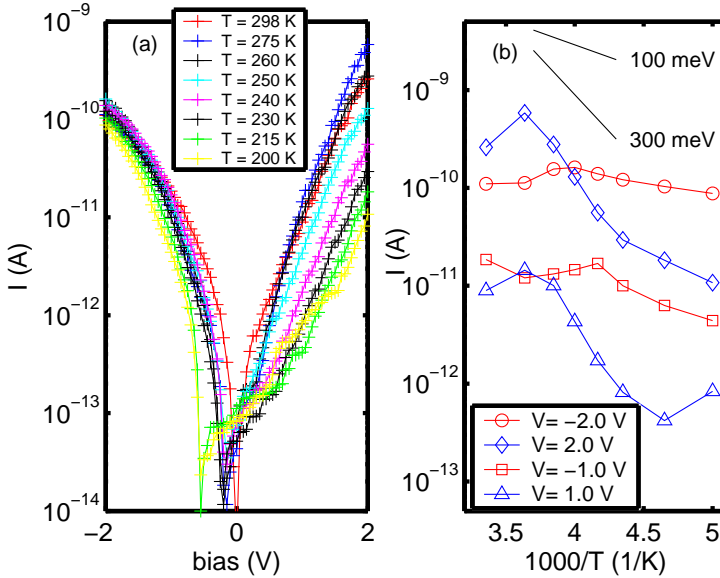


**Figure 5.4:** (a) I-V characteristics of a pentacene nanorods device measured at temperature between 298 K and 200 K. The I-V curves are nonlinear and asymmetric. (b) The conductance does not follow a simple thermal activated behavior. Rather, the transport appears to be almost not temperature dependent for negative bias (red symbols). A more complicated transport is found for positive bias (blue symbols), where the activation energy reaches  $\sim 300$  meV for intermediate temperature.

## ELECTRICAL TRANSPORT THROUGH SELF-ASSEMBLED PENTACENE NANORODS

---

theoretical ones [67], which cast a serious doubt on the application of such models in the case of metal-organic semiconductor interfaces. Therefore, the obtained results will only be qualitatively described.

It is noted by close inspection of the SEM image (Fig. 5.1(b)), that most of the nanorods have larger contact area to the upper electrode compared to the bottom one, probably as a consequence of the electrode geometry and the growth mode of the nanorods. The hypothesis that the different contact explain the asymmetric  $I - V$  characteristics is discussed in Sec. 5.4.

To support this hypothesis, thick pentacene devices are produced by depositing  $\sim 20$  ML (deposition rate  $\sim 0.7$  ML/min) of pentacene on a similar metallic nanojunction. The thick devices show that the gold surface and the gap region are almost completely covered with pentacene (Fig. 5.1(d)). Thus, the pentacene has similar contact on both sides. As expected, the measured  $I - V$  are much more symmetric as depicted in Fig. 5.5(a). The temperature dependent transport can be fitted at high bias by an Arrhenius model. In contrast to the doped nanorods devices, the conductance  $G$  depends here on both the temperature and on the bias. The results are presented in Fig. 5.5(b). For bias exceeding 1 V, an activation energy of 270-410 meV is found, which is slightly larger for positive compared to negative bias. In this regime the activation energy decrease with increasing bias. This observation indicates a barrier lowering by the applied field. The effect is experimentally similar to the Schottky barrier lowering in inorganic semiconductor, but the exact injection mechanism between a metal electrode and an organic semiconductor is different [68]. At bias below 1 V, the Arrhenius model is less accurate, either because of experimental errors or because of a different injection mechanism. A discussion on the different injection processes observed is presented in the next section.

### 5.3. TEMPERATURE DEPENDENCE OF THE CONDUCTIVITY

---

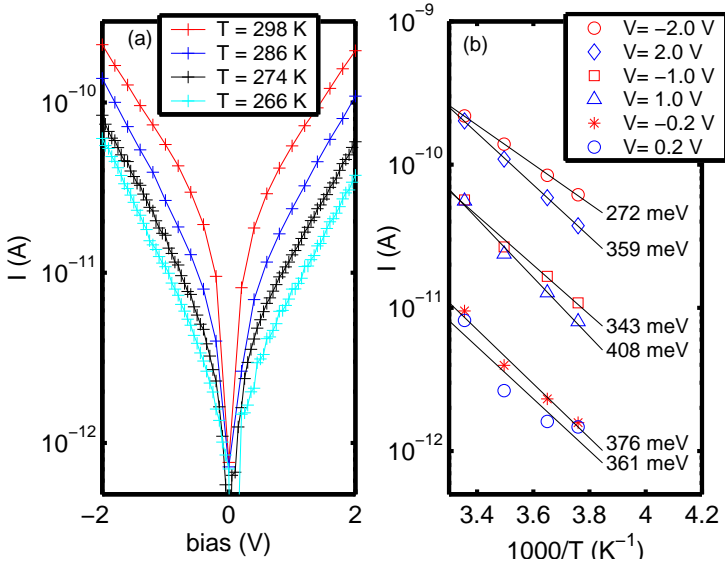


**Figure 5.5:** (a) I-V characteristics of a thick ( $\sim 20$  ML) pentacene nanojunctions measured at temperature between 298 K and 266 K. The I-V curves are nonlinear but almost symmetric. (b) The current at different bias voltages shows a thermal activation energy of 300-400 meV.

## 5.4 Possible transport mechanism

In this section, a possible mechanism for the transport observed in undoped and doped pentacene nanorods devices is discussed.

The first general consideration is on the size of the devices. As the channel length  $L$  is reduced, the interfaces become predominant for the transport properties. This is because the total resistance  $R_{tot}$  is the sum of the contact resistance  $R_c$  and the resistance of the bulk part  $R_b$ , which depends on  $L$ . Reducing  $L$  increase the ratio  $R_c/R_{tot}$ . It is known from literatures, that short channel effects start to play an important role in organic TFT with sub- $\mu\text{m}$  channel length [69]. Since the here presented devices has  $L$  in the 10 nm range, it is not surprising that the interface is the bottleneck for the charge transport. The second indication is based on the measured  $I - V$ . Usually, asymmetric  $I - V$  characteristics are obtained by using as electrodes two metals with different work function. This is accomplished by a sandwich structure with two different metals, as it is the case in an organic light emitting diode or in photovoltaic devices. Asymmetric  $I - V$  are also observed by a combination of a clean electrode and a contaminated one. In both cases, the work function of the actual metal surface influences the energy level alignment of the metal-organic interface creating a build-in potential. In the here presented devices, however, the two gold contacts have a similar amount of contaminations coming from the brief exposure to the air prior and after the pentacene deposition. Consequently, the electrodes should exhibit the same work function. Nevertheless, the asymmetry has to arise from contact properties, since the bulk do not discriminate between the flow in opposite directions. There is the possibility of bipolar current caused by positive and negative bias, i.e. of transport of holes and electrons, which in general have different mobilities and causes therefore different current intensity. Even if the transport in the 10 nm range could be different, the TFT transfer characteristics

## 5.4. POSSIBLE TRANSPORT MECHANISM

---

presented in Chap. 6 suggest that holes are the main charge carriers in gold-pentacene-gold devices. Moreover, the results on the thick nanorods devices also imply that in case of similar contact on both sides, the asymmetry disappears. It is therefore concluded, that the transport in nanojunction device based on pentacene is determined by  $R_c$ , i.e. it is limited by the charge injection from metal to pentacene at the contact. In other words, studying the transport in nanojunction gives information about the injection properties of the metal-organic interface. The injection is governed by the HOMO alignment, interface dipoles and charge carrier concentration [68] or, more in general, by the shape of the energy band near the interface, by the barrier height and by the related depletion width. In a rough approximation, the depletion width  $W$  at a metal-organic interface is determined by

$$W = \sqrt{(2\epsilon\epsilon_0\phi)/(pe)} \quad (5.3)$$

where  $\phi$  is the band misalignment,  $\epsilon$  the dielectric constant of pentacene,  $p$  the charge carrier concentration and  $e$  the electron charge. As  $p$  is increased,  $W$  decreases and charges can more easily tunnel through the thinner barrier. As an estimation, the depletion width  $W$  in the case of undoped pentacene exposed to the air, estimated from  $p_0 = 3 \times 10^{17}$  and  $\phi=0.4$  eV, is 15 nm. It should be noted, that this relation follows from the Poisson equation applied to a planar bulk junction. For a one-dimensional geometry, a deviation from this behavior has been both predicted [70] for carbon nanotubes. If this has to be applied in a 10 nm organic semiconductor is still unclear. The band misalignment [71] measured in UHV conditions is found to be 0.47 eV [46]. Since the sample measured in these works has been exposed to the ambient air, the contaminants probably reduce the electronic interaction between the metal and the pentacene molecules. The activation energy of 0.4 eV measured for the thick nanojunction is therefore in good agreement with the spectroscopy

## ELECTRICAL TRANSPORT THROUGH SELF-ASSEMBLED PENTACENE NANORODS

---

experiments.

In the specific case of the thin nanorods devices, the nanorods-lower electrode contact, which has the smaller contact area, is more exposed to the environment. As a consequence, the concentration of the ionized dopants on the nanorods-lower contact is higher compared to the nanorods-upper contact. In the experiments, the voltage bias was always applied to the upper electrode (drain), while keeping the lower one at ground (source). Thus, the width of the depletion layer is considerably smaller on the source side compared to drain side. A possible band diagram is presented in Fig. 5.6. By applying a negative bias voltage, the charge carriers (holes) have to be injected from the source where the width of the depletion layer is smaller, allowing a direct tunneling through the barrier. This tunneling process is inherently temperature insensitive, consistent to the experimental data. In contrast, by applying a positive bias voltage, holes have to be injected from the drain where the width of the depletion layer is too large for a direct tunneling. Therefore the charges have to overcome a barrier by a thermally activated process characterized by an activation energy. This is also the case for the contacts in the thick devices, where both electrodes have a large contact area to the pentacene and the interfaces are therefore less exposed to the air. Consequently, the smaller charge carriers concentration and a higher depletion width determine an almost symmetric  $I-V$  and an Arrhenius-like activation energy.

This picture follows directly from the theory on inorganic semiconductors. For metal-organic semiconductor interfaces, the situation is more complicated because of the localized nature of the charge carriers. In fact, the injection process involves a combination between a thermionic emission process and a tunneling process, where the crucial first injection event is thermally assisted tunneling into a distribution of localized states [68, 13]. The energy barrier that a

## 5.4. POSSIBLE TRANSPORT MECHANISM

---

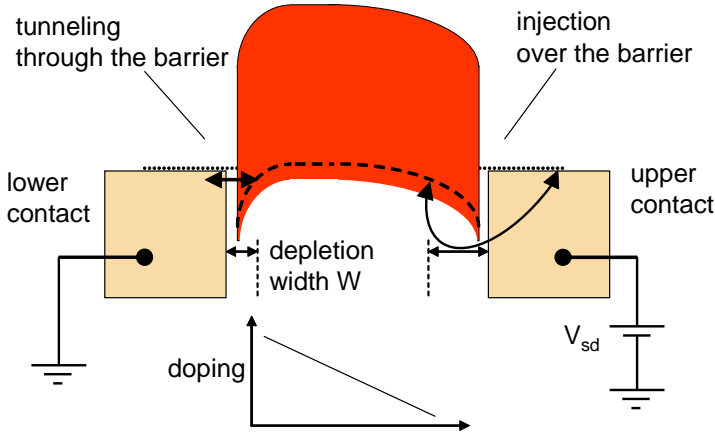


**Figure 5.6:** Possible energetic levels of pentacene nanorods connected between 2 electrodes. On the left side (lower electrode in fig. 5.1(b)) the nanorods-electrode contact is smaller and therefore more exposed to environment doping. The carrier concentration at this side is higher, which shrink the depletion width enabling direct tunneling through the barrier. This process is not temperature dependent. On the right side (upper electrode in fig. 5.1), the depletion width is bigger and the carrier must be thermally injected over the barrier.

## ELECTRICAL TRANSPORT THROUGH SELF-ASSEMBLED PENTACENE NANORODS

---

charge has to overcome or pass depends on many details, like the energy level alignment between the metal Fermi level and the first layer of molecules (charge neutrality level [72], the metal induced broadening of the density of the gap states in the first layer of molecules [73] and the dopant induced dipolar disorder [74]. In low mobility disordered organic semiconductors, also the back diffusion of the injected carriers driven by the image charge potential has to be considered. This could also play a role in the interface region, where the mobility can be reduced by the impurities. However, even if a detailed description is complicated, the general observation that doping reduce the injection barrier holds also for the injection in the nanojunction presented here.

As state above, the transport in nanojunction probes the injection properties of the metal-organic interface. It is not obvious if this is true also for doped pentacene.

The  $I - V$  of F<sub>4</sub>TCNQ doped pentacene measured in vacuum (Fig. 5.2(a)) show an indication of SCLC or PF related phenomena, which is a bulk effect. After exposing the device to air, the conductance decreases and a fully linear  $I - V$  is measured, which is also an indication of bulk transport. On the other hand, by scaling the measured  $R_c$  (Chap. 7) to the nanojunction geometry, it is found that even if  $R_c$  is substantially reduce by doping, it is comparable to the resistance of the channel, i.e. the nanojunction remains injection limited. However, it should be noted, that a precise comparison of  $R_c$  between TFT and nanojunction devices is not straightforward, as the arrangement of the pentacene molecules may be not comparable and the higher field in a small length scale could modify the barrier.

The question remains even if the transport at variable temperatures is considered. The  $I - V$  remains linear (within the measurement accuracy) to the lowest measured  $T$ . A linear  $I - V$  is a sign either of bulk transport or a tunneling process. By assuming a tun-

## 5.4. POSSIBLE TRANSPORT MECHANISM

---

nel process, the thermal activation energy has then corresponds to the T-dependence of the barrier width. The problem is that a linear  $I - V$  based on a tunnel process requires  $G = I/V \sim \exp(-W)$ , where  $W$  is the barrier width, and the experimental observation of  $G \sim \exp(-1/T)$  implies  $W \sim 1/T$ . This is not consistent with a Schottky-like barrier determined from  $W \sim p^{-1/2}$  by thermally activated carriers  $p \sim \exp(-1/T)$ . By assuming the thermal generation of  $p$ , then one has to conclude that  $W = -\log(p)$ . Curiously, this behavior was observed in doped carbon nanotubes and was attributed to 1-dimensional nature of the system [70]. However, it is hard to believe that this would also applied in the present situation. A more plausible explanation can be found in a thermally assisted tunneling mechanism [75, 76]. The linear  $I - V$  could be a consequence of multiple tunneling processes, while the thermal activation part come from the energy difference between the mean energy level of the carrier and the transport level. However, it is not clear why by increasing filed the activation energy stays constant.

In conclusion, it is difficult to clarify if the transport in doped pentacene nanojunctions in limited by the contact or by the channel. Available literature data on similar structure with comparable channel length are very limited, and non of them comments on linear  $I - V$  of organic semiconductors. In any case, the important finding is that the transport in a 10-nm length scale shows a linear, high current density  $I - V$  upon doping with F<sub>4</sub>TCNQ. These properties are well suited for a good injection of charges carriers into the organic semiconductor and may be important for future applications.

For a field and temperature dependent quantitative measurement of the contact resistance in this material system, organic thin film transistors with undoped and doped pentacene are investigated in the next chapters.



# Chapter 6

## In-situ doping of a few monolayer pentacene thin film

In-situ characterizations of thin film transistor (TFT) are presented in this chapter. Experiments with ultrathin active channel represents a new method for the investigation of doping phenomena in a few monolayer (ML) organic semiconductors, in a similar way to what has been recently discussed for inorganic semiconductors [77]. In combination with the transmission line method, this approach permits to study the effect of dopant molecules on the mobility and the injection efficiency at the nanometer scale.

## 6.1 Thin film transistor: introduction and working principle

### 6.1.1 Design

The electrical transport properties of organic semiconductor have often been characterized using the investigated molecules as the active materials in the channel of a field effect transistor (FET). Such transistors consists of two contacts, source and drain, separated by a defined distance (called the channel length  $L$ ) and connected together by the semiconductive channel. A third electrode, the gate electrode, is separated from the channel by an insulating layer and allows the modulation of the channel conductivity. Typically, a  $\text{SiO}_2$  or a  $\text{SiN}$  insulating layer is used, but recently high dielectric nanocomposite [78] or self-assembled monolayers [79] have been explored.

Bottom gated devices with very thin channel thickness (from few monolayer to  $\sim 100$  nm) are called thin film transistor (TFT). The contact are usually made of metals, but in general can also be obtained from well-conductive polymer as it is the case for the so called all-plastic (flexible) electronics. There exists two different configurations. Bottom-contact TFTs are produced by first patterning the two metal contact on a thin insulating layer and by then depositing the semiconductive organic material in a last step of the fabrication process. The other possible configuration is the top-contact geometry, where the two metal contact are produced in the last fabrication step, usually by a shadow mask evaporation which permits to pattern the contact without damaging the semiconducting layer. The advantage of the bottom-contact FET is that the properties of the channel like e.g. the thickness or the composition can be easily changed on the same device and the resulting characteristics can be continuously monitored. This is particularly helpful for studying the early stages

## 6.1. THIN FILM TRANSISTOR: INTRODUCTION AND WORKING PRINCIPLE

---

of the channel formation (see Sec. 6.2) and the doping of the resulting TFT (Sec. 6.4). The disadvantage is in general a poorer contact between the metal pad and the semiconductor because of the different growth of the film on the metal and on the oxide (as already presented in Sec. 4.4). This issue is discussed in Sec. 4.4.3 and in Chap. 7.

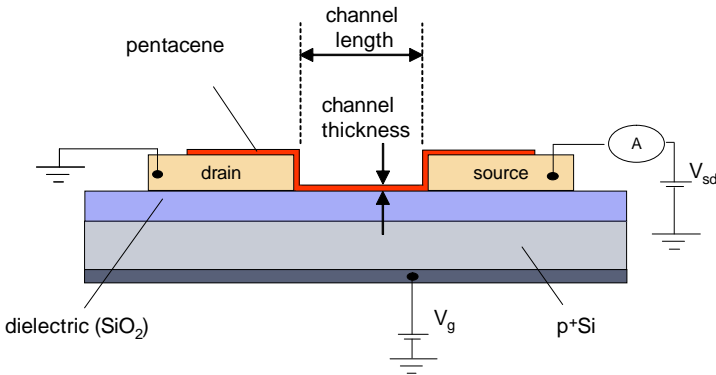


**Figure 6.1:** Schematic drawn of a bottom contact TFT. In these thesis, pentacene is used as organic semiconductor

### 6.1.2 Working principle

The advantage of using a FET for studying the transport properties of a semiconductor is that the conductivity of the channel, given by both the carrier density and the charge mobility, can be indepen-

## IN-SITU DOPING OF A FEW MONOLAYER PENTACENE THIN FILM

---

dently measured. The reason is that the gate bias voltage  $V_g$  linearly influence the charge carrier density in the channel, whereas the mobility is in a first assumption independent from the applied field and from the charge carrier density. To illustrate the working principle, the energetic band diagram of a p-type TFT is displayed in Fig. 6.2 with a cut in the perpendicular direction p-p' (Fig. 6.2(a)) show the allignment of the gate Fermi level  $E_F$ , the wide bandgap insulating oxide, the position of the high occupies molecular orbital (HOMO) and of the low unoccupies molecular orbital (LUMO). For a p-type semiconductor, the states responsible for the conduction (conduction states) lie close above the HOMO level. If no bias is applied to the gate (Fig. 6.2(a) and (b)), the Fermi level  $E_F$  lie somewhere between the HOMO and the LUMO of the organic semiconductor. In this situation the conductivity of the channel is very poor as the HOMO levels are not aligned to  $E_F$  as sketched in the horizontal cut h-h' presented in Fig. 6.2(b). By applying a negative bias between the gate and the two contact, an electric field is created in the channel. This shifts all the levels of the semiconductor toward positive values (Fig. 6.2(c). For large enough  $V_g$  conduction states (holes) start to be aligned with  $E_F$  (Fig. 6.2(d)) enabling the charge carriers to flow between source and drain. This voltage is the turn on voltage  $V_{on}$ . Around and below  $V_{on}$  there is the subthreshold regime, where charges are partially free to move. Only above the gate threshold voltage  $V_{g,th}$ , the number of induced charges contributing to the current increase proportionally with  $V_g$ .

### 6.1.3 Extrapolation of TFT mobility and charge carrier density from measurements

Because of charge neutrality, the charge carrier concentration  $p$  generated by  $V_g$  (above the gate threshold voltage  $V_{g,th}$ ) can be expressed

## 6.1. THIN FILM TRANSISTOR: INTRODUCTION AND WORKING PRINCIPLE

---

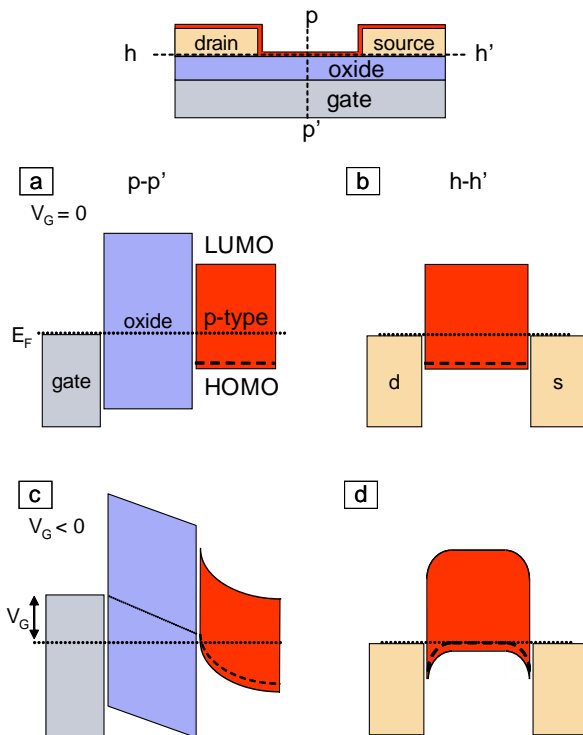


**Figure 6.2:** Working principle of a TFT. For simplicity band bending at the oxide-pentacene interface at  $V_G=0$  is neglected. In the experiments a  $p^+$ -Si substrate is used as the gate electrode.

## IN-SITU DOPING OF A FEW MONOLAYER PENTACENE THIN FILM

---

as

$$p(V_g) = \frac{C_{ox}}{et}(V_g - V_{g,th}) \quad (6.1)$$

where  $C_{ox}$  is the capacitance of the oxide per unit area,  $t$  the channel thickness and  $e$  the fundamental electric charge. A positive  $V_{g,th}$  indicate therefore the (zero gate) charge carrier density

$$p_0 = \frac{C_{ox}}{eT}V_{g,th} \quad (6.2)$$

The conductivity of the channel (channel length  $L$ , width  $W$  and thickness  $t$ ) can be probed by applying a bias  $V_{sd}$  between source of the drain and by measuring the resulting current  $I_{sd}$ . The conductivity at small  $V_{sd}$  (linear regime) is expressed as

$$G = \frac{I_{sd}}{V_{sd}} = \frac{W}{L}C_{ox}\mu_{TFET}(V_g - V_{g,th}) \quad (6.3)$$

where  $\mu_{TFET}$  is the mobility of the charge carriers. Therefore, measuring  $I_{sd}$  by varying  $V_g$  but at fixed  $V_{sd}$  enables to extrapolate  $\mu_{TFET}$  from the slope of the transconductance  $I_{sd}$  vs.  $V_g$ :

$$\mu_{TFET} = \frac{L}{WC_{ox}} \frac{1}{V_{sd}} \frac{\partial I_{sd}}{\partial V_g} \quad (6.4)$$

The above considerations are based on the assumption that the bulk resistance is much higher than the resistance of the metal-organic contact, so that  $V_{sd}$  mainly drops in the channel and not at the interfaces. In case of high  $\mu_{TFET}$ , large  $p$  or small  $L$ , the assumption fails. Only a portion of  $V_{sd}$  is really applied to the channel, the rest being applied to the interface. The potential drop at the interface  $V_c$  can be expressed as the contact resistance  $R_c = V_c/I_{sd}$ . In case of a linear relation between  $I_{sd}$  and  $V_c$ , the contact is designated as Ohmic. This can be verified by checking if  $I_{sd}$  depends linearly on

## 6.1. THIN FILM TRANSISTOR: INTRODUCTION AND WORKING PRINCIPLE

---

$V_{sd}$  for small  $V_{sd}$ , i.e. before starting the saturation regime. The effect of a large (ohmic and non-ohmic)  $R_c$  are noticed as non constant slope of the transfer characteristics, with in extreme case a saturation of  $I_{sd}$ . For practical application, high  $R_c$ 's are undesirable because of the decrease of  $I_{sd}$ , of the on/off ratio and the performance. It is therefore important to characterize the potential drop in the contact region.

### 6.1.4 Correction for contact resistance: transmission line method (TLM)

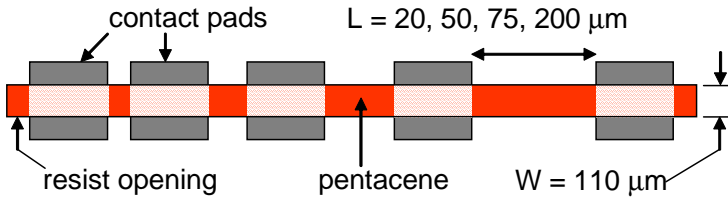


**Figure 6.3:** Schematic drawn of the devices used for the TLM: 4 devices with  $L=20-200 \mu\text{m}$  are obtained by depositing pentacene in the resist opening between the metal pads.

Several methods have been implemented for the measurements of  $R_c$ : 4-probes technique [80], kelvin probe [81] and transmission line method (TLM) [82]. In this dissertation, the TLM is used. It consists of measuring the total resistance  $R_{tot}$  of four TFTs with various channel length's  $L$  and fixed width  $W$  (Fig. 6.3). Here  $R_{tot}$

## IN-SITU DOPING OF A FEW MONOLAYER PENTACENE THIN FILM

---

is expressed as the sum of  $R_c$  and  $R_b$ , which depends on  $L$  and the sheet conductivity  $\sigma$ . By using the relation

$$R_{tot} = \frac{V_{sd}}{I_{sd}} = R_c + R_b = R_c + \frac{L}{W\sigma} = R_c + \frac{L}{WC_{ox}\mu_{cf}(V_g - V_{g,th,i})} \quad (6.5)$$

$R_c$  is evaluated by extrapolating to  $L=0$  the relation between  $R_{tot}$  and  $L$ :

$$R_c = R_{tot}(L=0) \quad (6.6)$$

while the contact free mobility  $\mu_{cf}$  is calculate by

$$\mu_{cf} = \frac{1}{WC_{ox}} \cdot \frac{\partial}{\partial V_g} \left( \frac{\partial R_{tot}}{\partial L} \right)^{-1} \quad (6.7)$$

An important assumption here is that the mobility is considered field independent, which should be considered for channel length dependent studies on the mobility at high  $V_{sd}$ . The  $V_{g,th,i}$  is the intrinsic gate threshold voltage, which differs from the  $V_{g,th}$  extrapolated from the transfer characteristics. It has been pointed out, that  $V_{g,th}$  is a fitting parameter without a real physical meaning [83]. Thus, the transfer characteristics of a TFT can be described at various temperatures without the need of  $V_{g,th}$ . However,  $V_{g,th}$  does reflect in a rough approximation the charge carrier density, following Eq. 6.2. Therefore, even if only indirectly, it is a useful fitting parameter. The difference between  $V_{g,th,i}$  and  $V_{g,th}$  is further discussed in Sec. 6.3.

### 6.1.5 Considerations on the models, peculiarities of organic semiconductors

Although the above described model will be exploited in some measurements in this thesis to estimate  $\mu_{TFT}$  and  $V_{g,th}$ , it is important to point out some limitations.

## 6.1. THIN FILM TRANSISTOR: INTRODUCTION AND WORKING PRINCIPLE

---

First of all, the onset of the conduction, i.e the region  $V_g > V_{g,th}$  also referred as subthreshold region is not considered. It is known from the literature and from experiments, that the onset is often not sharp and it is related to the effect of traps [84]. At higher negative  $V_g$ , these effects are less important as the traps get increasingly filled by charges. In some cases, it is not obvious where this transition region ends, and therefore the fit of the transfer characteristics is not unique. In this thesis, the fit is always performed from the  $V_g$  value corresponding to the highest slope. Second, the mobility is assumed to be field and charge carrier density independent in the model. The dependence on the charge carrier density is presented in Sec. 8.4. It will be shown, that at least for a doped pentacene TFT, the assumption of constant  $\mu$  is not justified. By adopting the fitting procedure described above, the evaluated mobility is approximately equal to the mobility at high charge carrier density. It is noted that the mobility can also be extrapolated from the saturation regime. However, e.g. in the in-situ monitoring of the TFT formation, a large  $V_{sd}$  would possibly influence the pentacene growth.

The last observation is on the applicability of the TLM. The method could be used with success for all doped TFTs, at all temperature and channel thickness conditions. There are some slight deviations from the foreseen linear dependence of  $R_{tot}$  at the higher  $L$  (Fig. 7.2), but these do not influence the extrapolated  $R_c$  or  $\mu_{cf}$  too much. However, for TFTs based on undoped pentacene, especially at low temperatures, the linear relation between  $R_{tot}$  and  $L$  is not fulfilled. Therefore the TLM can not be straightly applied in these cases. In general it is observed, that if the contact resistance is significant,  $R_{tot}$  decreases with increasing  $L$  from  $20\mu\text{m}$  to  $75\mu\text{m}$ . This behavior could be a consequence of contacts that differ in their resistance from device to device. This is plausible in the microscopic picture by considering that a small difference in the number or shape

## IN-SITU DOPING OF A FEW MONOLAYER PENTACENE THIN FILM

---

of the pentacene islands that cover the electrode edge can be responsible for a large change in  $R_c$ . On the the hand, the  $R_{tot}$  vs.  $L$  relation seems quite systematic, which would not be expected in these case. This behavior is not currently understood and the experimental data are simply not considered. It is noted that in the TLM, a field independent mobility is assumed.

### 6.2 In-situ control of TFT formation

#### 6.2.1 Sample preparation

Using the above described bottom-contact TFT, the properties of the devices at increasing channel thickness can be measured. The advantage is that sample to sample variations that depend on many experimental parameters are reduced. The samples are produced by patterning metal pads (gold or palladium) on a silicon wafer covered by 50 - 150 nm of SiO<sub>2</sub> grown by thermal dry oxidation. The separation between the metal pads, i.e. the channel length  $L$ , are between 20 $\mu$ m and 200 $\mu$ m. The active part of the device is defined by opening a 50-110 $\mu$ m wide window through a double layer resist over the contacting pads and over the channel. This approach ensures a low leakage current and a precise definition of the TFT geometry. The surface is cleaned by oxygen plasma for 30s. After cleaning, up to 4 devices on one chip are wire-bonded and loaded to the deposition chamber. The transfer takes approximately 15 min, therefore exposing the devices to ambient air. Longer exposure time is found to have a detrimental effect on the transport properties and leads in the extreme case to a unmeasurable small currents. Probably this is caused by the covering of the metal and the oxide by contaminants. The so minimized exposure to the air may also affect the performances, however since the extrapolated mobility is comparable to the values found in the literature, this effect is considered to be small. The chamber is pumped down for 12-24 h to a base pressure of  $\sim 10^{-8}$  mbar. The evaporation is performed as described in Sec. 4.3. Briefly, the pentacene is deposited at a rate of 0.3-0.6 ML/min up to a thickness of 6-7 ML. The devices are characterized in-situ at intermediate coverages. For some experiments aiming at the investigation of dopant molecules, a thin channel thickness of 1-3 ML is exposed to a subsequent evaporation of the dopant molecules from a second

## IN-SITU DOPING OF A FEW MONOLAYER PENTACENE THIN FILM

---

crucible. While reaching a stable evaporation rate of the dopant, the sample is hidden from direct exposure to the source. Therefore, a shorter stabilization time for the dopant ( $\sim 10$  min) compared to the stabilization time for the pentacene evaporator ( $\sim 1$  h) is necessary to avoid significant contaminations.

### 6.2.2 Measurements setup

The measurements are performed in-situ in the same vacuum chamber used for the deposition of pentacene. This chamber is equipped with a home made chip carrier holder fixed on a linear feedthrough. The electrical access to the samples is provided by a 7-pins electrical feedthrough connected by flexible cables to the chip carrier holder (Fig. 4.1). This enables to move the device in and out of the molecular beam without modification of the electrical connections. Moreover, the linear feedthrough can also be rotated along its longitudinal axis, which allows to deposit the molecules at any arbitrary angle. The electrical measurements are made using the same instruments used for the characterization of the nanorods device (Sec. 5.2). In addition, the gate voltage  $V_g$  is supplied by a Keithley 2400 which permits a maximal gate bias of  $\pm 20$  V and the measurement of the gate leakage current  $I_g$ . For all the presented results, only devices with  $I_g < 10$  pA have been considered.

### 6.2.3 TFT formation

By exploiting the deposition setup in combination with the in-situ characterization, the formation of the TFT can be monitored. For this purpose, a device with  $L=40 \mu\text{m}$ ,  $W=50 \mu\text{m}$  is exposed to the evaporation of pentacene molecules while applying  $V_{sd}=-1$  V,  $V_g=-5$  V and measuring  $I_{sd}$ . The results presented in Fig. 6.4 show that  $I_{sd}$  remains in the pA range up to a channel thickness  $t$  of 1.1 ML.

### 6.3. DETERMINATION OF THE MOBILITY AND THE THRESHOLD GATE VOLTAGE

---

At this stage, the evaporated pentacene forms separated monolayer islands. By increasing the coverage, the current suddenly increase to few nA, indicating the formation of a percolating network of conductive pentacene islands. Further increase of  $t$  up to 6 ML shows a second slower increase of  $I_{sd}$  to the 100 nA range. The change in the overall increase of  $I_{sd}$  at  $\sim 2$  ML seems to suggest a maximal mobility already achieved at 2 ML [6, 7]. The steps visible in the current intensity are caused by the TFT investigations that have been performed at intermediate channel thickness, which slightly modify the characteristics.

An example of the measured output characteristics ( $I_{sd}$  vs.  $V_{sd}$ ) of a device with  $t = 1.6$  ML ( $W=200 \mu\text{m}$ ,  $L=40 \mu\text{m}$ , oxide thickness  $t_{ox}=50 \text{ nm}$ ) is shown in Fig. 6.5(a). The current  $I_{sd}$  increases with negative gate voltages  $V_g$ , indicating a p-type behavior. Fig. 6.5(b) shows the transfer characteristics of the same device ( $I_{sd}$  vs.  $V_g$ ). From this second plot, the influence of the contact resistance  $R_c$  is identified as a decrease of the slope at higher currents. This is not obvious in the output characteristics, since  $I_{sd}$  around  $V_g=0$  is very linear, which is commonly taken as an indication of a good contact. The mobility  $\mu_{TFT}$  equal to  $0.02 \text{ cm}/(\text{Vs})$  is extracted by a linear fit of the curve at the maximal slope, while the gate threshold voltage  $V_{g,th}$  is the intercept of the linear fit with the abscissa.

### 6.3 Determination of the mobility and the threshold gate voltage

The investigation of the channel thickness necessary to reach a saturated value of the mobility is important to provide information on the extent of the accumulation layer. This has a precise physical meaning, as it shows how the motion of charges can be confined in

IN-SITU DOPING OF A FEW MONOLAYER  
PENTACENE THIN FILM

---

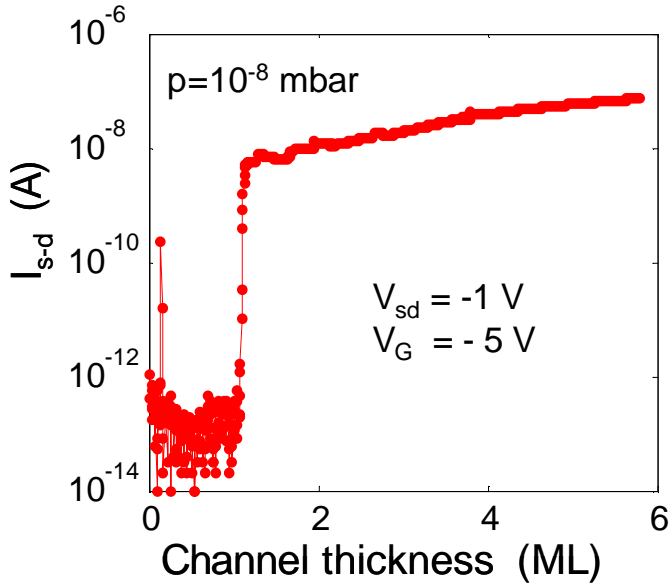


**Figure 6.4:**  $I_{sd}$  current measured at  $V_{sd}=-1$  V and  $V_g=-5$  V while evaporating pentacene over a TFT. At a critical channel thickness of 1-2 ML the current suddenly increases and saturates at 4-6 ML.

### 6.3. DETERMINATION OF THE MOBILITY AND THE THRESHOLD GATE VOLTAGE

---

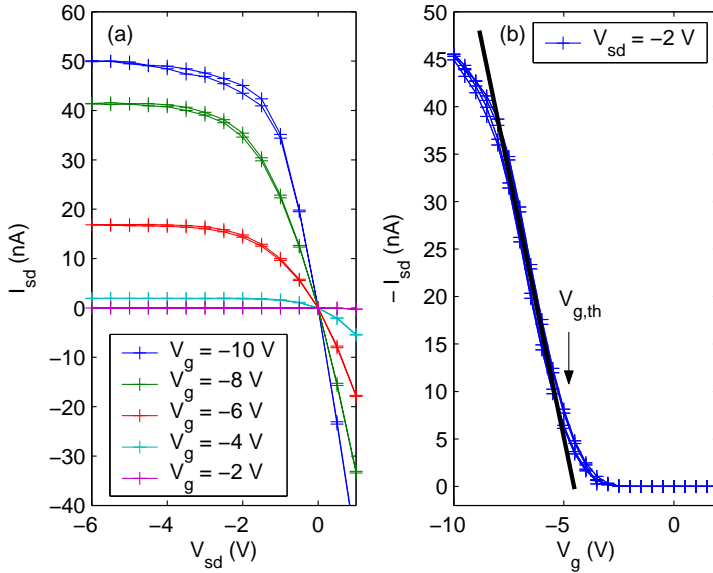


**Figure 6.5:** (a) Output characteristics of a pentacene TFT with a channel thickness of 1.6 ML measured in-situ:  $I_{sd}$  is plotted in function of  $V_{sd}$  (b) Transfer characteristics of the same device:  $I_{sd}$  is plotted in function of  $V_g$ . The effect of the contact resistance is noted by a decrease of the slope at high currents.

## IN-SITU DOPING OF A FEW MONOLAYER PENTACENE THIN FILM

---

organic semiconductors, which is important towards miniaturization and towards an understanding of the transport process.

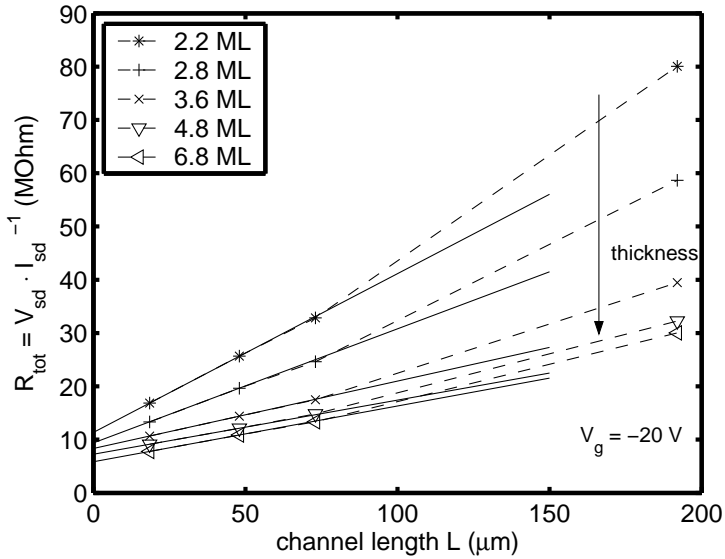
Using the in-situ measurements capability, the channel thickness  $t$  can be increased in several steps and the devices characterized after each additional deposition. The evaporation rate is 0.04 ML/min and the first 1.1 ML are deposited at an angle of  $+30^\circ$  and  $-30^\circ$  to the normal surface direction respectively, in order to well cover the side of the metallic pad. Additionally, devices with channel lengths from  $20\ \mu\text{m}$  to  $200\ \mu\text{m}$  are processed in parallel and characterized with the transmission line method (TLM, Sec. 6.1.3). This is important in order to extract mobility data free of parasitic resistance effects. For each device at various  $t$ ,  $I_{sd}$  is measured by setting  $V_{sd}=-0.1\ \text{V}$  and by scanning  $V_g$  between  $\pm 20\ \text{V}$  at a rate of 0.2-1 V/s. The mobility  $\mu_{TFT}$  and  $V_{g,th}$  are determined from the transfer characteristics as presented above.

Fig. 6.6 shows  $R_{tot} = V_{sd}/I_{sd}$  of pentacene TFTs with channel width  $W = 110\ \mu\text{m}$  at different  $t$  and at  $V_g = -20\ \text{V}$ . It is noted that  $R_{tot}$  increases proportionally to  $L$  below  $80\ \mu\text{m}$ . Therefore, using the data in this  $L$  range, the contact free mobility  $\mu_{cf}$  is calculated from Eq. 6.7. The influence of the channel thickness on the extracted  $\mu_{cf}$  is presented in Fig. 6.7. In comparison, the mobilities  $\mu_{TFT}$  from the transfer characteristics of the TFTs with the different channel lengths  $L$  are also plotted.

The results show that the contact free mobility  $\mu_{cf}$  saturates at  $t \approx 3-4\ \text{ML}$ . The measured  $\mu_{TFT}$  depends on  $L$ : higher values of  $\mu_{TFT}$  are recorded for devices with long channel length  $L$ . Because the devices are processed in parallel, this excludes strong device-to-device variation and suggests an important contribution of the contacts on the measured mobility. In fact, the contact free mobility  $\mu_{cf}$  is  $\sim 40\%$  higher than  $\mu_{TFT}$  for the longest channel and a up to a factor 4 for the shortest one. This implies that  $\mu_{TFT}$  is strongly in-

### 6.3. DETERMINATION OF THE MOBILITY AND THE THRESHOLD GATE VOLTAGE

---



**Figure 6.6:** Total resistance  $R_{tot}$  measured for undoped pentacene TFTs with various channel length  $L$  and channel thickness.

IN-SITU DOPING OF A FEW MONOLAYER  
PENTACENE THIN FILM

---

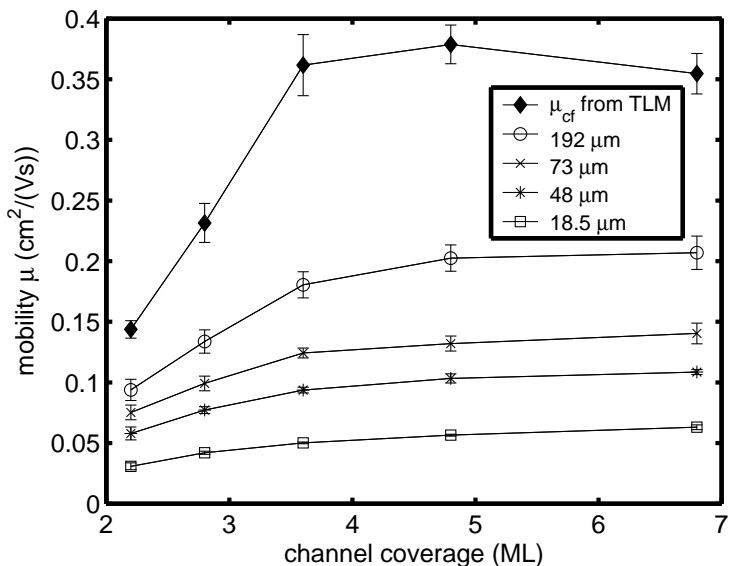


**Figure 6.7:** Contact free mobility  $\mu_{cf}$  of pentacene TFTs at various channel thickness. In comparison, the mobility  $\mu_{TFT}$  extracted from the slopes of the transfer characteristics of TFTs with different  $L$  is systematically lower. The difference is assigned to the contact resistance that is neglected in the extraction of  $\mu_{TFT}$ . Error bars indicate the difference between the up and down scan of  $V_g$  in the measured data

### 6.3. DETERMINATION OF THE MOBILITY AND THE THRESHOLD GATE VOLTAGE

---

fluenced by the contact resistance and is underestimated with respect to the real  $\mu_{cf}$  governing the charge transport in the thin film.

The measured  $\mu_{cf}$  value are in agreement with the values found in the literature for polycrystalline pentacene, which range from 0.5 to 0.8 cm<sup>2</sup>/(Vs) (measured with TLM, [69]). For single crystal pentacene measured with a 4-point method and an air-gap field-effect technique, the mobility reach 20 cm<sup>2</sup>/(Vs) [80].

By comparing the transfer characteristics of TFTs with different channel lengths  $L$ , it is noted that not only  $\mu_{TFT}$ , but also  $V_{g,th}$  depends on both  $t$  and  $L$ . Fig. 6.8(a) shows the conductivity scaled by  $L/W$  of the same set of measurements used for the extraction of the mobility data. The black lines denote the linear fit. It is recognizable, that  $V_{g,th}$  increases with increasing  $t$  and decreasing  $L$ . The maximal shift between TFT with the same coverage  $t$  is as large as 4.7 V, while by comparing the shortest and the longest  $L$ , the maximal shift is 7.2 V. The dependence of  $t$  can be understood as an increase of  $p$  caused by the contribution of the grain boundaries which density per square area increasing with  $t$ . The dependence on  $L$  is more puzzling. In the saturation regime (i.e. in case of  $V_{sd} \gg V_g$ ) it is attributed to a drain lowering of the Schottky barrier [85], where the source-drain field depends on  $L$  for fixed  $V_{sd}$  and on  $V_g$ . This can not be the case in the linear regime, where the source-drain field is much lower than the gate field. A plausible explanation is that  $V_{g,th}$  suffers from  $R_c$  since it is extrapolated from the transfer characteristics that are clearly influenced by the contact properties. Fig. 6.8(b) shows the conductivity, scaled by  $1/W$  obtained by the slope of the relation  $R_{tot}$  vs.  $L$  at  $V_g$  from 0 to -10 V (Eq. 6.5). The intrinsic  $V_{g,th,i}$ , identified by the intercept of the linear fit with the abscissa, is about 10 V and varies only by 2.4 V for different channel thickness. This value is close to  $V_{g,th}$  for the longest  $L$  (Fig. 6.8(a)), confirming the importance of the contact resistance on the precise

## IN-SITU DOPING OF A FEW MONOLAYER PENTACENE THIN FILM

---

determination of the characteristics of short channel TFTs.

The good quality of the obtained device presented above allows the use of TFT with  $\sim 2$  ML channel thickness. These devices are an interesting new tool to study the interaction effects of dopant molecules directly deposited on top of the channel in a sub-ML coverage. The same devices are also well suited for the investigation of the effect of pentacene TFT exposed to the air. These are the topics of the next two sections.

### 6.3. DETERMINATION OF THE MOBILITY AND THE THRESHOLD GATE VOLTAGE

---

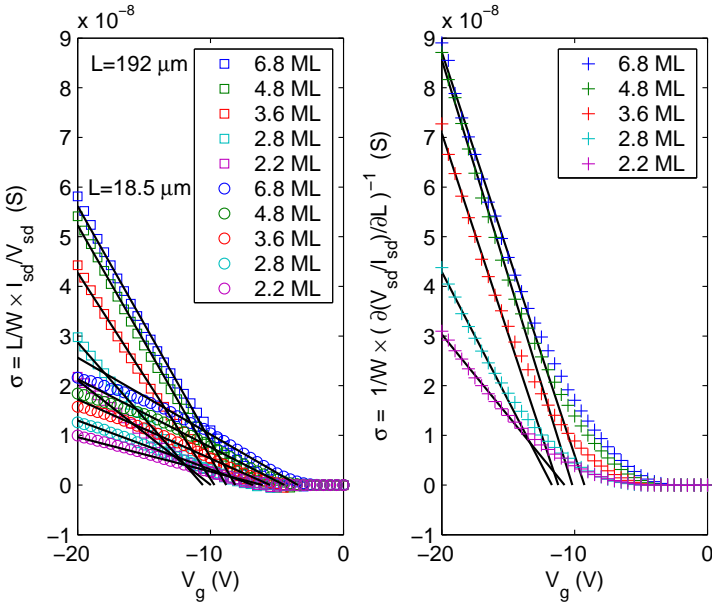


**Figure 6.8:** (a) Conductance obtained from the transfer characteristics of a TFT with  $L=18.5 \mu\text{m}$  and  $L=192 \mu\text{m}$  at various channel thickness. From the linear fit,  $V_{g,th}$  varies between -3.4 and -10.5 V. (b) Conductance obtained from the TLM. An intrinsic  $V_{g,th,i}$  of  $10 \pm 1.2$  V characterize all the TFTs.

## 6.4 Effect of guest dopant molecules

### 6.4.1 Control of threshold gate voltage by in-situ doping

TFT devices with a pentacene thickness of 1-3 ML are used to investigate the effect of an evaporation of very low dose of a second dopant molecule on top of the existing pentacene channel. The investigated organic molecules are tetrafluoro-tetracyanoquinodimethane ( $F_4TCNQ$ , Fluka), manganese(III)-tetraphenylporphyrin chloride ( $MnTPPCL$ ) (Aldrich) and Fullerene ( $C_{60}$ , Aldrich) used as received. Since a very low dopant coverage already modifies the transfer characteristics of the TFTs, a low evaporation rate of 0.02 ML/min is necessary. This should also minimize the damages to the existing pentacene layer, which could lead to a decrease of the mobility because of structural defects induced by the deposition. All measurements are performed in-situ and in the dark.

Figure 6.9(a) shows the transfer characteristics of a pentacene TFT with  $L = 40 \mu m$ ,  $W = 50 \mu m$  and channel thickness of  $\sim 2$  ML exposed to a subsequent evaporation of dopant molecules. The transfer characteristics is measured by applying a fixed drain-source bias ( $V_{sd} = -1, V$  for the  $MnTPPCL$  and  $V_{sd} = -0.1, V$  for  $F_4TCNQ$ ). The effect of the dopant molecules is characterized in terms of the shift of the  $V_{g,th}$  and of the change of the mobility  $\mu_{TFT}$  extracted from the transfer characteristics (Sec. 6.1.3). It is recognized, that the  $MnTPPCL$  molecules induce a decrease of  $V_{g,th}$  and of the mobility  $\mu_{TFT}$ . This is assigned to a n-type doping. It should be noted, that the effect is already noticeable at 0.2 mol% of , which represents a molecular surface density at the of  $4.7 \times 10^{11}$ . An opposite behavior is observed for the  $F_4TCNQ$  molecule (Fig. 6.9(b)). The deposition shifts  $V_{g,th}$  towards positive values, which indicates an increase of the charge carrier density  $p_0$  (Eq. 6.2). This observation is discussed in

## 6.4. EFFECT OF GUEST DOPANT MOLECULES

---

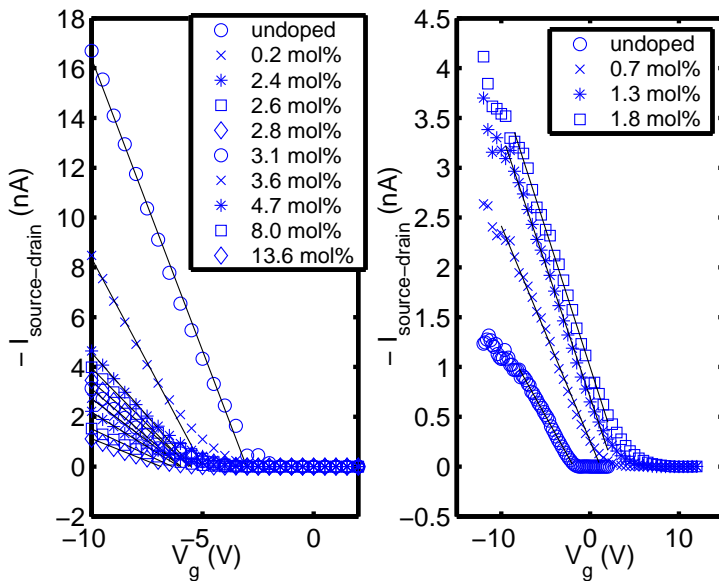


**Figure 6.9:** Comparison of the effect of guest dopant molecules on the transconductance. (a) Doped with MnTTPCl. (b) Doped with F4TCNQ.

## IN-SITU DOPING OF A FEW MONOLAYER PENTACENE THIN FILM

---

the next section. The mobility  $\mu_{TFT}$  also appear to increase, but this result has to be carefully reflected. In fact, the detailed investigations presented in Chap. 7 suggest that this effect is related to a decrease of the contact resistance. The last observation is on the influence of the adsorbed  $C_{60}$ , which have been evaporated on top of the pentacene channel without modification of the electrical properties being observed.

Fig. 6.10 summarizes the shift of  $V_{g,th}$  for the investigated molecules. The minute variation of  $V_{g,th}$  for the three undoped devices is a consequence of run-to-run variations and possible contaminations of the device during the stabilization time necessary to equilibrate the heated dopant crucible in order to reach a stable evaporation rate.

As stated above, the addition of  $F_4TCNQ$  molecules promotes a charge transfer (CT) process between the pentacene and the dopant molecules. This is tentatively explained by considering the ionization energy (IE = difference between the vacuum level and the HOMO) and the electron affinity (EA = difference between the vacuum level and the LUMO) of the two molecules. A summary of the electronic levels of the investigated molecules is presented in Fig. 6.11. From UPS-IPES experiments [36], the HOMO level of pentacene is observed at -5.0 eV and the LUMO of the highly electronegative  $F_4TCNQ$  is observed at -5.2 eV. A transfer of an electron between the HOMO level of pentacene to the LUMO of  $F_4TCNQ$  (-5.2 eV) seems therefore energetically favorable. This process would create a hole in the HOMO of the pentacene and lead to an increase of  $p$ . This is consistent with the transfer characteristics being experimentally measured as shifted to more positive gate values.

The situation for the  $MnTPPCl$  is more difficult to interpret, since the fact that the HOMO at -8 eV and the LUMO at -2 eV does not indicate a possible transfer of charges. A similar consideration on the electronic level can be made for  $C_{60}$ , where the HOMO is

## 6.4. EFFECT OF GUEST DOPANT MOLECULES

---

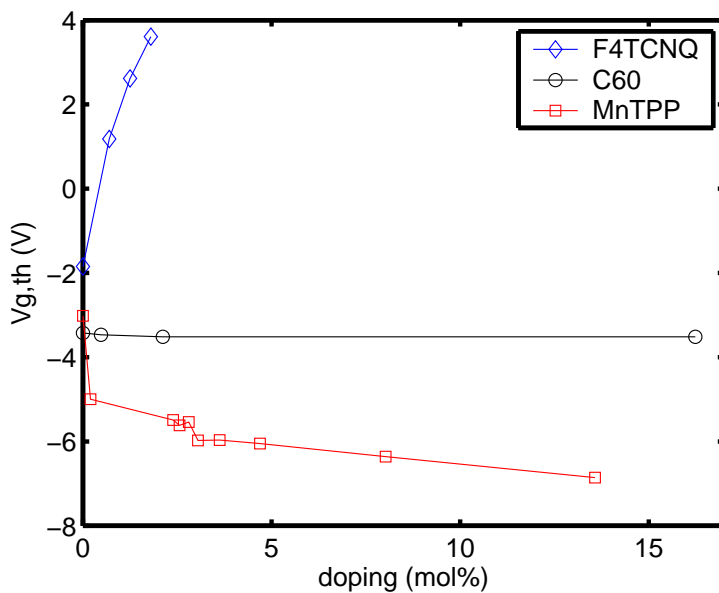


**Figure 6.10:** Dependence of the threshold gate voltage on the amount of additional dopant molecules.

## IN-SITU DOPING OF A FEW MONOLAYER PENTACENE THIN FILM

---

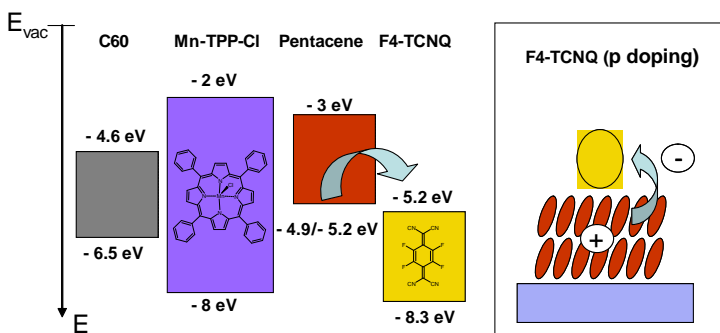


**Figure 6.11:** Summary of the electronic level of the investigated molecules. A charge transfer doping process for pentacene seems energetically favorable only with F<sub>4</sub>TCNQ

## 6.4. EFFECT OF GUEST DOPANT MOLECULES

---

located at -6.5 eV and the LUMO at -4.6 eV [86]. Indeed, no indication of electronic interactions is observed between  $C_{60}$  and pentacene. The shift of  $V_{g,th}$  in the case of MnTPPCl can be explained by the existence of energy levels in the bandgap, given for example by impurities or by a partial thermal decomposition due to the evaporation process. The difference between MnTPPCl and  $C_{60}$ , besides lower thermal stability of MnTPPCl, is the existence of an electric dipole and a magnetic moment given by the unpaired spin of the partially oxidized Mn atom. An exciting explanation of the shift of  $V_{g,th}$  and the decrease of  $\mu_{TFT}$  upon addition of MnTPPCl to pentacene could therefore be related to the electronic interaction of those dipoles with the charges in the conducting layer. More experiments would be necessary in order to gain insight in this possible phenomena. However, because of the improved transport properties of  $F_4TCNQ$  doped pentacene, the further investigations in the dissertation concern this latter doping process.

### 6.4.2 $F_4TCNQ$ doping : effect on the carrier concentration

The addition of  $F_4TCNQ$  dopant molecules on top of a few ML TFT is now studied in detail: starting with TFTs devices with  $L=20 \mu m$  and  $50 \mu m$  and  $W=110 \mu m$ , the dopant molecules are added in several subsequent steps. The evaporation and the characterization are performed similar to the case described for the devices presented in Sec. 6.4 except that a  $V_{sd}=-0.1 V$  is applied for the measurement of  $I_{sd}$ .

Fig. 6.12(a) shows the change of the transfer characteristics after the addition of the surface dopant, performed in several steps. The first observation, already noticed in Fig. 6.9(b), is that the current strongly increases and  $V_{g,th}$  moves toward positive voltages. The

## IN-SITU DOPING OF A FEW MONOLAYER PENTACENE THIN FILM

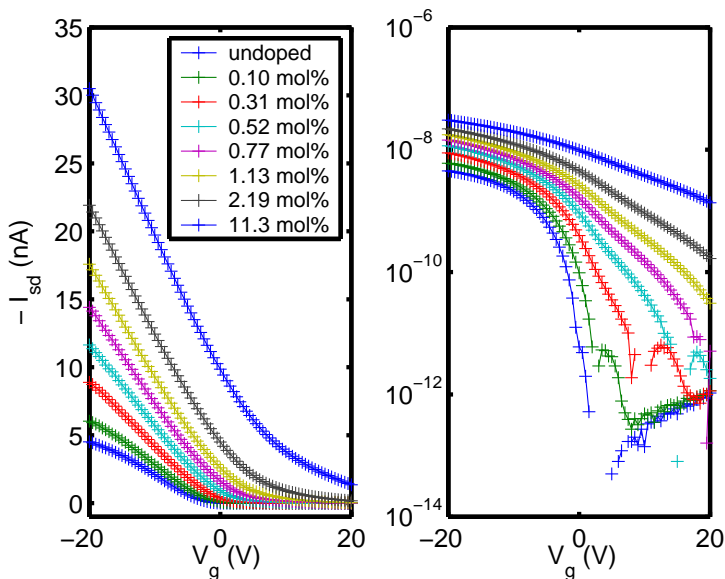


**Figure 6.12:** Evolution of the transfer characteristics of a TFT device with  $L=50\ \mu\text{m}$  upon addition of  $F_4TCNQ$  on top of a 1.7 ML pentacene channel. (a) linear and (b) logarithmic plot of the transfer characteristics obtained by applying  $V_{sd}=-0.1\ \text{V}$ .

## 6.4. EFFECT OF GUEST DOPANT MOLECULES

---

second observation is the decrease of the on/off ratio, i.e. of the ratio between the maximal current at the  $V_g=-20$  and the minimal current at positive  $V_g$ . The undoped device shows an on/off ratio of  $4 \times 10^4$ , while it decrease to 15 for the devices doped with 11.3 mol%. The decrease of the on/off ratio is ascribed to a strong increase of the charge carrier density, which can not be electrostatically controlled by the gate voltage. This observation is in agreement with [59], but clearly limits the maximum amount of doping for obtaining a device with good dynamic range.

To quantify the number of doping induced charge carriers, the change in the gate threshold voltage  $V_{g,th}$  is evaluated for a device with  $L=20 \mu\text{m}$  and  $L=50 \mu\text{m}$ . In Fig. 6.13 the shift  $\Delta V_{g,th}$  relative to the  $V_{g,th}$  of the undoped devices is plotted as a function of the amount of additional dopant.

The dopant ratio  $c$  is expressed in mol% relative to the total amount of deposited pentacene (1.7 ML). The induced charge carriers concentration per unit area  $p$  is estimated from  $p = C_{ox}\Delta V_{th}/e$ , where  $C_{ox}$  is the oxide capacitance ( $2.4 \times 10^{-8} \text{ F/cm}^2$  given by the 150 nm  $\text{SiO}_2$  used as gate dielectric). Below  $\sim 1$  mol%,  $p$  increase linearly with  $c$ . The activation ratio  $\eta$  indicating the charges induced by a dopant molecules can therefore be calculated from relation between  $p$  and  $c$ . It is found that for  $L=20 \mu\text{m}$ ,  $\eta$  is equal to 1, while it decreases to 0.5 for  $L=50 \mu\text{m}$ . This dependence from  $L$  is not well understood, but is probably related to the  $V_{g,th}$  dependence on  $L$  caused by the the extrapolation of  $V_{g,th}$  from the transfer characteristics without correcting for the contact resistance (see Sec 6.1.4). Nevertheless, this provides an estimation of the number of charges produced by the charge transfer process between pentacene and  $\text{F}_4\text{TCNQ}$ . Since a long channel TFT is less sensitive to the contact resistance,  $\eta$  is estimated to be in the range of 0.1, which would imply that in average 1 over 10  $\text{F}_4\text{TCNQ}$  molecule provides a hole to

## IN-SITU DOPING OF A FEW MONOLAYER PENTACENE THIN FILM

---

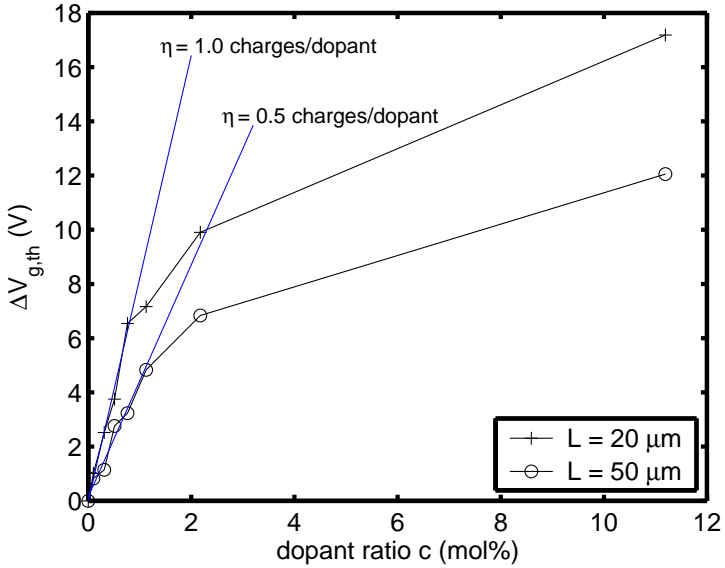


**Figure 6.13:** Shift of the gate threshold voltage by addition of F4TCNQ for a FTF with channel length  $20 \mu\text{m}$  and  $50 \mu\text{m}$ . The activation ratio  $\eta$  represents the induced charges pro dopant molecule.

## 6.5. INFLUENCE OF AIR EXPOSURE ON THE THRESHOLD GATE VOLTAGE

---

the conductive pentacene channel. It is worth to note that the deviation from the linear relationship appear at  $\sim 1$  mol%. Assuming that the deviation occurs when the influence area of the dopant molecules start to overlapp, it can be concluded that the radius of influence of a dopant molecule is equal to the average distance between the dopant at  $\sim 1$  mol%, which corresponds to  $\sim 5$  nm. This is a rough approximation that assume also that the dopants are well distributed on top of a perfect pentacene layer, but provides an estimation of the extension of the coulomb potential of the ionized dopant in a 2-dimensional geometry.

## 6.5 Influence of air exposure on the threshold gate voltage

In Sec. 5.2 it was shown that the conductance of pentacene nanojunctions increases upon air exposure. In order to quantify this unintentional effect, TFTs with 2 ML pentacene channel ( $L=40 \mu\text{m}$ ,  $W=50 \mu\text{m}$  for the TFT measured in vacuum,  $W=500 \mu\text{m}$  for the TFT measured in air) measured in-situ in the dark and in air with light. For these experiments, the characterization is performed by scanning  $V_{sd}$  between +1 V and -5 V at each  $V_g$ . It is confirmed for both TFTs that the  $I_{sd}$  is linear at small  $V_{sd}$ , which permits to calculate the conductance by the slope  $\partial I_{sd}/\partial V_{sd}$ . The conductance normalized by the device geometry is plotted in Fig. 6.14. The gate threshold  $V_{g,th}$  moves from -4 V for the TFT measured in vacuum to +4.3 V for the TFT measured in air. This indicate an increase of the charge carrier concentration  $p_0$  to  $3.3 \times 10^{17} \text{ c/cm}^3$  (Eq. 6.2) and a change of the TFT from a normally-off ( $I_{sd}=0$  for  $V_g=0$ ) to a normally-on ( $I_{sd} \neq 0$  for  $V_g=0$ ). The decrease of the slope upon air exposure is related to a decrease of the mobility  $\mu$ . The measurements in air are

## IN-SITU DOPING OF A FEW MONOLAYER PENTACENE THIN FILM

---

performed after  $\sim 15$  min of exposure to the air. With much longer exposure time,  $\mu$  decreases further and finally the current become so small that it is not possible to measure the TFT properties anymore. It is concluded, that exposure to the air and light increases  $p$  but decreases  $\mu$ . A proper encapsulation would be required in order to stably operate the TFT in air.

## 6.5. INFLUENCE OF AIR EXPOSURE ON THE THRESHOLD GATE VOLTAGE

---

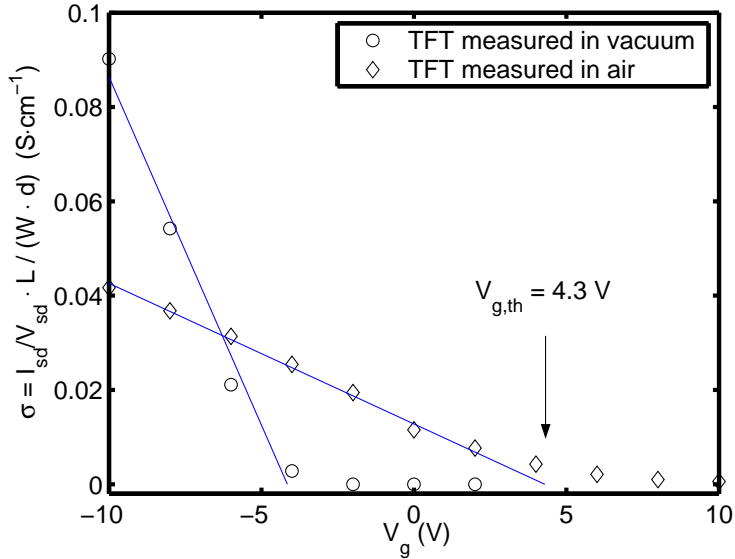


**Figure 6.14:** Channel conductivity  $\sigma$  as a function of  $V_g$  of two TFTs measured in vacuum and in air. The TFT measured in air shows a positive  $V_{g,th}$ , which indicates an increase of  $p$  upon air exposure.



# Chapter 7

## Coevaporation of F<sub>4</sub>TCNQ and pentacene

As recognized in Sec. 6.3, the contact resistance  $R_c$  of few ML TFT plays an increasing role, especially as the size of the devices is reduced below the  $10\ \mu\text{m}$  range. Towards the miniaturization of organic electronic devices and the improvement of their performances, it is therefore important to decrease  $R_c$ . In this section, the doping schema for the reduction of  $R_c$  is investigated.

### 7.1 Reduction of the contact resistance

Following the procedure presented in Sec. 6.2.1, doped pentacene TFTs are in-situ prepared and characterized. In order to keep the

## COEVAPORATION OF F<sub>4</sub>TCNQ AND PENTACENE

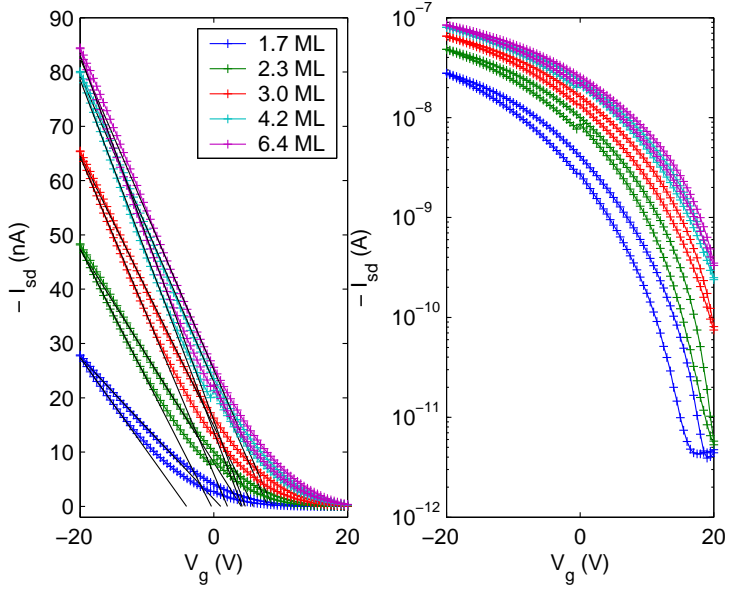


**Figure 7.1:** Transfer characteristics for a  $(0.7 \pm 0.02)\%$  F<sub>4</sub>TCNQ doped pentacene TFT with  $L=18 \mu\text{m}$  at various channel thicknesses.

## 7.1. REDUCTION OF THE CONTACT RESISTANCE

---

on/off ratio reasonably high, a low doping ratio of  $(0.7 \pm 0.02)\%$  is used. This is achieved by evaporating a mixture of  $F_4TCNQ$  and pentacene. The doping concentration  $c$  is estimated from the relation between  $\Delta V_{g,th}$  and  $c$  presented in the previous Chapter (Fig. 6.13) by comparing devices with the same  $L$ . From the transfer characteristics (Fig. 7.1) it is found that the on/of ratio is 250 for the TFT with  $L=18\ \mu\text{m}$  and the thickest channel coverage, but increases to  $5 \times 10^3$  at the thinnest coverage. The TFT with larger  $L$  have on/off ratios in between these values. Using these data, the same analysis based on the transmission line method (TLM) presented in Sec. 6.1.3 is carried out. The results are presented in Fig. 7.2.

Comparing with the undoped TFT (Fig. 6.6), it is found that the linear relation between  $R_{tot}$  and  $L$  is improved up to the longest channel devices. This is consistent to the model by Horowitz, where the mobility in polycrystalline organic TFT is limited by the grain boundaries, of which influence can be reduced by doping [87]. Fig. 7.3 shows the extrapolated  $R_c$  for both an undoped and the doped TFTs.  $R_c$  includes the contribution of both source and drain contact. The error bars indicate the difference of  $R_c$  due to the hysteresis of  $I_{sd}$  between up and down sweeps of  $V_g$ . The hysteresis is not a consequence of the setup capacitance: an example of small hysteresis can be seen in Fig. 6.5. For clarity, the up sweep has been omitted so far.

For both undoped and doped TFTs,  $R_c$  decreases with increasing channel thickness  $T$ . The decrease is attributed to the increased uniformity of the pentacene coverage at the edge of electrode contacts. This is concluded from SEM observations of the devices at different channel thickness prepared using the same conditions. For the undoped TFTs,  $R_c$  reaches a minimum value of  $7\ \text{M}\Omega$  at the thickest  $T=6.4\ \text{ML}$  with  $V_g=-20\ \text{V}$ . The  $R_c$  is 8 times higher compared to the reported values [82, 88]. This is ascribed to the small deposited pentacene thickness: in fact only the electrode edge is completely covered

## COEVAPORATION OF F<sub>4</sub>TCNQ AND PENTACENE

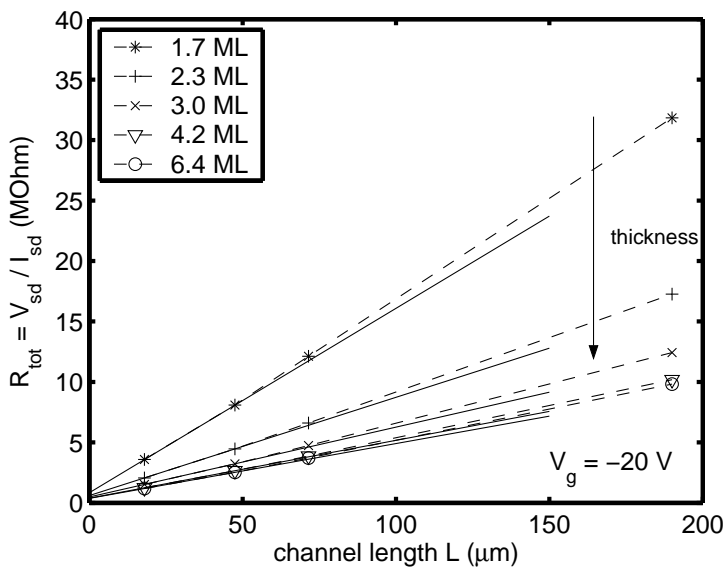


**Figure 7.2:** Total resistance  $R_{tot}$  measured for F<sub>4</sub>TCNQ doped pentacene TFTs with various channel lengths  $L$  and channel thicknesses.

## 7.1. REDUCTION OF THE CONTACT RESISTANCE

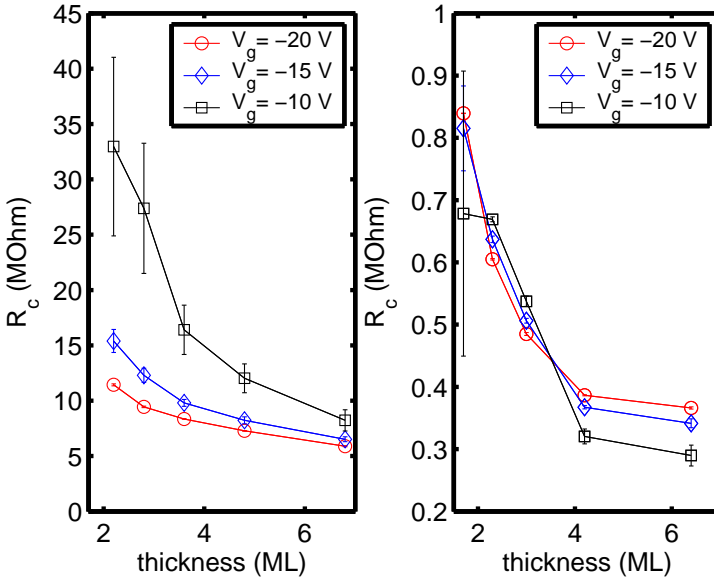


**Figure 7.3:** Extrapolated  $R_c$  using the TLM method as a function of the channel thickness at various  $V_g$  for (a) undoped and (b) doped TFTs.

## COEVAPORATION OF F<sub>4</sub>TCNQ AND PENTACENE

---

by pentacene while the surface of the electrode does not contribute to the injection of the current in the channel, decreasing therefore the effective area. Moreover, the contact resistance may also depend on the thickness of the organic semiconductor above the metal surface. For the doped TFTs,  $R_c$  is  $\sim 0.35$  MOhm, which is a factor 20 smaller than that of undoped TFTs. The  $R_c$  of the undoped TFT is about 80% of the total resistance for a channel length of  $20 \mu\text{m}$ . For the doped TFT, the  $R_c/R_{tot}$  decrease to 30%. This indicates that the resistance of the channel is strongly reduced because of the additional charge carriers induced by the doping process, but the resistance of the contact region is even more influenced. The observation underlines the importance of  $R_c$  on the organic TFT performance.

For the undoped TFTs and at fixed  $T$ ,  $R_c$  decreases when a more negative  $V_g$  is applied. This indicates that the gate electric field is essential for the efficient injection of charges to the TFT channel. This can be compared to the Schottky barrier transistor in carbon nanotube [89]. The barrier height is determined by the band alignment and the gate induced carrier concentration [90]. This enhances the thermionic emission over the barrier [91]. At the same time, the higher carrier concentration decreases the depletion width and enhances the (thermal assisted) tunneling through the barrier [92]. Both processes lead to an enhancement of the carrier injection by  $V_g$ .

The situation is reversed for the doped TFT. First, the influence of  $V_g$  is less pronounced. This is ascribed to the fact that the potential profile is here mostly determined by the ionized dopants [93]. Second, a detailed inspection of the data indicates a slight increase of  $R_c$  for  $V_g$  below  $-10$  V. It is noted that the increase of negative  $V_g$  leads to the downward shift of the density-of-state (DOS) of pentacene channel relative to the Fermi energy of the electrode while increasing the DOS filling by holes. Therefore, the decrease of  $R_c$  can be ascribed to the decrease of DOS with  $V_g$  e.g. by saturating the states created by

## 7.2. COMPARISON BETWEEN THE MOBILITY OF UNDOPED AND DOPED TFT

---

the ionized dopants [5]. This reduces the thermal assisted tunneling through the barrier by decreasing the available final states [13]. On the other hand, the increase of the hole concentration in the channel can partially screen the impurity potential that counteracts the barrier lowering effect. Consequently the width of the interface barrier is increased. However, the screening property of the holes limited by the hopping-like conduction in organic semiconductors has not been clarified yet.

## 7.2 Comparison between the mobility of undoped and doped TFT

The same data analyzed above also provides evidence that the mobility is hardly affected by the ionized dopants. Fig 7.4 shows a comparison between the contact free mobility  $\mu_{cf}$  measured using the TLM (Eq. 6.7) for the undoped and doped TFTs. Although  $\mu_{cf}$  of the doped TFT is slightly higher for a thickness smaller than 3 ML, it reaches a similar saturation value of  $(0.35 \pm 0.05) \text{ cm}^2/(\text{Vs})$  for increasing coverage. The small difference in the early stage of the channel formation is explained by the importance of the grain boundaries at this stage. It was pointed out by Horowitz et. al [50], that back-to-back Schottky barriers form at the intergrain regions. The barrier width depends on the amount of defect states at the grain boundaries. It is therefore plausible, that additional charges originating from the doping process decreases these barriers and therefore enhances the measured mobility. However, from the data presented here it can be concluded that this does not lead to a drastic change in the channel mobility at high gate voltage.

## COEVAPORATION OF F<sub>4</sub>TCNQ AND PENTACENE

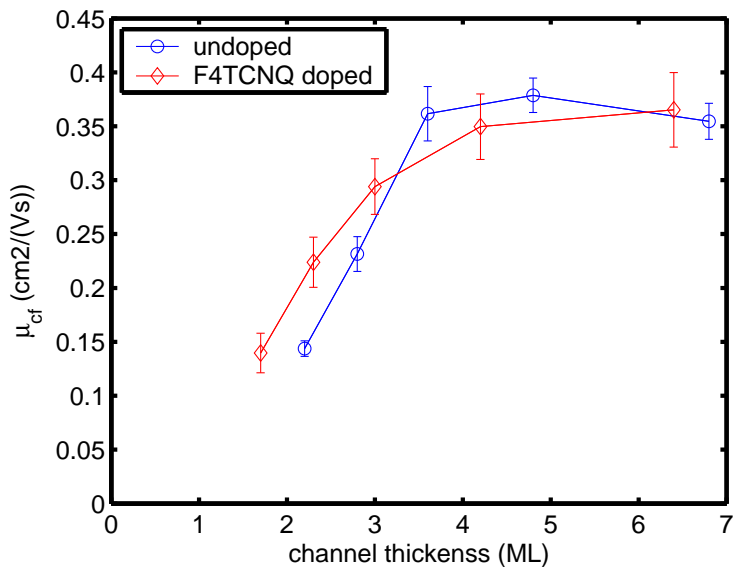


**Figure 7.4:** Contact free mobility for undoped and F<sub>4</sub>TCNQ doped pentacene. The mobility is similar in both cases and is saturated at 3-4 ML. This shows the minimal influence of the dopant molecules on the hopping/scattering of the charges.

# Chapter 8

## Thermally activated transport in pentacene

In this section, the results of temperature dependent characterizations of the TFTs are presented. For these measurements, the devices have to be transferred to the same cryostat which has also been used for the characterization of the nanojunction devices (Sec.5.3). The exposure time to ambient air is kept to the minimal, typically  $\sim 5$  min. All the TFTs presented in this chapter have a channel length between  $20\ \mu\text{m}$  and  $200\ \mu\text{m}$ , a channel width  $W$  of  $110\ \mu\text{m}$ , a gate oxide thickness of  $150\ \text{nm}$  and a channel thickness of  $6\text{-}7\ \text{ML}$ . In case of doped TFTs, the TLM can be applied over the whole range of investigated temperatures. This allows to extrapolate the contact resistance  $R_c$  and the contact free mobility  $\mu_{cf}$ . These data are compared to the

## THERMALLY ACTIVATED TRANSPORT IN PENTACENE

---

mobility extracted from the transfer characteristics  $\mu_{TFT}$  of undoped and doped TFTs. In the last part of the chapter, the dopant induced modification on the density of states (DOS) is presented.

### 8.1 Temperature dependence of the mobility

Fig. 8.1 and Fig. 8.2 show some examples of the acquired transfer characteristics at different temperatures. It is noted that because of the short exposure to the air, the characteristics are slightly different from these which have been acquired in-situ. Most evident is the shift of the transfer characteristics of the doped TFT towards negative voltages, which is assigned to a partial de-doping. However, the conclusions presented in this chapter are based on the difference between undoped and doped TFT and are therefore not fundamentally affected.

From these data, the TLM is applied and the extracted contact free mobility  $\mu_{cf}$  at gate voltage  $V_g$  between -10 V and -18 V is presented in Fig. 8.3. An almost linear relation between  $\log(\mu_{cf})$  and  $1/T$  is found with a corresponding  $E_a$  of approximately 95 meV for  $V_g = -10$  V, and slightly lower for more negative  $V_g$ . By carefully looking at the data, it is found that  $E_a$  is higher at lower  $T$  and no sign of temperature independent mobility is found. This reflects the hopping character of the charge transport in these polycrystalline 6-7 ML thin film.

For comparison, an Arrhenius plot of the mobility  $\mu_{TFT}$  calculated from the fit of the linear part of the transfer characteristics presented above is presented in Fig. 8.4. As stated in Chap. 7, the doping process drastically decreases the contact resistance  $R_c$ . The calculated mobility should be therefore less affected by  $R_c$  and  $L$ .

## 8.1. TEMPERATURE DEPENDENCE OF THE MOBILITY

---

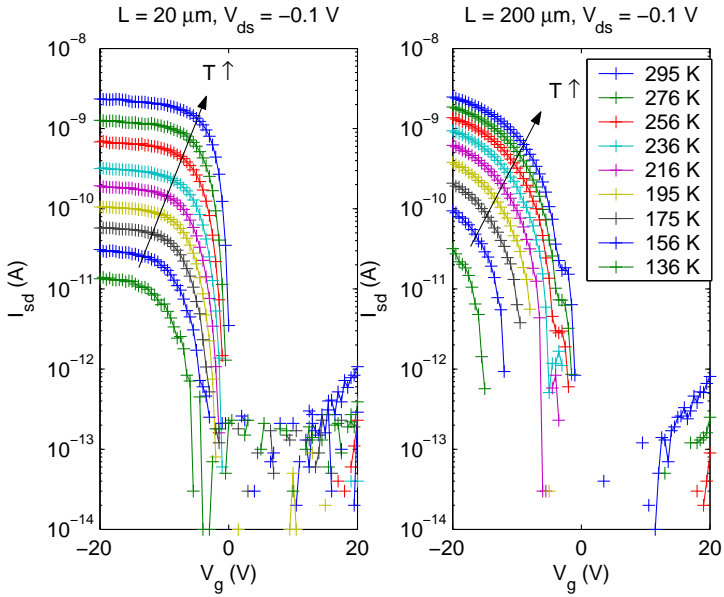


**Figure 8.1:** Transfer characteristics of an undoped pentacene TFT (left  $L=20 \mu\text{m}$ , right  $L=200 \mu\text{m}$ ) at temperatures from 295 K to 136 K.

# THERMALLY ACTIVATED TRANSPORT IN PENTACENE

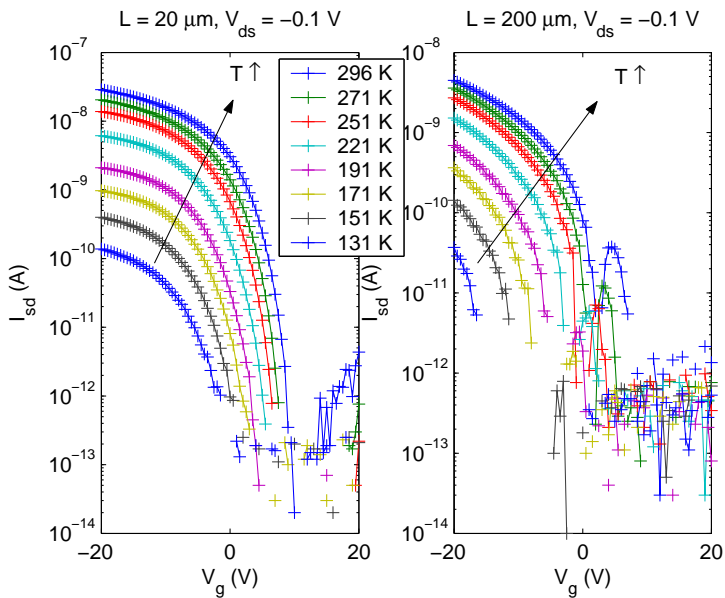


**Figure 8.2:** Transfer characteristics of a  $F_4$ TCNQ doped pentacene TFT (left  $L=20\ \mu\text{m}$ , right  $L=200\ \mu\text{m}$ ) at temperatures from 296 K to 131 K.

## 8.1. TEMPERATURE DEPENDENCE OF THE MOBILITY

---

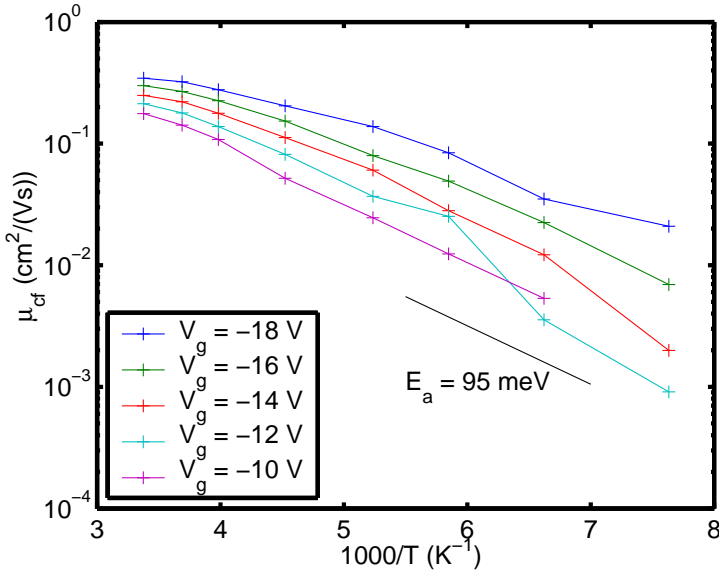


**Figure 8.3:** Contact free mobility  $\mu_{cf}$  of doped TFT at various gate voltages. The mobility decreases with decreasing  $V_g$  and approximately follows a  $\log(\mu_{cf})$  vs.  $1/T$  relation. An activation energy of  $\sim 95$  meV is found for  $V_g = -10$  V and slightly decreases with more negative  $V_g$ .

## THERMALLY ACTIVATED TRANSPORT IN PENTACENE

---

Consequently,  $E_a$  is less sensitive to injection processes and it is found to vary between 102 and 78 meV for small, respectively large  $L$ , with even a further decrease at higher  $T$  and large  $L$ . The similarity between  $\mu_{cf}$  and  $\mu_{TFT}$  for TFTs with low  $R_c$ , both with respect to the  $T$ -dependence and to the extracted  $E_a$  indicates that the mobility of doped TFTs can also be calculated from the transfer characteristics without major contact artifacts.

For the undoped TFTs, it was not possible to apply the TLM at low temperature (see Sec. 6.1.5). Therefore, only the  $\mu_{TFT}$  extracted from the transfer characteristics is presented. Fig. 8.5 shows an Arrhenius plot of the  $\mu_{TFT}$  for undoped pentacene TFTs. As expected, the so calculated  $\mu_{TFT}$  is influenced by  $R_c$  (Sec. 6.3) and therefore  $E_a$  depends strongly on  $L$ .

At small  $L$  the effect of  $R_c$  is evidenced by the existence of two temperature ranges with different  $E_a$ . In the high temperature range,  $\mu_{TFT}$  is thermally activated with  $E_a=215$  meV, while in the low temperature range  $E_a$  decreases to 93 meV. Since a change from a lower to a higher  $E_a$  with increasing  $T$  can not be explained by two different processes acting in series (e.g. contact and channel),  $\mu_{TFT}$  reflects two ways for charges to be transported. The higher activation energy  $E_a=215$  meV is probably strongly affected by contact effects as thermionic or thermally assisted tunneling through the interface barrier. The value can be compared to the injection process in undoped nanorods (Sec. 5.3.3) which shows a value between 270 meV and 360 meV. It should be noted however, that in TFT the gate field can modify the injection barrier in a different way compared to bias field in nanojunction devices. Moreover, the charge carrier density is probably different, which would also change the shape of the band bending at the interface. The part of the Arrhenius plot associated with the lower  $E_a$  is dominated by two contributions: a tunneling process through the barrier and the thermal activated transport in the

## 8.1. TEMPERATURE DEPENDENCE OF THE MOBILITY

---

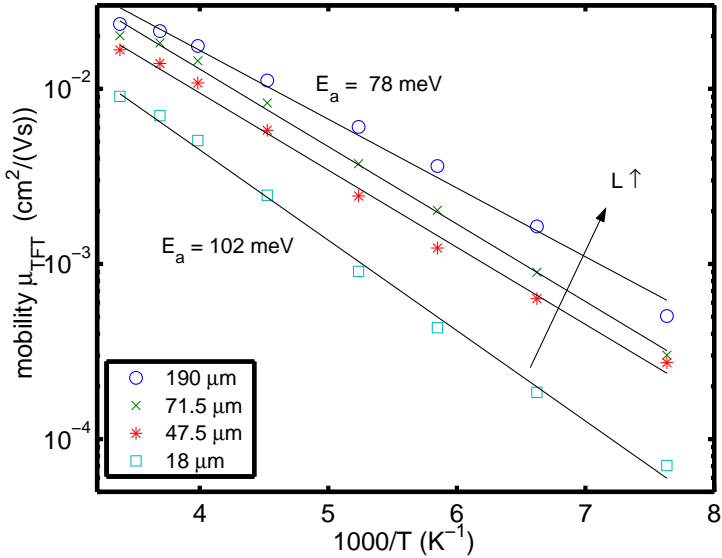


**Figure 8.4:** Thermal activation energy of the mobility  $\mu_{TFT}$  for  $F_4TCNQ$  doped pentacene TFTs. An activation energy of 78-102 meV is found for all 4 devices independently from the channel length  $L$ .

## THERMALLY ACTIVATED TRANSPORT IN PENTACENE

---

channel (i.e. not influenced by the contact). The tunneling process can be weakly temperature dependent because of a possible thermally assisted contribution [94].

With increasing  $L$ , there is a progressive change to a single temperature regime. At large  $L$ , the contact has much less influence and  $\mu_{TFT}$  is well described by a single activation energy of 71 meV.

From these data, it is concluded that the doping process has small influence on  $E_a$ . In fact, for large  $L$ , the doped and the undoped devices have similar  $E_a$ . This is explained by the fact that  $E_a$  is measured from  $\mu_{TFT}$ , which is extracted from a linear fit of the transfer characteristics either by starting at the maximum  $V_g$  or, in case of high  $R_c$  as the maximal slope. Therefore,  $\mu_{TFT}$  reflects the mobility at high  $V_g$ . In Sec. 8.5, the activation energy of *the conductivity* as a function of  $V_g$  is presented. It is found that at high  $V_g$ , there are no differences in  $E_a$  between doped and undoped TFT. (Fig. 8.9). These latter activation energies also includes the activation of the carrier concentration  $p$ . In the next section it will be shown through the analysis of the  $V_{g,th}$  shift, that the temperature may induce a change in the carrier concentration  $p$  only by a factor 2 in the investigated temperature and gate voltage range. Compared to the two orders of magnitude change of  $\mu_{TFT}$ , the change in  $p$  is unimportant. It is therefore allowed to compare the  $E_a$  of the conductivity and of  $\mu$  with the conclusion that at high  $V_g$ , both undoped and doped TFTs shows very similar thermal activated behavior. In fact, high  $V_g$  shifts the Fermi level well above the energy scale of the dopants, i.e. in the region where both undoped and doped pentacene have similar density of states (see Fig. 8.9 and Fig. 8.10). However, it is expected that the contact free mobility measured at lower  $V_g$  is different between undoped and doped TFTS.

## 8.1. TEMPERATURE DEPENDENCE OF THE MOBILITY

---

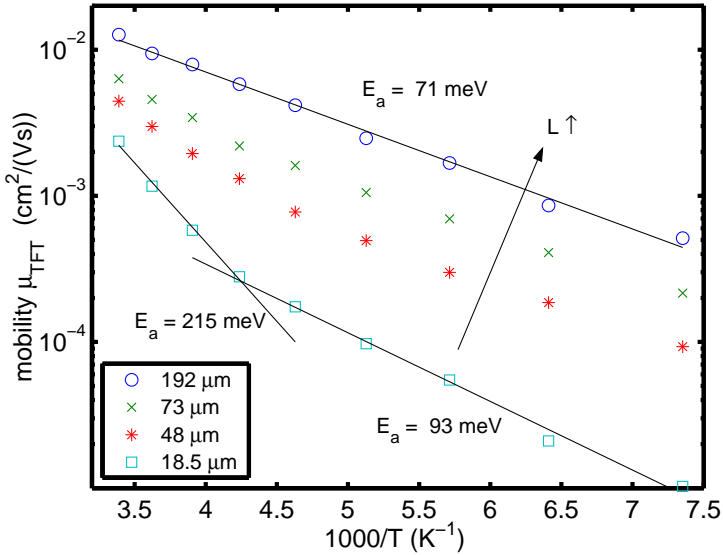


**Figure 8.5:** Thermal activation energy of the mobility  $\mu_{TFT}$  for undoped pentacene measured between 296 K and 131 K for various channel length  $L$ . For the TFT with  $L=18.5 \mu\text{m}$ , the activation energy change from 93 meV to 215 meV at 230 K. For the TFT with  $L=192 \mu\text{m}$ , a single activation energy of 71 meV is found.

## 8.2 Temperature-induced shift of the gate voltage threshold

From the transfer characteristics, a temperature and  $L$  dependent gate threshold  $V_{g,th}$  is measured. The results presented in Fig. 8.6 show that the shift  $\Delta V_{g,th}$  drawn to scale  $V_{g,th}$  at  $T=298$  K is similar for undoped and doped TFTs and in a rough approximation is independent on  $L$ . It is found that  $\Delta V_{g,th}$  is at the maximum 10 V, which represents a factor 1/2 of the maximal applied  $V_g$ . It was pointed out by Meijer *et al.* [83], that  $V_g$  is merely a fitting parameter. The temperature dependence of  $V_g$  is governed by other underlying physical parameters. However, since  $V_{g,th}$  is related to the carrier concentration  $p$ , investigation on the  $T$ -dependance of  $V_{g,th}$  is important to have information on the temperature induced variation of  $p$ . These considerations lead to the conclusion that the charge carrier density does not strongly depend on  $T$ , so that any change of the conductivity or the mobility by orders of magnitude (see previous section) can not be determined by  $p$ .

## 8.2. TEMPERATURE-INDUCED SHIFT OF THE GATE VOLTAGE THRESHOLD

---

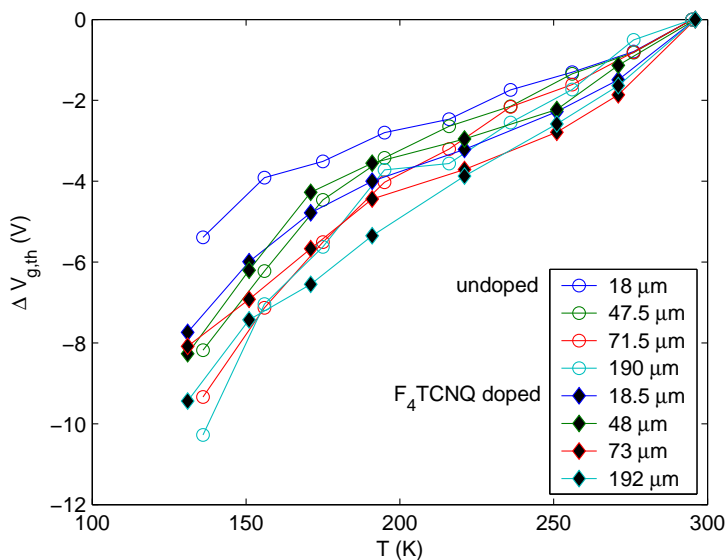


**Figure 8.6:** Temperature induced gate threshold voltage shift for undoped and doped TFTs with various channel length  $L$  drawn to scale  $V_{g,th}$  at 298 K.

### 8.3 Contact resistance

The temperature dependence of the contact resistance  $R_c$ , extracted by the TLM from doped TFTs at  $V_g = -20$  V is plotted in Fig. 8.7.

Between room temperature and 190 K,  $R_c$  increases according to the relation  $R_c = R_{c,RT} \times \exp(E_{a,c}/(kT))$ . The activation energy  $E_{a,c}$  for this process is 0.16 eV. Below 190 K, the behavior deviates and the changes are less pronounced. The high temperature regime is assigned to a thermally assisted tunneling of charge between the metal electrode and the doped organic [75, 95]. The thermal component of the tunneling process is here given by the probability  $\sim \exp(\Delta E/kT)$  that a charge hops between two sites having an energy difference  $\Delta E$ . By increasing  $T$ , there are more charges that can hop between more sites and therefore the process is thermally assisted. The possibility of a thermionic emission process originating from the thermal activated injection is excluded by the information obtained from the doped pentacene nanojunction (Sec. 5.3.2). There, a linear  $I_V$  is found from room temperature down to  $T=120$  K which shows that no substantial energy barrier is formed at the interface. At  $T$  below 190 K, there is a transition to a temperature independent  $R_c$ . In this T-range, a tunneling process could be the reason of the constant  $R_c$ . The same transition was observed in the contact resistance of carbon nanotubes []. It is therefore plausible that at this gate voltage ( $V_g=-20$  V) the barrier width at the interface between metal and doped pentacene is thin enough allowing a direct tunneling of charges.  $V_g$  seems also responsible for the missing tunneling regime in the doped nanojunction, where no deviation from an Arrhenius-like behavior is observed.

### 8.3. CONTACT RESISTANCE

---

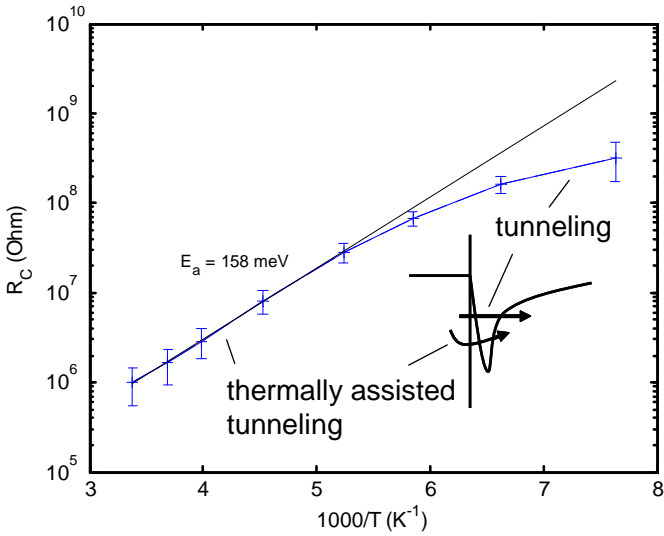


**Figure 8.7:** Temperature dependence of the contact resistance  $R_C$  at  $V_g = -20$  V for a doped TFT.  $R_C$  is calculated from transistors with channel length from  $20 \mu\text{m}$  to  $200 \mu\text{m}$  as presented in Chap. 7.

## 8.4 Charge carrier density dependence of the contact free mobility at various temperatures

In Sec. 6.1.2 the working principle of a TFT was presented. The basic model assumes a mobility  $\mu$  that does not depend on the carrier concentration. It is shown here, that this is not true in doped few ML TFT. Again, using the TLM, it is possible to extract the contact free mobility  $\mu_{cf}$  for  $V_g$  between -20 V and 0 V and at various temperatures. The gate induced charge carrier density  $p$  is calculated by  $p = V_g C_{ox} / (et)$ , where  $C_{ox}$  is the gate capacitance,  $t$  the channel thickness and  $e$  the electronic charge. The result is presented in Fig. 8.8.

It is found that the mobility  $\mu_{cf}$  increases with increasing  $p$ . This observation is consistent with a filling of the trap states by increasing  $p$ . At high  $V_g$  and corresponding increased  $p$ , part of the charges need a smaller activation energy in order to move, i.e. the mobility increases. At room temperature, the increase is about 1 order of magnitude over the applied  $V_g$  range. By lowering the temperature, the  $\mu_{cf}$  dependence on  $p$  is increased, reflecting the fact that the thermal energy can contribute less to the hopping of the charges. The model proposed by Vissenberg and Matters [96, 97], based on a variable range hopping mechanism, shows

$$\mu \sim p^{\frac{T_0}{T}-1} \tag{8.1}$$

i.e. a linear dependence of  $\mu$  from  $p$  in a double log scale. Here  $T_0$  describes the effective temperatures of the traps or alternatively the width of the exponential distribution describing the density of states (DOS). Although the stronger dependence of  $\mu$  on  $p$  at lower temperature is correctly described by the model, the  $\mu$  dependence at fixed

## 8.4. CHARGE CARRIER DENSITY DEPENDENCE OF THE CONTACT FREE MOBILITY AT VARIOUS TEMPERATURES

---

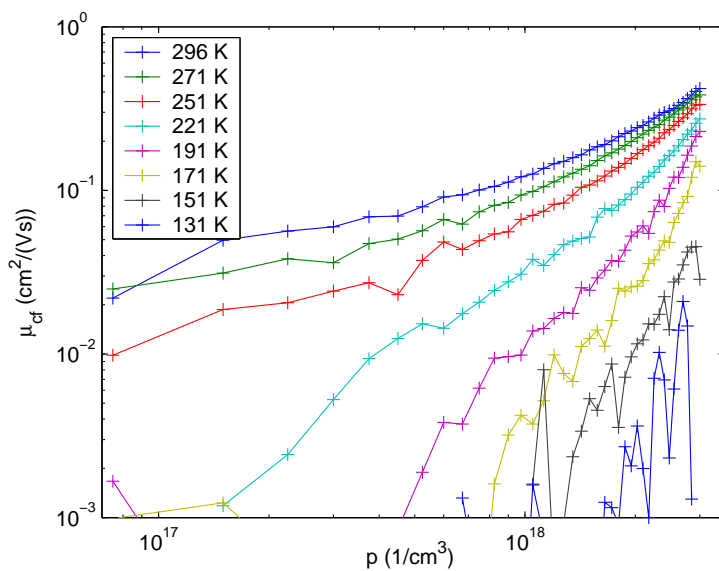


**Figure 8.8:** The contact free mobility of  $\text{F}_4\text{TCNQ}$  doped pentacene in function of the charge carrier density at temperatures between 296 K and 131 K.

## THERMALLY ACTIVATED TRANSPORT IN PENTACENE

---

$T$  is experimentally found to be larger compared to the prediction. The deviation from the model is tentatively assigned to the shape of the DOS. In the model, an exponential DOS is assumed. In the next section, it will be shown that the DOS of the doped samples showed here exhibit an additional broad peak as a consequence of the doping process.

## 8.5 Density of states in undoped and F<sub>4</sub>TCNQ doped pentacene

A fundamental aspect governing the charge transport in semiconductors is the density of states (DOS). In 3-dimensional inorganic semiconductor materials, the DOS responsible for holes conduction is well described by a parabolic relation  $N(E) \sim (E - E_v)^{3/2}$ , where  $E_v$  is the upper energy of the valence band. Above  $E_v$  (and below the conduction band  $E_c$ ) no states exists, i.e. there is a band gap. In organic crystalline small weight semiconductors, the disorder associated with the imperfect crystal structure given by the weak forces between molecules leads to a DOS that is usually modeled by a Gaussian or an exponential distribution. The consequence is an extension of the DOS into the gap region, commonly denominated as band tail. The introduction of guest molecules, either unintentionally by contaminations or intentionally by doping, further modifies the DOS shape. Theoretical models describing the transport properties are based on the knowledge of a statistical function describing the energy distribution of charges. In order to apply the model to a physical situation and to compare with transport measurements, the determination of the DOS with respect of both shape and total density is required [98].

In this Section, the transport in TFT at variable temperature is exploited to extract the DOS [99, 5]. This is done by measuring  $I_{sd}$  at a small  $V_{sd}=-0.1$  V, fixed  $V_g$  and at various temperatures. The thermal activation energy  $E_a$  is then calculated according to  $I_{sd} \sim \exp(-E_a/kT)$ . Assuming that the density of free carriers is much smaller than the density of trapped carriers  $N$  [100], the measured  $I_{sd}$  is given by the number of charges that are available in the energy range for thermal activation. In a rough approximation,  $E_a$  corresponds therefore to the energy difference between the Fermi level

## THERMALLY ACTIVATED TRANSPORT IN PENTACENE

---

$E_F$  and region close to the edge of the HOMO level. For practical purpose, the measurements are performed by scanning  $V_g$  at different temperatures and by extracting  $E_a$  from the measured  $I_{sd}(V_g, T)$ . Fig. 8.9 shows a plot of the dependence of the extrapolated  $E_a$  on  $V_g$ .

The DOS is defined as the number of states  $\partial N$  per energy interval  $\partial E$ .  $\partial N$  is given by  $\partial V_g C_{ox}/e$ , where  $C_{ox}$  is the gate capacitance per unit area ( $2.4 \times 10^{-8}$  F/cm<sup>2</sup>) and  $e$  the electronic charge. Therefore, the number of states  $N(E)$  is

$$N(E) = \frac{\partial N}{\partial E} = \frac{C_{ox}}{e} \left( \frac{\partial E_a}{\partial V_g} \right)^{-1} \quad (8.2)$$

Calculating  $N(E)$  implies to differentiate the  $E_a$  values in Fig. 8.9 with respect to  $V_g$ . The rather intriguing decrease of  $E_a$  at a certain  $V_g$  is not understood. However, in order to avoid negative slopes in the derivative, the calculation is performed by a piecewise linear fit of 7-13 points and all the results are plotted. This is a compromise between taking a small number of points and correspondingly scattering derivative, and taking too many points where the changes in  $E_a$  are smeared out. The results are presented in Fig. 8.10, where  $N(E)$  is scaled by the channel thickness to give a volume density.

The DOS of the undoped pentacene can be divided in two regions. Below 0.15 eV the data are well fitted by a Gaussian distribution by setting the total of states density equal to the density of pentacene molecules ( $3.2 \times 10^{21}$  c/cm<sup>3</sup>). The second region is fitted by an exponential part describing the tail above 0.15 eV. The exponential part

$$N(E) = \frac{N_t}{kT_0} \exp\left(\frac{-E}{kT_0}\right) \quad (8.3)$$

relates  $N(E)$  to the trap density  $N_t$  and to an effective temperature  $T_0$ . From the fit it is found  $N_0 = 3.6 \times 10^{19}$  and  $T_0 = 1330$  K.

## 8.5. DENSITY OF STATES IN UNDOPED AND F<sub>4</sub>TCNQ DOPED PENTACENE

---

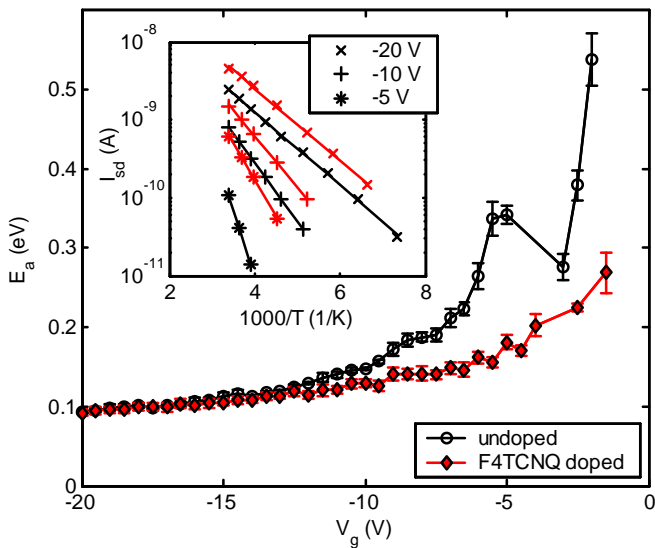


**Figure 8.9:** Thermal activation energy  $E_a$  measured at various  $V_g$  for undoped and F<sub>4</sub>TCNQ doped TFT pentacene.

# THERMALLY ACTIVATED TRANSPORT IN PENTACENE

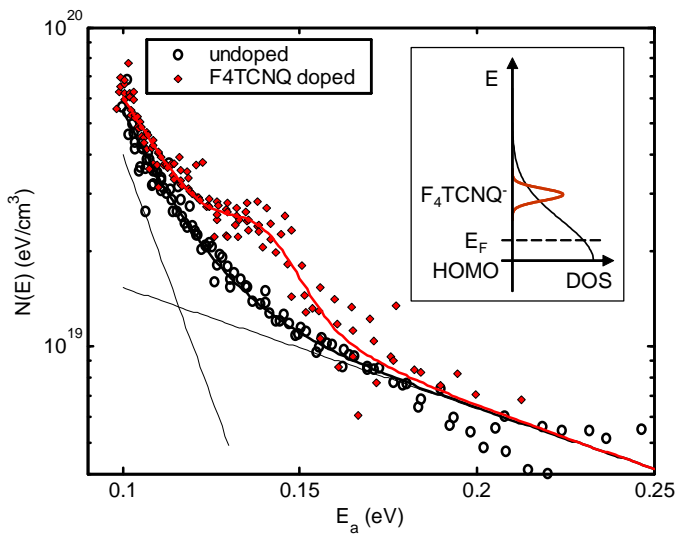


**Figure 8.10:** Density of states  $N(E)$  of undoped and  $F_4\text{TCNQ}$  doped 6-7 ML pentacene. The results are calculated from the TFTs data presented in Fig. 8.9 by applying Eq. 8.2.

## 8.5. DENSITY OF STATES IN UNDOPED AND F<sub>4</sub>TCNQ DOPED PENTACENE

---

The  $T_0$  value is in very good agreement (within 5%) with the value reported by Lang *et al.* [99], which confirm the robustness of the applied method.

The results on the trap density  $N_t$  are a factor 3 different from those reported by Lang *et al.* The difference is ascribed to the exposure of the samples to the air. This is especially important in the devices presented here, where the 6-7 ML thin channel is very sensitive to the air, even if the exposure time was minimized to 5 min. The Gaussian distribution describing  $E$  below 0.15 eV is centered at -0.5 eV with a half width half maximum  $\sigma$  of 0.11 eV. These parameters have to be taken carefully, since the fit is performed only over a small region of the distribution. However, the result is an useful starting point for the fitting of the doped TFT.

Clearly, the DOS of the doped pentacene is different from the undoped case, showing higher DOS with an additional broad peak. It is worth to note, that the peak does not arise from the fluctuation of  $E_a$  in the  $-5 \text{ V} < V_g < 0 \text{ V}$  region of Fig. 8.9. Rather, the increased  $N(E)$  is a consequence of the almost constant  $E_a$  values between -5 and -10 V (Eq. 8.2). The peak in the DOS of doped pentacene is reasonably well fitted by an additional Gaussian centered at 0.14 eV with  $\sigma$  of 0.012 eV. This peak is assigned to the F<sub>4</sub>TCNQ dopants producing additional trap levels located above the HOMO of pentacene upon inclusion in the matrix. In Sec. 6.4 the molecular orbitals of pentacene and F<sub>4</sub>TCNQ were presented. The difference between the HOMO of pentacene and the LUMO of the dopant is about 0.2 eV [36]. This is consistent with the observed position of the peak. For a detailed picture of the doping process, information on dipole formation around the ionized dopant, morphological modification of the pentacene crystal and contribution from the grain boundaries are necessary. However, some impact on the effect of the modified DOS can be drawn.

## THERMALLY ACTIVATED TRANSPORT IN PENTACENE

---

By carefully looking at the data presented in Fig. 6.12, the transfer characteristics of a 1.7 ML TFT shows some shoulder in the sub-threshold region. Similar observations were made by Mejer *et al.* [101]. There, the effect was attributed to the conduction through the thick channel far away from the interface. In the case of the devices considered here, the channel thickness is  $\sim 2$  ML, therefore this mechanism is rather improbable. The observed shoulders are tentatively assigned to the transport through the dopant induced DOS. In fact,  $N(E)$  and therefore  $I_{sd}$  does not vary monotonically as the Fermi level is shifted by  $V_g$  from the unbiased position toward the middle gap. Rather, more energy levels become available as the Fermi level approach the center of the dopant induced DOS. The states involved in the transport addressed by the Boltzmann distribution can therefore vary in a non-monotonic way, producing a non-monotonic change in  $I_{sd}$ , which is recorded as shoulders in the subthreshold part of the transfer characteristics. An implication of these scenario, is that the Fermi position at  $V_g=0$  lies between the HOMO edge and the dopant induced DOS. This hypothesis is consistent with the 'normally on' state of the doped TFT and the decreased on/off ratio, since the Fermi level can only be moved by  $V_g$  in a finite energy window.

An interesting final comparison that has to be made is between the position of the dopant induced peak in the DOS, the thermal activation energy of the  $I - V$  in doped nanojunctions (Fig. 5.3) and of  $R_c$  in doped TFTs ((Fig. 8.7). The observation is that, although measured in very different experiments, all these energies are very close. The thermal activation energy of the conduction in doped pentacene 10-nm channel measured with the nanojunctions is found to be  $0.123 \pm 0.002$  eV. The contact resistance  $R_c$  measured in a 6-7 ML TFT geometry shows a thermally activated behavior with an activation energy of 0.16 eV. This suggests that these three phenomena may be related. It is recognized, that the injection of charges from a

## 8.5. DENSITY OF STATES IN UNDOPED AND F<sub>4</sub>TCNQ DOPED PENTACENE

---

metal electrode to an organic semiconductor depends on the available states at in the second layer of molecules close to the interface [Ref]. Since the doping induce additional states, the injection is enhanced. This is what is also experimentally observed by the reduction of  $R_c$  by doping. In the nanojunction devices, the transport can hardly be separated between interface injection and channel transport since the band bending occurs in a significant part of the channel. The measured activated transport could be therefore based on the same phenomena acting on  $R_c$ . This confirm that measuring the transport in a 10-nm channel is equivalent to measuring the injection properties of the interface. In these scenario, the transport is no longer a 3-dimensional effect but rather an interface phenomena.



# Chapter 9

## Conclusions and Outlook

The electrical transport in organic semiconductor exhibits similar phenomena that are known from the bulk devices, spanning a large range of length scales, down to the molecular dimension. In contrast to inorganic semiconductors, this fact offers a possibility to add new chemical functionalities to devices in the nanometer scale.

In this thesis, few monolayer-thick thin film transistors (TFTs) have been manufactured and characterised 'in-situ'. These devices uniquely offer direct access to the quasi two dimensional active material layer. Thus, the manipulation of charge carrier density and the transistor performance by dopant ad-molecules in controlled sub-monolayer concentrations have been studied. These experiments represent a new method for the investigation of doping phenomena in organic semiconductors. The characteristic effect of  $C_{60}$ , MnTPP and  $F_4$ TCNQ deposition at sub-monolayer coverage on top of a 2 ML-

## CONCLUSIONS AND OUTLOOK

---

thick pentacene channel provides clear evidence for electronic interactions with the active material layer which are specific to the chemical structure of the dopant molecules. MnTPP, that has a large dipole moment, shows a combination of decreased mobility and charge carrier density, which can be assigned to a n-type doping process. The addition of C<sub>60</sub>, that is non-polar, shows no modifications of the transport properties of the pentacene channel. The most striking effect is found when F<sub>4</sub>TCNQ is used as a dopant molecule: Here, the investigations show a p-type charge transfer doping process that permits both an increase of the charge carrier density and an improvement of the injection efficiency at the metal-pentacene channel interface without degradation of the channel mobility. The doping efficiency is estimated to be in the range of 0.1 charges/dopant molecule. By using the transmission line method (TLM), the channel mobility  $\mu$  of TFTs with 2-7 ML-thickness is measured without the influence of the contact resistance.  $\mu$  is found to be  $0.35 \pm 0.05$  cm/(Vs) for both undoped and F<sub>4</sub>TCNQ doped TFTs, which is comparable to the state-of-the art mobility of polycrystalline organic semiconductors. This behaviour shows that the coulomb potential of the ionized dopants is screened to a large degree. An approximately linear relation is observed, for both undoped and doped pentacene, between  $\log(\mu)$  and the inverse temperature  $1/T$  that evidences the importance of hopping between localized states.

The exact physical origin of these striking phenomena related to the doping induced enhancement of the injection at the metal-organic interface has not been clarified yet. However important insight is obtained by temperature dependent transport in TFT geometry as well as in 10 nm-channel devices: The Schottky-like potential barrier between a metal electrode and an undoped organic semiconductor is revealed by the current-voltage characteristics measured in a 10 nm channel device based on the metallic nanojunction spe-

---

cially developed for this study. The contact resistance at the metal-organic interface can be lowered by the gate field in thin film transistor geometry with few monolayer channel. The effect, although on a nanometer scale, is similar to what is found in conventional inorganic semiconductors and in 1-dimensional conductor like carbon nanotubes. It is related to a potential barrier with finite thickness that results from a finite difference  $\Delta E$  between the metallic work function and the ionization potential of the pentacene. The Scottky barrier height of  $\sim 0.4$  eV has been determined from the temperature dependent current-voltage characteristics of undoped pentacene on a 10 nm-channel nanojunction. This value is consistent with the expected  $\Delta E$  of 0.47 eV.

However, the injection process can be controlled by doping engineering. The doping process here results in the local modification of the potential landscape by the individual ionized dopant molecules. The radius of influence of a single dopant is estimated to be few nanometers, therefore a few % doping ensures a complete change of the injection barrier at the metal-organic interface. In pentacene doped with 3% F<sub>4</sub>TCNQ, a highly linear, ohmic transport regime in a 10 nm channel device is achieved with an enhancement of the conductivity by a factor of  $10^3$ - $10^5$ . In the TFT geometry, the contact resistance is reduced by a factor of 20 upon 0.7% F<sub>4</sub>TCNQ doping. The effect of the gate field on the contact resistance is in this case reverted, which confirms that the charge injection process at the interface is strongly modified by the ionized dopants.

At low temperature, the contact resistance in doped TFTs shows a thermally activated behavior with an activation energy of 0.16 eV. This value is similar to the activation energy of 0.13 eV measured from the temperature dependent conductance of a 10 nm-channel doped pentacene. At sufficiently low temperature, the TFT contact resistance shows a transition to a temperature independent regime, which

is associated to the tunneling of charges between the electrode and localized states close to the electrodes.

In addition, from the temperature dependent transport characteristics of TFTs, the dopant induced modification of the density of states (DOS) is observed as an additional broad peak centered 0.14 eV above the highest occupied molecular orbitals (HOMO). It is found that the energy position of the F<sub>4</sub>TCNQ induced DOS, the activation energy of the contact resistance of doped TFT and the activation energy of the conductance of 10 nm-channel device based on F<sub>4</sub>TCN doped pentacene are similar in value. This may suggest that these three phenomena are related. On the nanometer scale, the contact resistance is described as an injection of charges from a metallic electrode through multiple site hopping processes, which depends on the availability of electronic states. Additional doping induced states can therefore enhance the injection process. This is consistent with the observed strong decrease of the contact resistance in doped pentacene TFTs and with the observed enhancement of the conductance in a 10-nm channel with doped pentacene.

The key advantage of organic electronics originates from the confinement of the charge carriers wave function at the molecular scale. This has been directly exploited for the operation of ultrathin active layer devices and by doping engineering. These methods have a potential impact on future applications based on organic semiconductors and their application within sensors and devices. Future possible experiments involve the in-situ monitoring of the charge transfer induced by the dopant by Scanning Tunneling Spectroscopy. Advanced scanning probe experimentation potentially provides molecularly resolved local experiments with individual dopants. Such experiments provide the basis for direct comparison with numerical simulations of these well defined device layers and provide the knowledge base for ultimately miniaturised organic semiconductor devices.

# Bibliography

- [1] International Technology Roadmap for Semiconductors, emerging research devices, 2005 edition.
- [2] T. Holstein, *Studies of Polaron Motion Part II. The “Small” Polaron*, *Annals of Physics* **281**, 725 – 773 (2000).
- [3] A. Troisi and G. Orlandi, *Charge-Transport Regime of Crystalline Organic Semiconductors: Diffusion Limited by Thermal Off-Diagonal Electronic Disorder*, *Phys. Rev. Lett.* **96**, 086601 (2006).
- [4] R. Coehoorn, W. F. Pasveer, P. A. Bobbert, and M. A. J. Michels, *Charge-carrier concentration dependence of the hopping mobility in organic materials with Gaussian disorder*, *Phys. Rev. B* **72**, 155206 (2005).
- [5] O. Tal, Y. Rosenwaks, Y. Preezant, N. Tessler, C. K. Chan, and A. Kahn, *Direct Determination of the Hole Density of States*

*in Undoped and Doped Amorphous Organic Films with High Lateral Resolution*, Phys. Rev. Lett. **95**, 256405 (2005).

- [6] F. Dinelli, M. Murgia, P. Levy, M. Cavallini, and F. Biscarini, *Spatially Correlated Charge Transport in Organic Thin Film Transistors*, Phys. Rev. Lett. **92**, 116802 (2004).
- [7] T. Muck, J. Fritz, and V. Wagner, *Better bottom contact properties in organic field-effect transistors with ultrathin layers*, Appl. Phys. Lett. **86**, 232101 (2005).
- [8] J. M. Lehn, *Toward complex matter: Supramolecular chemistry and self-organization*, Proc. Natl. Acad. Sci. USA **99**, 4763 – 4768 (2002).
- [9] A. P. Alivisatos, P. F. Barbara, A. W. Castleman, J. Chang, D. A. Dixon, M. L. Klein, G. L. McLendon, J. S. Miller, M. A. Ratner, P. J. Rossky, S. I. Stupp, and M. E. Thompson, *From Molecules to Materials: Current Trends and Future Directions*, Adv. Mater. **10**, 1297 – 1336 (1998).
- [10] A. P. H. J. Schenning, P. Jonkheijm, F. J. M. Hoeben, J. van Herrikhuyzen, S. C. J. Meskers, E. W. Meijer, L. M. Herz, C. Daniel, C. Silva, R. T. Phillips, R. H. Friend, D. Beljonne, A. Miura, S. De Feyter, M. Zdanowska, H. Uji, F. C. De Schryver, Z. Chen, F. Wurthner, M. Mas-Torrent, B. D. den, M. Durkut, and P. Hadley, *Towards supramolecular electronics*, Synth. Met. **147**, 43 – 48 (2004).
- [11] L. Wang, D. Fine, D. Sharma, L. Torsi, and A. Dodabalapur, *Nanoscale organic and polymeric field-effect transistors as chemical sensors*, Anal Bioanal Chem pp. 310 – 321 (2006).
- [12] S. M. Sze, *Physics of Semiconductor Devices*, 2nd. ed, John Wiley & Sons, New York (1981).

- [13] B. N. Limketkai and M. A. Baldo, *Charge injection into cathode-doped amorphous organic semiconductors*, Phys. Rev. B **71**, 085207 (2005).
- [14] A. Aviram and M. Ratner, *Molecular rectifiers*, Chem. Phys. Lett. **29**, 277 – 283 (1974).
- [15] S. Datta, *Electrical resistance: an atomistic view*, Nanotechnology **15**, S433–S451 (2004).
- [16] C. Joachim, J. K. Gimzewski, R. R. Schlittler, and C. Chavy, *Electronic Transparency of a Single C<sub>60</sub> Molecule*, Phys. Rev. Lett. **74**, 2102–2105 (1995).
- [17] X. D. Cui, A. Primak, X. Zarate, J. Tomfohr, O. F. Sankey, A. L. Moore, T. A. Moore, D. Gust, G. Harris, and S. M. Lindsay, *Reproducible Measurement of Single-Molecule Conductivity*, Science **294**, 571–574 (2001).
- [18] M. A. Reed, C. Zhou, C. J. Muller, T. P. Burgin, and J. M. Tour, *Conductance of a Molecular Junction*, Science **278**, 252–254 (1997).
- [19] J. Park, A. N. Pasupathy, J. I. Goldsmith, C. Chang, Y. Yaish, J. R. Petta, M. Rinkoski, J. P. Sethna, H. D. Abruña, P. L. McEuen, and D. C. Ralph, *Coulomb blockade and the Kondo effect in single-atom transistors*, Nature **417**, 722–725 (2002).
- [20] A. F. Morpurgo, C. M. Marcus, and D. B. Robinson, *Controlled fabrication of metallic electrodes with atomic separation*, Appl. Phys. Lett. **74**, 2084–2086 (1999).
- [21] L F Sun, S N Chin, E Marx, K S Curtis, N C Greenham, and C J B Ford, *Shadow-evaporated nanometre-sized gaps and their use in electrical studies of nanocrystals*, Nanotechnology **16**, 631–634 (2005).

- [22] S. E. Kubatkin, A. V. Danilov, H. Olin, and T. Cleason, *Tunneling Through a Single Quench-condensed Cluster*, J. Low Temp. Phys. **118**, 307 – 316 (2000).
- [23] T. T. Tsong, *Mechanisms and energetic of atomic processes in surface diffusion*, Physica A **357**, 250 – 281 (2005).
- [24] P. S. Ho and T. Kwok, *Electromigration in metals*, Rep. Prog. Phys. **52**, 301 – 348 (1989).
- [25] E. G. Gontier-Moya, I. Beszeda, and F. Moya, *Comparisons of parameters involved in mass transport and desorption at the surface of noble metals and sapphire*, Surf. Sci. **566-568**, 148 – 154 (2004).
- [26] C. J. Muller, J. M. van Ruitenbeek, and L. J. de Jongh, *Conductance and supercurrent discontinuities in atomic-scale metallic constrictions of variable width*, Phys. Rev. Lett. **69**, 140–143 (1992).
- [27] E. M. Ford and H. Ahmed, *Control of Coulomb blockade characteristics with dot size and density in planar metallic multiple tunnel junctions*, Appl. Phys. Lett. **75**, 421 – 423 (1999).
- [28] P. Morf, F. Raimondi, H.-G. Nothofer, B. Schnyder, A. Yasuda, J. M. Wessels, and T. A. Jung, *Dithiocarbamates: Functional and Versatile Linkers for the Formation of Self-Assembled Monolayers*, Langmuir **22**, 658 – 663 (2006).
- [29] T. Dadosh, Y. Gordin, R. Krahné, I. Khivrich, D. Mahalu, V. Frydman, J. Sperling, A. Yacoby, and I. Bar-Joseph, *Measurement of the conductance of single conjugated molecules*, nature **436**, 677 – 679 (2005).
- [30] J. M. Wessels, H.-G. Nothofer, W. E. Ford, F. von Wrochem, F. Scholz, T. Vossmeier, A. Schroedter, H. Weller, and A. Yasuda, *Optical and Electrical Properties of Three-Dimensional*

- Interlinked Gold Nanoparticle Assemblies*, Mater. Sci. **126**, 3349 – 3356 (2004).
- [31] D. Deamer, J. P. Dworkin, S. A. Sandford, M. P. Bernstein, and L. J. Allamandola, *The First Cell Membranes*, Astrobiology **2**, 371 – 381 (2002).
- [32] S. C. Glotzer, *Some Assembly Required*, science **306**, 419 – 420 (2004).
- [33] G. M. Whitesides and M. Boncheva, *Beyond molecules: Self-assembly of mesoscopic and macroscopic components*, Proc. Natl. Acad. Sci. USA **99**, 4769 – 4774 (2002).
- [34] S. R. Forrest, *Ultrathin organic films grown by organic molecular beam deposition and related techniques*, Chem. Rev. **97**, 1793 – 1896 (1997).
- [35] G. E. Thayer, J. T. Sadowski, F. M. z. Heringdorf, T. Sakurai, and R. M. Tromp, *Role of Surface Electronic Structure in Thin Film Molecular Ordering*, Phys. Rev. Lett. **95**, 256106 (2005).
- [36] A. Kahn, N. Koch, and W. Y. Gao, *Electronic structure and electrical properties of interfaces between metals and pi-conjugated molecular films*, J. Polym. Sci., Part B: Polym. Phys. **41**, 2529 – 2548 (2003).
- [37] W. W. Pai, C. L. Hsu, K. C. Lin, L. Y. Sin, and T. B. Tang, *Characterization and control of molecular ordering on adsorbate-induced reconstructed surfaces*, Appl. Surf. Sci. **241**, 104 – 198 (2005).
- [38] C. C. Perry, S. Haq, B. G. Frederick, and N. V. Richardson, *Face specificity and the role of metal adatoms in molecular re-orientation at surfaces*, Surf. Sci. **409**, 512 – 520 (1998).
- [39] J. A. Theobald, N. S. Oxtoby, M. A. Phillips, N. R. Champness, and P. H. Beton, *Controlling molecular deposition and layer*

- structure with supramolecular surface assemblies*, Nature **424**, 1029 – 1031 (2003).
- [40] M. de Wild, S. Berner, H. Suzuki, H. Yanagi, D. Schlettwein, S. Ivan, A. Baratoff, H. J. Guentherodt, and T. A. Jung, *A novel route to molecular self-assembly: Self-intermixed monolayer phases*, Chem. Phys. **3**, 881 – 885 (2002).
- [41] T. Yokoyama, S. Yokoyama, T. Kamikado, Y. Okuno, and S. Mashiko, *Selective assembly on a surface of supramolecular aggregates with controlled size and shape*, Nature **413**, 619 – 621 (2001).
- [42] G. Witte, S. Lukas, P. S. Bagus, and C. Wöll, *Vacuum level alignment at organic/metal junctions: "Cushion" effect and the interface dipole*, Appl. Phys. Lett. **87**, 263502 (2005).
- [43] J. V. Barth, G. Costantini, and K. Kern, *Engineering atomic and molecular nanostructures at surfaces*, Nature **437**, 671 – 679 (2005).
- [44] A. P. H. J. Schenning and E. W. Meijer, *Supramolecular electronics; nanowires from self-assembled pi-conjugated systems*, Chem. Commun. **26**, 3245 – 3258 (2005).
- [45] C. D. Dimitrakopoulos and P. R. L. Malenfant, *Organic Thin Film Transistors for Large Area Electronics*, Adv. Mater. **14**, 99 – 117 (2002).
- [46] F. Amy, C. Chan, and A. Kahn, *Polarization at the gold/pentacene interface*, Org. Electron. **6**, 85 – 91 (2005).
- [47] B. D. Patterson, C. Bronnimann, D. Maden, F. Gozzo, A. Groso, B. Schmitt, M. Stampanoni, and P. R. Willmott, *The materials science beamline at the Swiss Light Source*, Nucl. Instrum. Methods Phys. Res. **238**, 1 – 4 (2005).

- [48] R. Ruiz, D. Choudhary, B. Nickel, T. Toccoli, K.-C. Chang, A.C. Mayer, P. Clancy, J.M. Blakely, R.L. Headrick, S. Iannotta, and G.G. Malliaras, *Pentacene Thin Film Growth*, Chem. Mat. **16**, 4497–4508 (2004).
- [49] S. E. Fritz, S. M. Martin, C. D. Frisbie, M. D. Ward, and M. F. Toney, *Structural Characterization of a Pentacene Monolayer on an Amorphous SiO<sub>2</sub> Substrate with Grazing Incidence X-ray Diffraction*, J. A. Chem. Soc. **126**, 4084 – 4085 (2004).
- [50] G. Horowitz and M. E. Hajlaoui, *Mobility in polycrystalline oligothiophene field-effect transistors dependent on grain size*, Adv. Mater. **12**, 1046 – 1050 (2000).
- [51] H. Yanagisawa, T. Tamaki, M. Nakamura, and K. Kudo, *Structural and electrical characterization of pentacene films on SiO<sub>2</sub> grown by molecular beam deposition*, Thin Solid Films **464**, 398 – 402 (2004).
- [52] A. S. Killampalli and J. R. Engstroma, *Nucleation of pentacene thin films on silicon dioxide modified with hexamethyldisilazane*, Appl. Phys. Lett. **88**, 143125 (2006).
- [53] T. Jentzsch, H. J. Juepner, K. W. Brzezinka, and A. Lau, *Efficiency of optical second harmonic generation from pentacene films of different morphology and structure*, Thin Solid Films **315**, 273 – 280 (1998).
- [54] B. Nickel, R. Barabash, R. Ruiz, N. Koch, A. Kahn, L. C. Feldman, R. F. Haglund, and G. Scoles, *Dislocation arrangements in pentacene thin films*, Phys. Rev. B **70**, 125401 (2004).
- [55] I. P. M. Bouchoms, W. A. Schoonveld, J. Vrijmoeth, and T. M. Klapwijk, *Morphology identification of the thin film phases of vacuum evaporated pentacene on SIO substrates*, Synth. Met. **104**, 175 – 178 (1999).

- [56] J. H. Kang and X.-Y. Zhu, *Pi-stacked pentacene thin films grown on Au(111)*, Appl. Phys. Lett. **82**, 3248–3250 (2003).
- [57] N. Koch, A. Kahn, J. Ghijsen, J. J. Pireaux, J. Schwartz, R. L. Johnson, and A. Elschner, *Conjugated organic molecules on metal versus polymer electrodes: Demonstration of a key energy level alignment mechanism*, Appl. Phys. Lett. **82**, 70 – 72 (2003).
- [58] W. S. Hu, Y. T. Tao, Y. J. Hsu, D. H. Wei, and Y. S. Wu, *Molecular orientation of evaporated pentacene films on gold: Alignment effect of self-assembled monolayer*, Langmuir **21**, 2260 – 2266 (2005).
- [59] Y. Abe, T. Hasegawa, Y. Takahashi, T. Yamada, and Y. Tokurac, *Control of threshold voltage in pentacene thin-film transistors using carrier doping at the charge-transfer interface with organic acceptors*, Appl. Phys. Lett. **87**, 153501 (2005).
- [60] A. Rose, *Space-charge-limited currents in solids*, Phys. Rev. **97**, 1538 – 1544 (1955).
- [61] S. C. Jain, W. Geens, A. Mehra, V. Kumar, T. Aernouts, J. Poortmans, and R. Mertens, *Injection- and space charge limited-currents in doped conducting organic materials*, J. Appl. Phys. **89**, 3804 – 3810 (2001).
- [62] J. Simmons, *Poole-frenkel effect and schottky effect in metal-insulator-metal systems*, Phys. Rev. **155**, 657 – 660 (1967).
- [63] B. A. Gregg, S. E. Gledhill, and B. Scott, *Can true space-charge-limited currents be observed in  $\pi$ -conjugated polymers?*, J. Appl. Phys. **99**, 116101 (2006).
- [64] S. Ogawa, T. Naijo, Y. Kimura, H. Ishii, and M. Niwano, *Photoinduced doping effect of pentacene field effect transistor in oxygen atmosphere studied by displacement current measurement*, Appl. Phys. Lett. **86**, 252104 (2005).

- [65] R. Ye, M. Baba, K. Suzuki, Y. Ohishi, and K. Mori, *Effects of O<sub>2</sub> and H<sub>2</sub>O on electrical characteristics of pentacene thin film transistors*, Thin Solid Films **464-465**, 437–440 (2004).
- [66] P. Emtage and J. Odwyer, *Richardson-schottky effect in insulators*, Phys. Rev. Lett. **16**, 356 – 358 (1966).
- [67] S. Barth, U. Wolf, H. Bassler, P. Muller, H. Riel, H. Vestweber, P. F. Seidler, and W. Riess, *Current injection from a metal to a disordered hopping system. III. Comparison between experiment and Monte Carlo simulation*, Phys. Rev. B **60**, 8791 – 8797 (1999).
- [68] J. C. Scott, *Metal-organic interface and charge injection in organic electronic*, J. Vac. Sci. Technol. A **21**, 521–531 (2003).
- [69] D. J. Gundlach, L. Zhou, J. A. Nichols, and T. N. Jackson, *An experimental study of contact effects in organic thin film transistors*, J. Appl. Phys. **100**, 024509 (2006).
- [70] F. Leonard and J. Tersoff, *Novel length scales in nanotube devices*, Phys. Rev. Lett. **83**, 5174 – 5177 (1999).
- [71] H. Ishii, K. Sugiyama, E. Ito, and K. Seki, *Energy level alignment and interfacial electronic structures at organic metal and organic organic interfaces*, Adv. Mater. **11**, 605 (1999).
- [72] H. Vazquez, W. Gao, F. Flores, and A. Kahn, *Energy level alignment at organic heterojunctions: Role of the charge neutrality level*, Phys. Rev. B **71**, 041306 (2005).
- [73] M. A. Baldo and S. R. Forrest, *Interface-limited injection in amorphous organic semiconductors*, Phys. Rev. B **6408**, 085201 (2001).
- [74] A. R. Hosseini, M. H. Wong, Y. Shen, and G. G. Malliaras, *Charge injection in doped organic semiconductors*, J. Appl. Phys. **97**, 023705 (2005).

- [75] M. Abkowitz and H. Mizes, *Emission limited injection by thermally assisted tunneling into a trap-free transport polymer*, Appl. Phys. Lett. **66**, 1288 – 1290 (1995).
- [76] J. Appenzeller, M. Radosavljevic, J. Knoch, and P. Avouris, *Tunneling Versus Thermionic Emission in One-Dimensional Semiconductors*, Phys. Rev. Lett. **92**, 048301 (2004).
- [77] J. Ristein, *Surface transfer doping of semiconductors*, Science **313**, 1057 – 1058 (2006).
- [78] C. S. Kim, S. J. Jo, S. W. Lee, W. J. Kim, and H. K. Baika, *High- $k$  and low- $k$  nanocomposite gate dielectrics for low voltage organic thin film transistors*, Appl. Phys. Lett. **88**, 243515 (2006).
- [79] J. Collet, O. Tharaud, A. Chapoton, and D. Vuillaume, *Low-voltage, 30 nm channel length, organic transistors with a self-assembled monolayer as gate insulating films*, Appl. Phys. Lett. **76**, 1941–1943 (2000).
- [80] V. Podzorov, E. Menard, A. Borissov, V. Kiryukhin, J. A. Rogers, and M. E. Gershenson, *Intrinsic Charge Transport on the Surface of Organic Semiconductors*, Phys. Rev. Lett. **93**, 086602 (2004).
- [81] L. Bürgi, H. Sirringhaus, and R. H. Friend, *Noncontact potentiometry of polymer field-effect transistors*, Appl. Phys. Lett. **80**, 2913 – 2915 (2002).
- [82] P. V. Necliudov, M. S. Shur, D. J. Gundlach, and T. N. Jackson, *Contact resistance extraction in pentacene thin film transistors*, Solid-State Electron. **47**, 259 – 262 (2003).
- [83] E. J. Meijer, C. Tanase, P. W. M. Blom, E. van Veenendaal, B. H. Huisman, D. M. de Leeuw, and T. M. Klapwijk, *Switch-on voltage in disordered organic field-effect transistors*, Appl. Phys. Lett. **80**, 3838 – 3840 (2002).

- [84] S. Scheinert, G. Paasch, M. Schrödner, H.-K. Roth, S. Sensfuß, and T. Doll, *Subthreshold characteristics of field effect transistors based on poly3-dodecylthiophene and an organic insulator*, J. Appl. Phys. **92**, 330 – 337 (2002).
- [85] J. B. Koo, J. H. Lee, C. H. Ku, S. C. Lim, S. H. Kim, J. W. Lim, S. J. Yun, and T. Zyung, *The effect of channel length on turn-on voltage in pentacene-based thin film transistor*, Synth. Met. **156**, 633 – 636 (2006).
- [86] G. C. Liang and A. W. Ghosh, *Identifying contact effects in electronic conduction through C60 on silicon*, Phys. Rev. Lett. **95**, 076403 (2005).
- [87] G. Horowitz, *Tunnel current in organic field-effect transistors*, Synth. Met. **138**, 101 – 105 (2003).
- [88] J. Zaumseil, K. W. Baldwin, and J. A. Rogers, *Contact resistance in organic transistors that use source and drain electrodes formed by soft contact lamination*, J. Appl. Phys. **93**, 6117–6124 (2003).
- [89] S. Heinze, J. Tersoff, R. Martel, V. Derycke, J. Appenzeller, and P. Avouris, *Carbon nanotubes as Schottky barrier transistors*, Phys. Rev. Lett. **89**, 106801 (2002).
- [90] B. H. Hamadani, H. Ding, Y. Gao, and D. Natelson, *Doping-dependent charge injection and band alignment in organic field-effect transistors*, Phys. Rev. B **72**, 235302 (2005).
- [91] L. Brgi, T. J. Richards, R. H. Friend, and H. Sirringhaus, *CLose look at charge injection in polymer field-effect transistors*, J. Appl. Phys. **94**, 6129 – 6137 (2003).
- [92] J. Appenzeller, J. Knoch, V. Derycke, R. Martel, S. Wind, and P. Avouris, *Field-Modulated Carrier Transport in Carbon Nanotube Transistors*, Phys. Rev. Lett. **89**, 126801 (2002).

- [93] N. Koch, S. Duhm, and J.P. Rabe, *Optimized Hole Injection with Strong Electron Acceptors at Organic-Metal Interfaces*, Phys. Rev. Lett. **95**, 237601–4 (2005).
- [94] M. A. Abkowitz, H. A. Mizes, and J. S. Facci, *Emission limited injection by thermally assisted tunneling into a trap-free polymer transistor*, Appl. Phys. Lett. **66**, 1288 – 1290 (1996).
- [95] T. van Woudenberg, P. W. M. Blom, M. C. J. M. Vissenberg, and J. N. Huiberts, *Temperature dependence of the charge injection in poly-dialkoxy-phenylene vinylene*, Appl. Phys. Lett. **79**, 1697 – 1699 (2001).
- [96] M. C. J. M. Vissenberg and M. Matters, *Theory of the field-effect mobility in amorphous organic transistors*, Phys. Rev. B **57**, 12964 – 12967 (1998).
- [97] W. Brütting, ed., *Physics of Organic Semiconductors*, chap. 11, Wiley-VCH (2005).
- [98] W. Brütting, ed., *Physics of Organic Semiconductors*, chap. 12, Wiley-VCH (2005).
- [99] D. V. Lang, X. Chi, T. Siegrist, A. M. Sergent, and A. P. Ramirez, *Amorphouslike density of gap states in single-crystal pentacene*, Phys. Rev. Lett. **93**, 086802 (2004).
- [100] B. A. Gregg, S. G. Chen, and R. A. Cormier, *Coulomb forces and doping in organic semiconductors*, Chem. Mater. **16**, 4586 – 4599 (2004).
- [101] E. J. Meijer, C. Detcheverry, P. J. Baesjou, E. van Veenendaal, D. M. de Leeuw, and T. M. Klapwijk, *Dopant density determination in disordered organic field-effect transistors*, J. Appl. Phys. **93**, 4831 – 4835 (2003).

# Publications

## Articles

- Vanoni C., Tsujino S. and Jung T.A., *Reduction of the contact resistance by doping in pentacene few monolayers thin film transistors and self-assembled nanocrystals*, Appl. Phys. Lett., **90**, 193119 (2007).
- Vanoni C., Tsujino S. and Jung T.A., *Temperature dependence of charge-injection at the metal-organic semiconductor interface in pristine and doped pentacene*, submitted.
- Vanoni C., Tsujino S. and Jung T.A., *Sub-monolayer detection by surface doping of 1-2 monolayers pentacene thin-film transistors*, in preparation.

## Oral Presentations

- Electrical Transport in Nanoscale Pentacene, NCCR Annual Meeting, Basel, April 2006.
- Electrical Transport in Nanoscale Pentacene, SPS, Lausanne, Februar 2006.
- Electrical Transport Studies of Metal-Molecules-Metal Nanojunctions, SONS Meeting, Basel, November 2004.
- Toward Electrical Transport Studies of Metal-Molecule(s)-Metal Nanojunctions, NCCR Annual Meeting, Basel, September 2004.
- Electrical Transport Studies of Metal-Molecules-Metal Nanojunctions, EMRS, Strassbourg (F), Mai 2004.
- Toward Electrical Transport Studies of Metal-Molecule-Metal Nanojunctions, SPS, Neuchtel, Februar 2004.
- Posters Doping of few monolayers thin film transistors: charge carrier density and injection properties, SPS, Zrich, Februar 2007.
- Doping of few monolayers thin film transistor and nanoscale transport, ICN+T, Basel, August 2006.
- Charge Transport in Nanoscale Organic Semiconductor, IFMIT Workshop, Kerkrade (NL), November 2005.
- Charge Transport in Nanoscale Organic Semiconductor, NCCR Annual Meeting, Gwatt, Oktober 2005.

## Poster Presentations

- Posters *Doping of few monolayers thin film transistors: charge carrier density and injection properties*, SPS, Zrich, February 2007.

- *Doping of few monolayers thin film transistor and nanoscale transport*, ICN+T, Basel, August 2006.
- *Charge Transport in Nanoscale Organic Semiconductor*, IFMIT Workshop, Kerkrade (NL), November 2005.
- *Charge Transport in Nanoscale Organic Semiconductor*, NCCR Annual Meeting, Gwatt, October 2005.



# Acknowledgments

This thesis will not have the very recent shape without the supervision of Dr. Soichiro Tsujino. I really appreciate his willing to take up the responsibility of my promotion. Through his teaching, advices, suggestions and ideas, which kept my mind busy for many evenings, I had the chance to progress in the research and to expand my knowledge and my scientific ways to think. Soichiro, I am profoundly grateful to you.

I would like to thank very much Dr. Thomas Jung from the PSI and Prof. Christian Schönenberger from the University of Basel to give me the opportunity to perform a thesis in such an interesting and ambitious field. The constant encouragement coming from stimulating discussions help me in the difficult moments ensuring the successfully accomplishment of my doctoral studies. For that, I also would like to address my respect and appreciation to Dr. Walter Riess from IBM which kindly accept to be my referee.

For the support and the help at the Laboratory for Micro and

Nanotechnology I would like to thank Prof. Jens Gobrecht and the technicians Stefan Stutz, Anja Weber and last but not least the solution oriented capabilities of Rolf Schelldorfer.

As inspiring and guiding friend I would like to thank Peter Morf for a lot of interesting discussions about physics and real life, sometimes after work and late in the evening.

I also would like to thank all the office colleagues, Li Zhang, Patrick Farquet, Sandro Bellini and Christian Dais. A special thanks goes to Günter Palfinger, which introduced me in the beautiful and very useful world of Matlab and LaTeX. Thanks also to Anna Diaz, Dirk Backes, Slawo Czekaj and Maxi Scheinert for together enjoying the lunch break. For those who cannot find her/his name in this page, I surely forgot it here but you can be confident that I didn't forget the hard but rewarding time we spent together.

Last, first and always, I must thank my sister for hosting me over the week-end and my parents, who gave me the best education over the past years, leaving me the freedom to choose my way.

**This work has been supported by the Swiss National Science Foundation (SNF) and the National Center of Competence in Research (NCCR).**

## CURRICULUM VITAE

### ***PERSONAL DETAILS***

---

|                |                 |
|----------------|-----------------|
| Name           | Claudio Vanoni  |
| Date of birth  | 13. August 1975 |
| Place of birth | Locarno (TI)    |
| Nationality    | Switzerland     |

### ***EDUCATION AND RESEARCH EXPERIENCES***

---

|               |  |
|---------------|--|
| 2006, 2007    | Post-doctoral position at the Laboratory for Micro- and Nanotechnology, PSI Villigen.  |
| 2002 – 2006   | Ph.D in Experimental Physics, University of Basel, work performed at the Paul Scherrer Institute (PSI), 5232 Villigen PSI, Switzerland.  |
| 2000 – 2001   | research associate at the Institute for Nonmetallic Inorganic Materials (Solid Oxide Fuel Cell Group), ETH Zürich.   |
| 1994 – 2000   | Diploma from the ETH Zürich, Department of Materials.  |
| Diploma work: | <i>“Production and physiochemical characterization of self-assembled monolayers on titanium surfaces and their influence on fibroblast behavior“</i> , performed partially at the Laboratory for Surface Science and Technology, ETHZ (advisors Prof. M. Textor and Prof. N. D. Spencer) and partially at the Faculty of |

Dentistry, University of British Columbia,  
Vancouver CA (Prof. D.M. Brunette).

Semester works “*Synthesis of magnetic nanoparticles and preparation of magnetic polymer/metal nanocomposite*”, Polymer Technology Group, ETHZ (Prof. P. Smith).

“*Electrical properties of copper doped ceria solid solution*”, Institute for Nonmetallic Inorganic Materials, ETHZ (Prof. L. J. Gauckler).